UNIVERSITY *of*
TASMANIA
AUSTRALIA

School of Natural Sciences

A Survey for Stellar Relics of Galaxy Formation in the Large Magellanic Cloud

Bryn D. Emptage
B.Sc. (Hons.)

November 2018

Supervisor: Associate Prof. Andrew A. Cole

Submitted in fulfilment of the requirements for the Degree of
Doctor of Philosophy

Declaration

This thesis contains no material which has been accepted for a degree or diploma by the University or any other institution, except by way of background information and duly acknowledged in this thesis, and to the best of the my knowledge and belief no material previously published or written by another person except where due acknowledgement is made in the text of the thesis.

Signed:

November 16, 2018

Acknowledgements

There are several people to whom I owe a great deal of thanks for their assistance in completing this project. The first and foremost is my supervisor Andrew Cole who kept me on the right path, and seems to be an endless well of knowledge and insight. To my family, thank you for supporting me through my project, and for your consistent motivation. To everyone in the School of Natural Sciences at UTAS, thank you for providing friendly and supportive environment. Finally, to my wife Alice, thank you for your support, your boundless enthusiasm for my project, and for your love.

Thank you to all the support staff at AAO for a fantastic observation run.

This research has made use of the SIMBAD database, operated at CDS, Strasbourg, France.

This research has made use of the NASA/ IPAC Infrared Science Archive, which is operated by the Jet Propulsion Laboratory, California Institute of Technology, under contract with the National Aeronautics and Space Administration.

Abstract

We aim to identify some of the first extremely metal-poor stars in the Large Magellanic Cloud (LMC) based on photometric selection of red giants. The photometric data were from observations using the CTIO 4m Blanco telescope and MOSAIC-II imager, covering 5.4 square degrees of the LMC, extending from the central bar to a projected distance of 8 degrees. Candidates were identified using Washington photometry, paired with a custom narrowband filter centred on the Calcium II H & K lines - in which metal-poor stars would exhibit greater flux. For the most likely metal-poor candidates, medium resolution spectra were obtained in the visible (R $\approx$ 1500), and the infrared (R $\approx$ 10000) using the 3.9m AAT telescope with the 2df + AAOmega instruments. The metallicity and radial velocities of these stars were derived from measurements of the near-infrared calcium triplet.

Based on the candidate frequency, the photometric pre-selection proved successful, yielding 104 metal-poor candidates. Of these, 34 stars are previously unknown stars more metal-poor than [Fe/H] = -2.0, with our most metal-poor candidate having a metallicity of [Fe/H] = -2.93. This is the most metal-poor known object in the LMC.

From these results, candidates for high-dispersion follow-up spectroscopy have been identified.

TABLE OF CONTENTS

LIST OF FIGURES

LIST OF TABLES

Chapter 1

Introduction

All matter in the universe started out as a combination of the light elements hydrogen, helium, and minute amounts of lithium that were produced in the Big Bang. As stars aged, they began to create heavier elements - carbon, nitrogen, oxygen, silicon, increasing in atomic number up to iron, dependent on their mass. The production of these elements produces energy for the stars, but the formation of elements heavier than iron results in a net loss of energy. The energy to form heavier elements is provided in abundance during the final stages of massive stars' lives. Stars more massive than $\sim$ 8 $M_{\odot}$ end their lives in explosive supernova events (type II supernova), which are responsible for the creation of elements up to uranium (Pagel 1997). These supernovae expel all these elements, dispersing them into the interstellar medium, where they are incorporated into the next generation of stars.

The next generation of stars has the remnants of the previous generation, and therefore is slightly more metal-rich[1] than its predecessors. Eventually, some of these stars will also go supernova, contributing the remnants of its predecessors

[1]Metal refers to any elements other than hydrogen and helium.

and the metals they created during their lives to the interstellar medium. This process is known as the chemical enrichment of galaxies.

The most recent stars to form in our Galaxy contain the elements produced by several generations of stars before them. These stars are metal-rich and are generally found in areas of recent star-formation. In the Milky Way (MW), these stars are primarily found within the disk. The older stars in a galaxy have not had the continual enrichment of the young stars and hence are typically metal-poor by comparison. These stars are typically located in the halo and the thick disk of galaxies like the MW. This leads to an observable anti-correlation between age and metallicity, the age-metallicity relation (AMR).

The distinction between the young and old stars of galaxies led to the definition of stellar populations. The younger, visibly bluer stars were called Population I, as they stood out from the redder, older stars, which were called Population II. These two populations also shared a distinction in their metallicities due to the nature of chemical evolution (e.g. Wiescher et al. (2012)). Therefore, the metallicity of the Population II stars can be used to infer the duration of major early star-forming activity in their host galaxy. The way abundances of elements change with time is shown in Figure 1.1.

Population II have only had metal contributions from a few progenitor stars, with the most metal-poor Population II stars only having contributions from one or two supernovae. The progenitors of the most metal-poor stars would have formed with effectively zero metal content, containing only the first elements created during the Big Bang (Bromm 2013). These stars represent an as yet unobserved third population of stars, called Population III. Population III stars are responsible for the reionisation of the early Universe and the energy of their stellar winds and supernovae is thought to have contributed to the feedback processes that

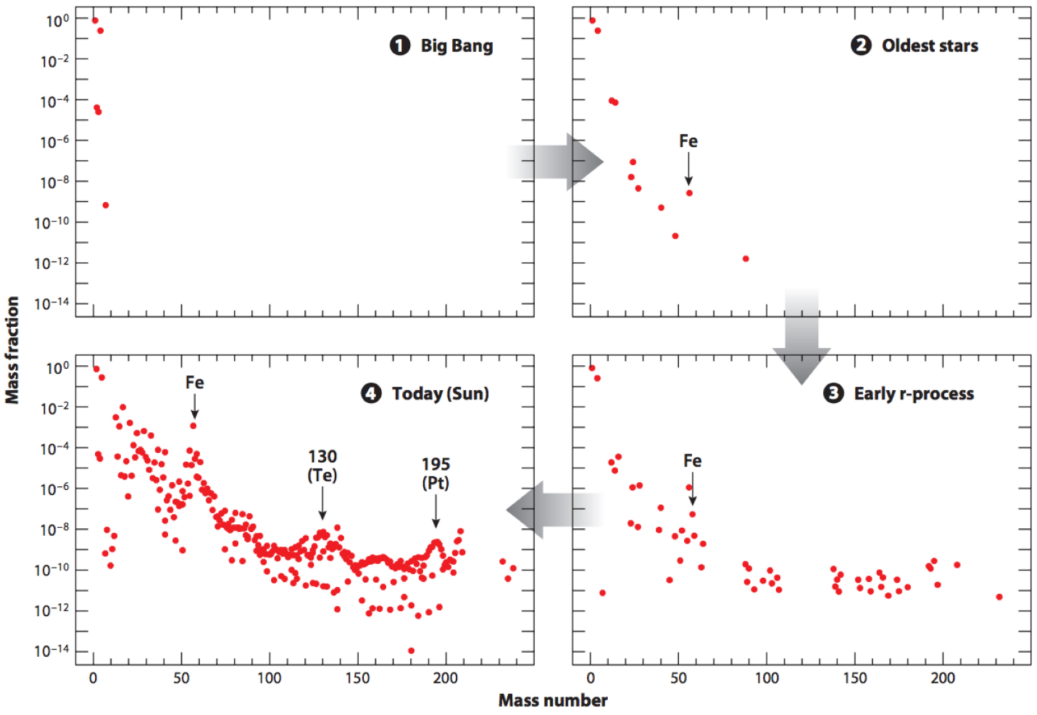

Figure 1.1: Figure from Wiescher et al. (2012), showing the abundances of the chemical elements as a function of mass number A at different stages of Galactic chemical evolution.

strongly shaped the early evolution of galaxies. If any of these Population III stars exist today, they will be invaluable in contributing to our knowledge of the early Universe.

1.1 Metal-Poor Stars

Metal-poor stars are among some of the oldest members of a given stellar population. Due to their usefulness as probes for the early epochs of galaxy formation, they have been the subject of many surveys over the last several decades, e.g. Bond (1970), Beers et al. (1985), Frebel et al. (2010), and Starkenburg et al. (2017). However, these metal-poor stars have remained relatively scarce, as they have proven difficult to identify, e.g. as in Christlieb et al. (2002).

The degree to which a star is metal-poor can be determined by measuring the total metal abundance [M/H] within that star. A proxy for the total metal abundance is [Fe/H], the abundance of iron in the star with respect to the Sun, given in equation 1.1.

$$[\mathrm{Fe/H}] = \log_{10}\left(\frac{N_{Fe}}{N_H}\right) - \log_{10}\left(\frac{N_{Fe}}{N_H}\right)_{\odot} \tag{1.1}$$

The term metal-poor refers to a large range of metallicities, typically anything below [Fe/H] $= -1.0$. To avoid ambiguity, we will adopt the nomenclature defined in Beers & Christlieb (2005) for classifying levels of metal deficiency, given in Table 1.1.

Table 1.1: The nomenclature for metal-poor stars as suggested by Beers & Christlieb (2005)

[Fe/H]	Term	Acronym
< -1.0	Metal-Poor	MP
< -2.0	Very Metal-Poor	VMP
< -3.0	Extremely Metal-Poor	EMP
< -4.0	Ultra Metal-Poor	UMP
< -5.0	Hyper Metal-Poor	HMP
< -6.0	Mega Metal-Poor	MMP

Many different methods have been used in attempts to identify these metal-poor stars in the field, primarily within the MW. The earliest metal-poor stars were linked to the halo of the MW, and as such, the surveys pre-selected stars based on their proper motions. Such studies are very limited, as they are restricted by the metallicity distribution function (MDF) of the populations in which they reside, and are kinematically biased, as there are many metal-poor stars without high proper-motions (Bond 1970; Beers & Christlieb 2005). Attempts to identify kinematically unbiased populations thus required a different methodology for selection of stars - for which we have two potential applicable wide-scale options: objective-prism based spectroscopic surveys, and colorimetric surveys (Christlieb 2006).

The survey by Bond (1970) was one of the first spectroscopic surveys to specifically search for metal-poor stars in the galaxy, covering 4000 square degrees of the MW. This survey was the first to indicate the extent of proper motions that metal-poor stars had, and show that metal-poor stars weren't limited to having high proper-motions. A follow-up survey (Bond 1980) further increased the list

of known metal-poor stars with $M_v < +2.0$ and [Fe/H] $\leqslant -1.5$ by 132 stars. The lowest metallicity stars observed in these first surveys were around [Fe/H] $= -3.0$, leading to the conclusion that stars of greater metal deficiency were exceedingly rare.

A majority of known VMP stars were discovered by the HK survey by Beers et al. (1985) and Beers et al. (1992), and the Hamburg/ESO (HES) survey (Christlieb et al. 2002). Both surveys are objective-prism-based, covering a large area of the MW, $\sim$ 2000 square degrees for the HK survey, and $\sim$5000 for HES. The selection of apparently metal-poor spectra yielded approximately 1000 stars more metal-poor that [Fe/H] $= -2.0$, and $\sim$100 stars more metal-poor than [Fe/H] $= -3.0$, increasing the number of known EMP stars by a factor of 7. These candidate stars were selected based on the widths of the Ca II K line and the Balmer lines in their spectra. Due to a limiting magnitude of $V \leqslant 15.0$, a majority of the stars discovered in this survey were relatively close, having distances between 2 kpc and 10 kpc. In addition, the HK survey was the first to identify objects in the UMP category (Beers et al. 1992).

Both spectroscopic and colorimetric methods are effective at identifying candidate metal-poor stars in wide fields, but still require confirmation of metallicity using follow-up medium-to-high-resolution spectroscopy. Spectroscopic surveys are capable of efficiently identifying metal-poor stars within the MW, and as such, these types of survey have been the most effective, yielding a majority of the known VMP stars in our galaxy to date.

Objective-prism-based spectroscopic surveys become increasingly difficult in the more crowded fields due to overlapping spectra, thus they tend to be limited to higher Galactic latitudes. For the more crowded fields, colorimetric surveys are necessary, which rely on the fact that metallicity has an effect on the observed

colours of the stars. The sensitivity to changes in metallicity is dependent on the photometric filter system used in the survey (Beers & Christlieb 2005). Additional filters can complement standard filter systems, enhancing the capacity to detect lower metallicity stars. For example, a narrowband filter centred on the region around the Ca II H & K lines, when used in conjunction with the *uvby* filters, could distinguish metallicities down to [Fe/H] = −3.4 (Anthony-Twarog & Twarog 1998).

Recently, there have been several photometry-based surveys searching for metal-poor stars, such as SkyMapper (Schmidt et al. 2005; Keller et al. 2012) and PRISTINE (Starkenburg et al. 2017). Both of these surveys rely on the use of a filter sensitive to changes in the Ca II H & K lines to detect metal-poor objects. SkyMapper observed the entire southern sky, with survey limits similar to the Sloan Digital Sky Survey. This survey has been responsible for the discovery of 122 previously unknown stars, 41 of which were confirmed to be EMP. SkyMapper is the first program to observe stars in the MMP category (eg. Nordlander et al. (2017); Keller et al. (2014)), which puts their metal content close to the elusive population III stars. PRISTINE also showed high efficacy in the selection of metal-poor targets based on their photometry, with a reported successful identification rate of 70 percent for stars more metal-poor than [Fe/H] = −2.5 (Youakim et al. 2017), identifying 33 new EMP stars.

Such low numbers of reported EMP stars in these surveys are a result of the MDF of the galaxy. In a given population, the chances of observing a metal-poor star decreases by a factor of 10 for every factor of 10 decrease in metallicity. It is estimated that EMP stars represent a proportion of fewer than 1 in 1000 stars (Norris 2004). Due to the scarcity of the lower metallicity stars, this relationship isn't well defined below [Fe/H] = −3.0. Results indicate that as few as 1 in 200 stars more metal-poor than EMP would be classified in the HMP category

(Christlieb 2006).

There is a hypothetical lower limit to the metallicities of stars that have active interiors. Mixing within a star that formed with very low metal content (e.g. Population III stars) would have a metallicity of [Fe/H] ≈ -5.7 today (Iben 1983). Currently, only one star has been discovered below this limit with a metallicity of [Fe/H] $\leqslant -6.5$ (Nordlander et al. 2017; Keller et al. 2014).

1.1.1 The Importance of Metal-Poor Stars

The study of metal-poor stars can provide key insights into several aspects of galaxy formation and the early epochs of the universe. They can be used to test the IMF of high-mass stars, the earliest chemical evolution of galaxies, and supernova yields. Due to the scarcity of the HMP and more metal-poor stars, this parameter space is not well understood.

The initial element abundances of the universe are not directly measurable. Metal-poor stars hold information on the chemical enrichment that occurred prior to their formation, which can be used to model the production of elements in the early universe. There are several different methods by which stars form their elements, from alpha elements created in helium burning stars, to the iron peak elements found in the cores of massive stars, to s- and r- process neutron-capture elements. The heavier elements that are produced during explosive supernovae are one of the better tracers of the predecessor population of stars.

The r- and s- processes are neutron capture mechanisms that allow for the formation of heavy elements. The r- process (rapid) produces heavy elements through the rapid capture of neutrons and subsequent β^- decay. This process requires a neutron-rich environment and primarily occurs during extreme events, like core-

collapse supernovae (Meyer 1994). The s- process (slow) allows for decays of the nucleus between neutron captures, and requires far less extreme environments when compared to the r- process. The s- process elements primarily form in AGB stars during helium burning phases (Meyer 1994).

In the most ancient metal-poor stars, very little chemical enrichment occurred prior to their formation. The chemical enrichment in these particular stars is primarily from the supernovae (SNe) of the preceding stellar populations mixing with the interstellar medium. At most, only a few SNe contributed to the heavy element content of the most metal-poor stars (McWilliam et al. 1995; Keller et al. 2014). By comparison to models that predict the heavy elements produced during SNe, the abundance patterns in these stars can indicate the conditions under which the progenitor stars created and distributed heavy elements (Shigeyama et al. 2000).

The ability to determine the early metal formation (specifically r- and s-process elements) rates is particularly useful in modelling supernova element production and testing the very end stages of a star's lifecycle. Aoki et al. (2013) tested models' ability to reproduce element abundance trends seen in metal-poor stars and found that the element abundance trends within EMP stars were indicative of a 'truncated r-process', in which the progenitor star initially forms as a neutron star, and then collapses through accretion to form a black hole. Observations of metal-poor stars by Yong et al. (2013a) suggest that there are an additional two methods by which heavy elements are formed other than the r-process.

Although metal-poor stars are classified as such through their relative lack of iron, they tend to exhibit relative overabundances of other elements compared

to iron[2]. For many elements, [X/Fe] is relatively constant for a majority of a star's life, barring any external contribution. Each nucleosynthetic process that occurs in a star will contribute to the enrichment of only a few elements. The [X/Fe] abundance trends in metal-poor stars can be useful in testing the processes that formed those elements (e.g. Spite et al. (2018)). The measurement of these abundances is particularly useful for elements that are commonly associated with high energy events like supernovae.

Several neutron-capture elements show consistent overabundances in metal-poor stars. The measured abundances of barium and europium are key indicators of neutron capture production, with the value of [Ba/Eu] changing dramatically between stars that formed elements under s-process and those that formed elements under r-process (Beers & Christlieb 2005). The variation in abundance patterns in metal-poor stars has indicated that if r-process elements are overabundant, then the stars were likely produced by low mass type-II supernovae (McWilliam et al. 1995).

The abundance of these r-process elements can determine the age of the star, in particular, thorium and uranium. Finding metal-poor stars with measurable r-process elements can help constrain the ages of the stellar populations to which these metal-poor stars belong, as they are some of the oldest stars in those populations (Sneden et al. 2001).

Approximately 20% of stars with [Fe/H] < -2.0 have an overabundance of carbon (Rossi et al. 2005), with a similar fraction below [Fe/H] < -3.0 (Yong et al. 2013b). Given this trend is frequent in the metal-poor star population, under the nomenclature of Beers & Christlieb (2005), any star with carbon overabundances

[2]The abundance ratio is represented by [X/Fe], where X represents any element other than hydrogen or helium, and is calculated similarly to [Fe/H] in Equation 1.1.

of [C/Fe] $> +1.0$ is termed a carbon-enhanced metal-poor (CEMP) star[3].

Due to the small number of HMP- class stars currently known, the abundance ratios of other elements at the low metallicity scale are not determined. Only a few stars are currently known with metallicities below [Fe/H] $= -5.0$, two of which have metallicities of [Fe/H] $= -5.3$ (Christlieb et al. 2004a), and [Fe/H] $= -5.4$ (Frebel et al. 2005). Both of these stars are CEMP stars, having large overabundances of carbon, with [C/Fe] $\approx +4.0$. In the most metal-poor star currently known, with an estimated metallicity of [Fe/H] $\leqslant -6.53$ (Nordlander et al. 2017), the abundance trends indicate that the star appears to have been enriched by at most only a few low-energy supernovae (Keller et al. 2014).

To understand galaxy formation, knowledge of the distribution of masses of the first stars is important. This mass distribution is known as the initial mass function (IMF) and represents the range of masses over which stars enter the main sequence. Metal-poor stars play an important role in constraining the IMF at low metallicities. Indeed, studies suggest that the IMF of galaxies is skewed, with a majority of the early stars having high masses, and any low-mass stars potentially forming as binaries (Tumlinson 2007b). The link between CEMP stars and the extremes of the metallicity scale are linked to the IMF by how these low-mass stars are able to form. There is a threshold of C and O required to form low-mass stars in the early Universe, as these elements provide a cooling mechanism for the gases to form low-mass stars (Bromm 2013). Therefore, any stars extremely low in metallicity at low mass must have formed from a gas above these critical thresholds of [C/H] $= -3.5$ and [O/H] $= -3.0$.

The low-mass end of the IMF can be used to understand the way in which the cosmic microwave background (CMB) has changed with time. As the CMB changes,

[3]Under nomenclature suggested by Beers & Christlieb (2005)

the minimum temperature of gases also changes. Metallicity affects the temperatures at which stars can form from gas (through cooling), hence the IMF would change as the CMB changes. Using the results from Abel et al. (2002) and Bromm et al. (2002), Tumlinson (2007a) showed that there was a relation between the CMB and the IMF and found indications that the CMB has an effect on the masses of stars formed early in the Galaxy.

Another of the important characteristics of a galaxy to understand is the proportion of stars that exist at given metallicities, described by the MDF. The MDF can be used to test the ability of stellar formation models to replicate observed trends. The MDF can also provide estimates for the proportion of peculiar metal-poor stars (such as CEMPs) (Yong et al. 2013b). Because stars become increasingly scarce at lower metallicities, the low metallicity end of the MDF is not well understood.

Understanding the way in which the most metal-poor stars (UMP and HMP) received their metal enrichment provides information about the Population III stars - the first stars that formed in their galaxy. The observations of these UMP and HMP stars can help constrain the MDF of Population III stars, and the star formation rate when Population II stars were beginning to form (Rollinde et al. 2009).

There is a wealth of knowledge that can be gained from studying metal-poor stars, and as such, the discovery of new metal-poor stars is important. Unfortunately, metal-poor stars become increasingly rare as metallicity decreases, with only a handful existing in the HMP category. Filling this parameter space will be invaluable for testing the conclusions based on the small number of these presently known stars.

1.2 The Large Magellanic Cloud

There have been extensive studies looking for metal-poor stars in the Milky Way and its metal-poor satellites. The dwarf spheroidal galaxies Fornax, Sculptor and Sextans have confirmed EMP stars resulting from the surveys of these satellites (Tafelmeyer et al. 2010). However, there hasn't been much work on our nearest significant mass neighbour, which we have reason to believe would be an excellent place to search for EMP stars.

The Large Magellanic Cloud (LMC) is one of the Milky Way's satellite galaxies. With a mass of between $M = 10^{10}$ $M_\odot$ and $M = 10^{11}$ $M_\odot$ (van der Marel et al. 2002; Laporte et al. 2018) (between 1% and 10% of the Milky Way's mass), it is classified as a barred late-type spiral. The galaxy formed approximately 13 Gyr ago and had formed about half of its stars between 5 and 7 Gyr ago (Weisz et al. 2013). Observation of the LMC is relatively easy, as we view it from almost directly face-on. Studies of the LMC are important as they provide comparisons for Galactic formation models, and help in understanding galaxies with companions such as our own (Robotham et al. 2012).

The distance to the LMC is now well determined by Pietrzyński et al. (2013), who used eclipsing binary systems to constrain the distance to approximately 2%. The LMC distance was determined to be $d_{LMC} = 49.96 \pm 1.11$ kpc. The proximity of the LMC has allowed for a great number of studies into its evolution and composition, and as such, is one of the Milky Way's most studied satellite galaxies.

Tidal interactions between the LMC and the Milky Way, and between the LMC and Small Magellanic Cloud (SMC) have both played a part in the star formation history (SFH) of the LMC (Bekki & Chiba 2005; Rubele et al. 2012; Kallivayalil

et al. 2013). An interaction between the LMC and the MW appears to have occurred approximately 3-5 Gyr ago, which is around the time when the LMC bar formed (Cole et al. 2005), corresponding to a burst in SMC star formation (Cignoni et al. 2012). The LMC-SMC system had its closest approach with the MW approximately 1 Gyr ago, and the LMC - SMC system has an orbital period of $\sim$ 1 Gyr, with the most recent interaction between 150 Myr and 200 Myr ago (Kallivayalil et al. 2013).

For recent star formation events in the LMC (i.e. over the past $\sim$ 2 Gyr, starting about 3 Gyr ago), there are observed coincident events in the SMC, further supporting interaction-induced star formation (Harris & Zaritsky 2009; Weisz et al. 2013). Although there has been star formation throughout the history of the LMC, the star formation rate between 12 and 5 Gyr was relatively quiescent, a trend that is shared by the SMC (Weisz et al. 2013).

The quiescent period of star formation is accompanied by a lack of globular cluster formation. Nearly all of the globular clusters observed in the LMC were formed around 13 Gyr ago, or in the past 3 Gyr, with only one cluster observed of intermediate age (Da Costa 1991). The formation of new clusters 3 Gyr ago coincides with a peak in the SFR, possibly due to an LMC-SMC interaction. The cluster age gap is of interest because the cluster and field star populations share a similar age-metallicity relationship (AMR), with the field star formation continuing during the age gap (Geha et al. 1998). By comparison, the SMC has a distribution of cluster ages extending back to its oldest clusters (Da Costa 1991). The cluster population is analogous to the Milky Way's cluster population (Harris & Zaritsky 2009) (with the exception of the cluster age gap), with the notable exception of massive young clusters that have formed as a result of the tidal interactions between the SMC-LMC and LMC-MW.

The AMR of various populations within the LMC have been studied by several authors (e.g. Cole et al. (2005); Carrera et al. (2011); Piatti et al. (2012)). Based on the AMR derived from red giant stars in the central bar, Cole et al. (2005) noted a lack of chemical evolution during the cluster age gap (i.e. the AMR was flat during this epoch). From the study of Cole et al. (2005), the majority of red giants in the bar have mean metallicity [Fe/H] = −0.4, with a distribution extending down past [Fe/H] < −2.0. Piatti et al. (2012) used wide-field Washington photometry covering a majority of the galaxy with the purpose of establishing an AMR (Piatti & Geisler 2013). The results of Piatti & Geisler (2013) found that the cluster AMR at the ancient ages acted as a lower limit to the field population AMR. There are indications that the initial chemical enrichment rate was quite steep, reaching a value of [Fe/H] = −1.0 within the first 2-3 Gyr (Carrera et al. 2011). A list of common age and metallicity tracers is given in Table 1.2.

Table 1.2: A few of the metallicity and age tracers in the LMC, given is the mean metallicity of these populations.

Tracer	**Metallicity** [Fe/H]	**Age** Gyr	**Refs**[a]
Young Globular Clusters	−0.4	< 2.5 Gyr	Piatti et al. (2018a)
RR Lyrae	−1.5	> 10 Gyr	Haschke et al. (2012)
Old Red Giants	−0.4	> 10 Gyr	Cole et al. (2005)

[a] Example references for the values given in this table.

From the trends of alpha elements observed in the LMC, it is likely that the primary source of chemical enrichment is from type Ia supernovae[4] (Van der

[4]Type Ia supernovae are caused by accretion onto white dwarf stars from a binary partner, causing them to exceed the Chandrasekhar limit of M = $1.44 M_{\odot}$.

Swaelmen et al. 2012b). The domination of enrichment from type Ia supernovae occurs at lower metallicities than is seen to occur in the Milky Way (Van der Swaelmen et al. 2012a). Through an analysis of the chemical enrichment history of the LMC, Van der Swaelmen et al. (2013) concluded that massive stars had less of a contribution to the total enrichment of the galaxy than they do in the Milky Way. Also observed in the study of Van der Swaelmen et al. (2013) was a difference in abundance patterns for the disk and bar stars.

1.2.1 Metal-Poor Stars in the LMC

There have been very few studies focussing on finding individual metal-poor stars within the LMC. Currently, there are only a handful of stars known with metallicity [Fe/H] < -2.0 (Cole et al. 2005; Carrera et al. 2011; Van der Swaelmen et al. 2013). Measurements of RR Lyrae stars have yielded one of the lowest metallicity objects known in the LMC (albeit with some degree of uncertainty due to the faintness and variability of the star), with reported [Fe/H] $= -2.7$ (Haschke et al. 2012).

Beyond these few examples, there have been no large attempts to delve into the metal-poor side of the MDF beyond [Fe/H] $= -2.0$. Many wide-scale surveys are performed in broadband systems, which have little sensitivity to changes in metallicity below this threshold. If the relationship between the metallicity and the frequency of metal-poor stars as described in Norris (2004) holds true in the LMC, then we can make a guess at the frequency of EMP class stars among the LMC's giant population. Given the distribution of red giant stars in the LMC as observed by Cole et al. (2005), we can expect roughly 1 out of every 2000 RGB

stars to be classed as EMP or more metal-poor[5].

The low line of sight reddening and the well-determined distance make the LMC a suitable place to search for EMP stars, as we can see down to the centre of the galaxy from the outside, unlike our views into the MW bulge. These central regions are likely to have the greatest proportion of metal-poor stars, due to their distribution (Tumlinson 2010).

It is not well known if the low metallicity scale of the LMC reflects what is seen in the MW. From this project, we expect to expand the lowest region of the MDF, probing below [Fe/H] $= -2.0$ to fill in this parameter space for the LMC.

[5]Assume the frequency of metal-poor stars follows a power-law distribution when the metallicity is less than [Fe/H] $\leqslant -0.7$, which in Cole et al. (2005), accounted for 10% of the red giant population. Then, for a star with at least [Fe/H] $= -3.0$, we have

$$\frac{0.10}{\int_{-\infty}^{-0.7} 10^x dx} \int_{-\infty}^{-3} 10^x dx \approx 0.0005$$

where x is [Fe/H]. This corresponds to seeing one EMP star out of every 2000 RGB stars.

Chapter 2

Photometric Survey

This study takes inspiration from Anthony-Twarog & Twarog (1998), wherein the use of a narrowband filter in combination with the broadband Strömgren *uvby* filter system was shown to be a good tracer of metallicity, showing good metallicity sensitivity and a low false positive rate as confirmed with spectroscopy (Anthony-Twarog et al. 2000).

Broadband photometric colours begin to lose sensitivity to changes in metallicity around [Fe/H] = −2.0. The Washington CMT_1T_2 filter system was designed to provide better temperature and metal abundances for G & K giant stars (Canterna 1976). This photometric system has been proven to be a good metallicity indicator when compared to other photometric systems, achieving some results down to a metallicity of [Fe/H] ≈ −2.5 (Geisler et al. 1991).

Instead of the Strömgren filters, we are using the Washington C & M filters with Cousins R & I as substitutes for Washington T_1 & T_2 (Geisler 1996). In a fashion similar to Anthony-Twarog & Twarog (1998), we establish an index for the differentiation of metallicity. We will define our measure as the HK index:

$$\mathrm{HK} = (\mathrm{Ca\,II} - \mathrm{M}) - (\mathrm{M} - \mathrm{R}) \tag{2.1}$$

We show the ability of this HK index to differentiate metallicities below [Fe/H] = −3.0 in Figure 2.1. The Washington and Cousins filter predictions were obtained from MIST isochrone grids (Dotter 2016; Choi et al. 2016; Paxton et al. 2011, 2013, 2015), and the calcium filter data were acquired from ATLAS model atmosphere grids (Kurucz 1970). The calcium filter magnitude was estimated by interpolating between grid values at the given metallicities for the corresponding MIST T_{eff} and log g.

To demonstrate the increase in the sensitivity of a photometric system paired with a narrowband filter, we compare Figure 2.1 to Figure 2.2. In Figure 2.2, we have taken the SkyMapper v filter as a representative calcium filter, and have constructed the HK index as in equation 2.1 using MIST isochrone grids. The SkyMapper v filter has a central wavelength of λ = 384nm with $\Delta\lambda$ = 28 nm (Bessell et al. 2011), which is slightly bluer and wider than the one used in this study. From this figure, we see that using a wider filter can result in a loss of sensitivity[1] below [Fe/H] = −3.0.

[1]SkyMapper uses a different metric to determine metallicity in their surveys. This example is only a comparison of the physical properties of the filter used in constructing our HK index.

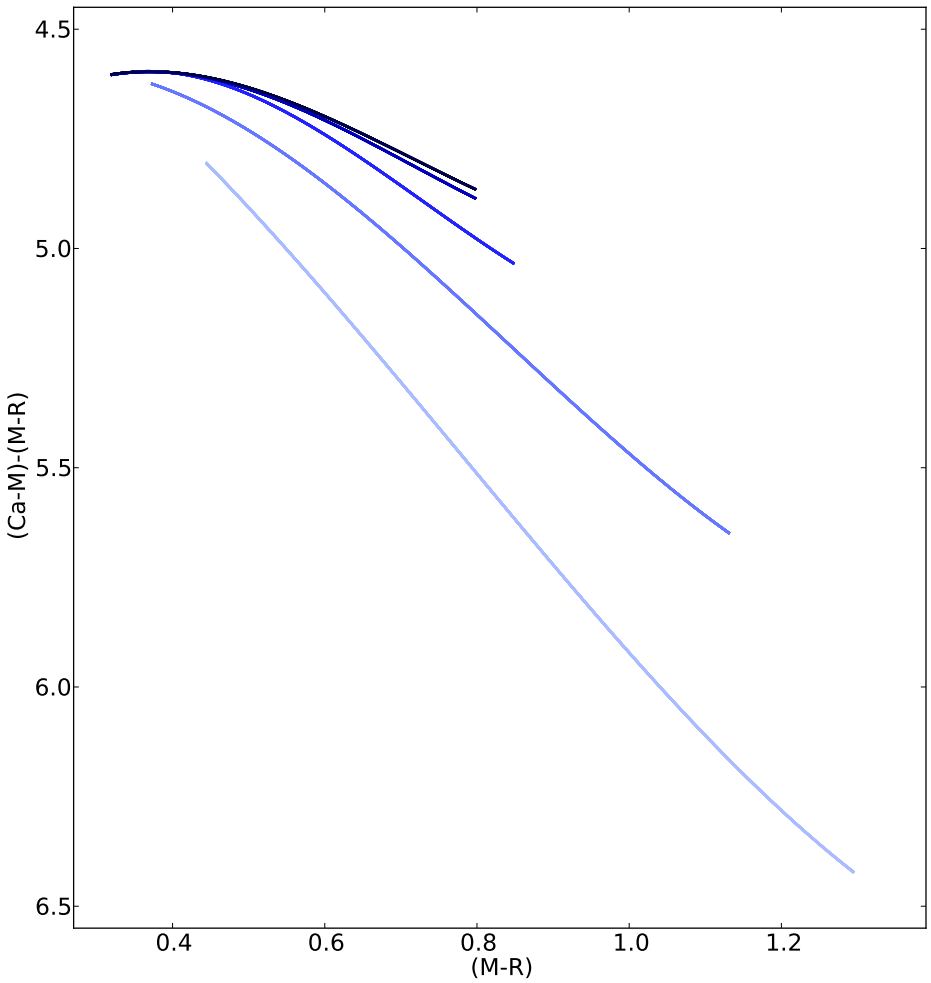

Figure 2.1: HK index against (M-R) colour using MIST isochrones with Kurucz model atmospheres to estimate the Ca II filter magnitudes. The tracks have metallicities of [Fe/H] $= -1.0, -2.0, -3.0, -4.0$, and -5.0, from lightest to darkest, respectively. All isochrones have an age of 13 Gyr.

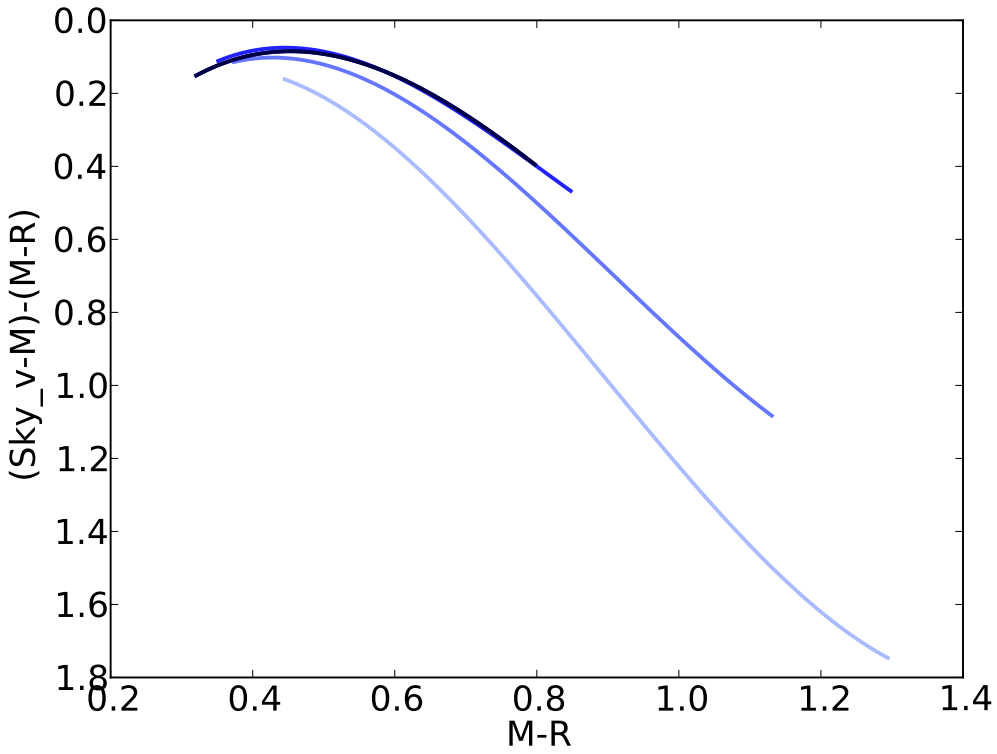

Figure 2.2: Skymapper v HK index against (M-R) colour using MIST isochrones. The tracks have metallicities of [Fe/H] $= -1.0, -2.0, -3.0, -4.0$, and -5.0, from lightest to darkest, respectively. All isochrones have an age of 13 Gyr. In this example, the isochrones become degenerate at [Fe/H] $= -3.0$.

2.1 Observations

The photometric data were taken by Andrew Cole and Doug Geisler during the nights of the 27th to the 31st of December 2008 with the 4-m Blanco telescope at the Cerro Tololo Inter-American Observatory (CTIO) using the MOSAIC-II CCD imager. The MOSAIC-II detector consists of eight 2048 $\times$ 2048 pixel SITe CCDs, with a pixel scale of 0.27" per pixel. A total of 15 science fields were observed

over the four nights, each covering an area of $36' \times 36'$, for a total observational area of 5.4 square degrees. The seeing for the observations varied between 0.6" and 1.7", with a typical value of $\sim$ 1". Airmass varied between $\sim$ 1.1 and 1.7. In addition to these observations, partial data[2] for some of the science fields were obtained a week prior (on the 21st of December) by Doug Geisler. These additional observations were combined with the primary data in the analysis.

In addition to the C, M, R & I filters, the fields were also observed with the DDO51 filter, which is centred on the Mgb and MgH lines at $\lambda \sim 515$nm. This filter can be used in conjunction with our M and I filters to help screen for unwanted foreground contaminants (Majewski et al. 2000) based on surface gravity.

The sixth filter used to observe our fields is a custom-built narrowband filter, centred on the Ca II H & K lines. The filter was manufactured by Omega Optical with a central wavelength of $\lambda = 396.5 \pm 2$nm, and a FWHM of 9 ± 2nm. The filter was specified to have a transmissivity of at least 50% at the central wavelength. The measured bandpass of the filter is shown in Figure 2.3 with some example spectra at different metallicities, showing the change in the H & K lines as the metal content decreases.

The science fields were aligned along the bar of the LMC, in the direction of the greatest falloff in stellar density, shown in Figure 2.4. The innermost field covers the same region observed in Cole et al. (2005), which we will use as a metallicity calibration between [Fe/H] = -0.4 and -2.0 for our data. This field also contains the metal-poor globular cluster NGC1939, which has a metallicity of [Fe/H] = -2.10 ± 0.19 (Mackey & Gilmore 2004). In the inner fields, we expect a stellar density of $\sim$ 1000 red giant branch (RGB) stars per square degree, decreasing to only $\sim$ 20 RGB stars per square degree in the outermost field

[2]Only data for the Washington C, and Cousins R & I filters were obtained.

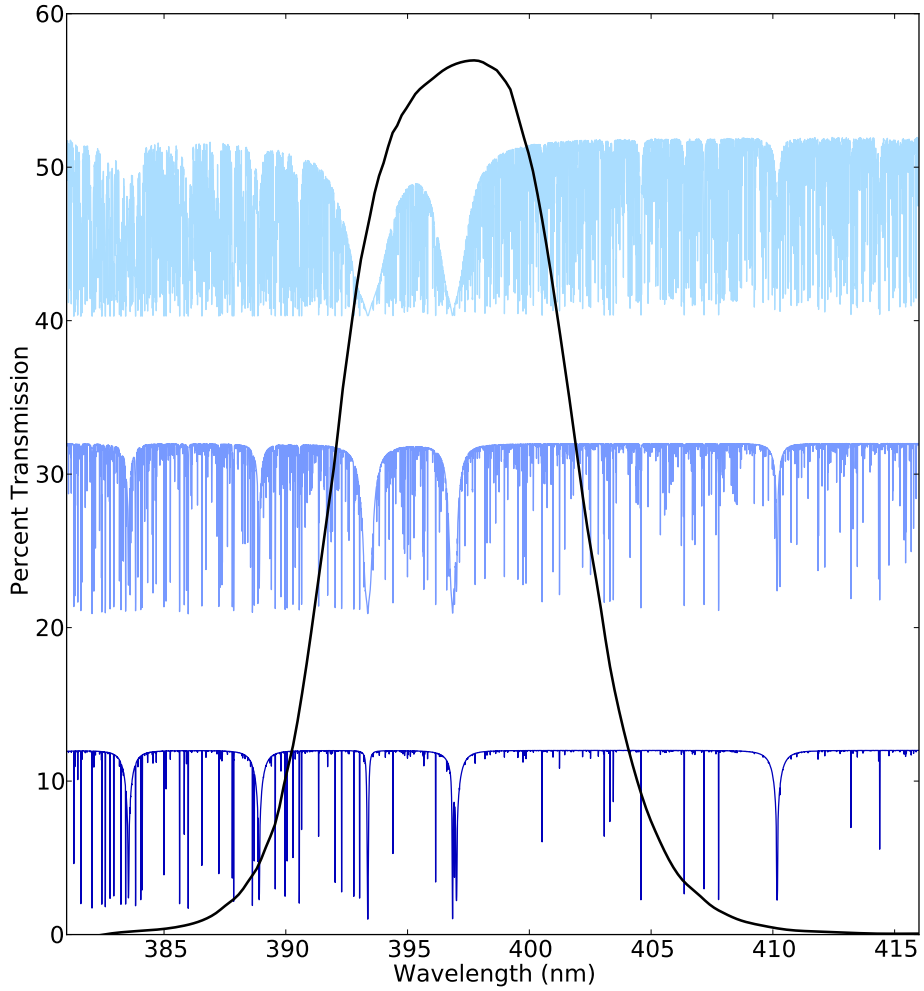

Figure 2.3: The transmissivity of the Omega Optical Ca II filter superimposed over POLLUX synthetic spectra (Palacios et al. 2010). The spectra have [Fe/H] = 1.0, 2.5, and 4.0, and T_{eff} = 5000, 5250, and 5500 from top to bottom, respectively. All three spectra have log g of 2.5.

(Nikolaev & Weinberg 2000).

For each night, a selection of calibration sources was observed, listed in Table 2.1, with the full list of observations given in Tables A.1 to A.3. The standard star fields PG0321, SA 98, SA 101, and NGC 3680 are the standard fields from Geisler (1996) and are used to calibrate the photometric system. The metal-poor star fields were offset from the star of interest by $2'$ N and $2'$ E, to ensure that the target wouldn't land in the gap between chips. These metal-poor calibration fields are useful for testing the candidate selection techniques detailed in section 2.2. The remaining cluster standard fields cover a range of metallicities between [Fe/H] = -0.7 and [Fe/H] = -2.2.

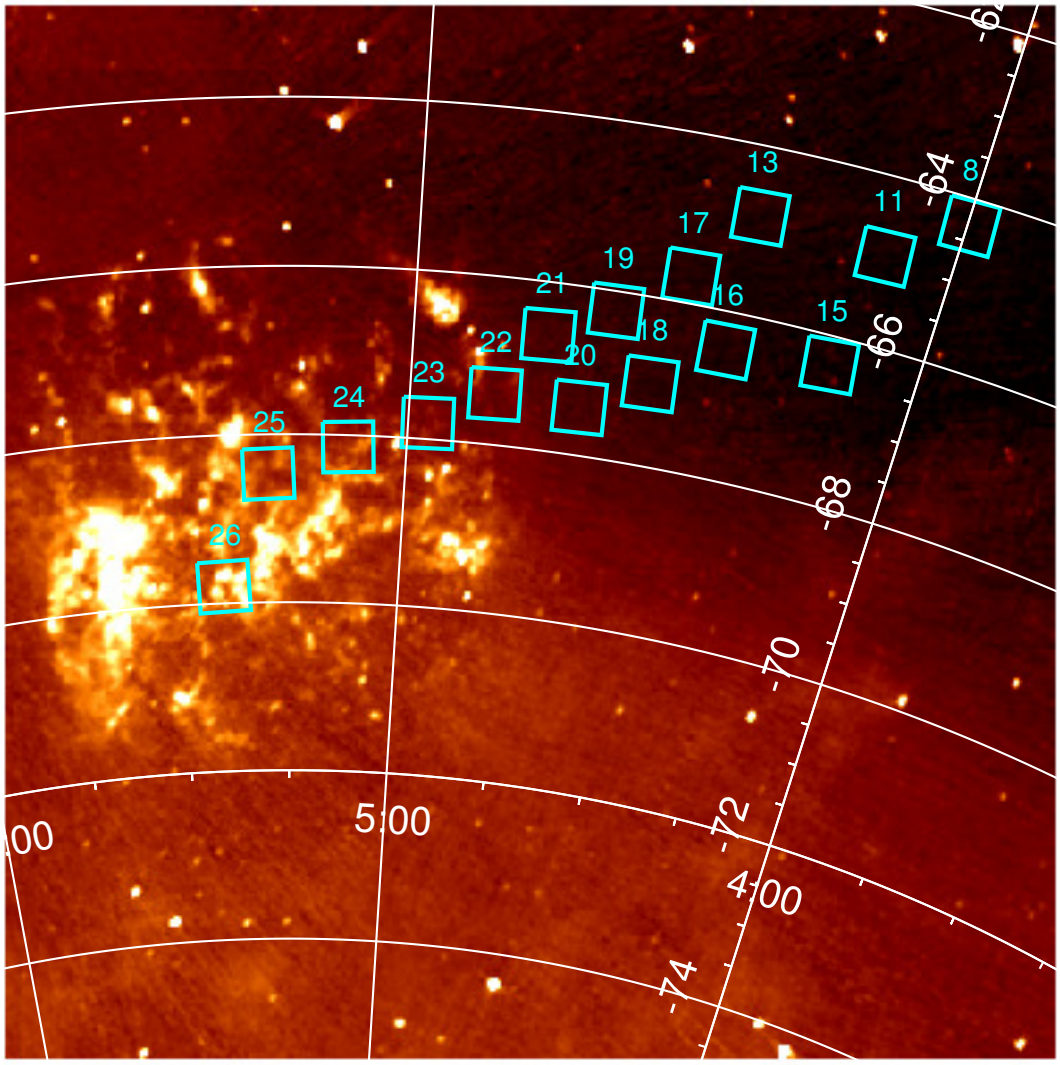

Figure 2.4: Positions of the fields observed within the LMC.

Table 2.1: Calibration fields observed at CTIO

Field Name	**Purpose**	**[Fe/H]**	**RA**	**Dec**
NGC 1851	Cluster Standard	-1.18[a]	$05^h\ 14^m\ 06^s$	$-40^\circ\ 02'\ 50''$
NGC 1904	Cluster Standard	-1.58[a]	$05^h\ 24^m\ 11^s$	$-24^\circ\ 31'\ 27''$
NGC 4590	Cluster Standard	-2.27[a]	$12^h\ 39^m\ 28^s$	$-26^\circ\ 44'\ 33''$
47 Tuc	Cluster Standard	-0.76[a]	$00^h\ 24^m\ 05^s$	$-72^\circ\ 04'\ 51''$
Mel 66	Cluster Standard	-0.32[b]	$07^h\ 26^m\ 23^s$	$-47^\circ\ 40'\ 00''$
HE 0044-3755	Metal-Poor Star	-4.0[c]	$00^h\ 46^m\ 46^s$	$-37^\circ\ 37'\ 34''$
HE 0107-5240	Metal-Poor Star	-5.2[d]	$01^h\ 09^m\ 42^s$	$-52^\circ\ 22'\ 34''$
HE 0305-5442	Metal-Poor Star	-3.6[e]	$03^h\ 06^m\ 42^s$	$-54^\circ\ 28'\ 32''$
HE 0557-4840	Metal-Poor Star	-4.75[f]	$05^h\ 58^m\ 41^s$	$-48^\circ\ 37'\ 57''$

[a] Dalessandro et al. (2012)

[b] Netopil et al. (2016)

[c] François et al. (2003)

[d] Christlieb et al. (2004b)

[e] Cayrel et al. (2004)

[f] Norris et al. (2007)

2.2 Data Analysis

On each night, a set of bias, dark and flat field images was taken to perform standard CCD basic calibration. All image reduction was done using the IRAF[3] mosaic reduction package `mscred`. The 10 bias images from each night were

[3]IRAF is distributed by the National Optical Astronomy Observatory, which is operated by the Association of Universities for Research in Astronomy (AURA) under a cooperative agreement with the National Science Foundation.

averaged together, rejecting the minimum and maximum pixel values from the image sets to account for cosmic ray interference. For each filter, 5 dome flats were combined, rejecting pixels more than 3σ from the median level.

The sky flats were constructed using many non-crowded images, which were averaged together rejecting pixels based on the readnoise and gain of the CCD, given by:

$$\sigma = \sqrt{\left(\frac{RN}{Gain}\right)^2 + \frac{\langle I \rangle}{Gain} + \left(s \times \langle I \rangle\right)^2} \tag{2.2}$$

Where $\langle I \rangle$ is the pixel value, RN is the readnoise, and s is the sensitivity noise. The range of acceptable values from the median is then calculated on a per-pixel basis, with rejection occurring if the pixel value is below 5σ, or above 2.5σ.

The science frames then were corrected based on the bias and the dome flat fields using the `ccdproc` task in `mscred`. These images were then processed once more, applying the corrections from the sky flats. In this process, `ccdproc` automatically performs trimming of the overscan regions in the frame and corrects for any crosstalk between CCD chips on the same amplifier.

Each amplifier was then merged in IRAF, and the multi-extension fits image split into individual fits images for each amplifier for the following steps of the data reduction.

The reduced data was then processed using the PHOTRED and STDRED packages, first described in Nidever et al. (2011). These IDL scripts make use of Peter Stetson's DAOPHOT and ALLFRAME packages (Stetson 1987, 1994) to reduce crowded photometric fields. STDRED was used to calculate the appropriate transformation equations for each night's data. PHOTRED was used to batch process the outer fields (RA $< 4^h30^m$), but was unable to process the inner

fields[4]. PHOTRED was used to estimate the required aperture corrections for all observed fields.

To ensure correctly combined images, these outer fields required processing in two batches, 'long' exposures (C, Ca II, and DDO51 filters), and 'short' exposures (I, R and M filters). The results from these reductions were then combined by aligning the frames using the stellar positions calculated by PHOTRED. There was a far greater number of stars identified in the I, R, and M exposures, which could not be included in the combined file, as the analysis required detections in four of the six filters (I, R, M, and Ca II).

The remaining fields were reduced by hand in DAOPHOT. The coordinates of the stars in each filter were matched to the corresponding stars, using the I filter as a reference. The positions of stars were allowed to vary by up to the average PSF of the filter being matched. The resultant file was the best symmetric match between the I filter and other filters, requiring matches in the above four filters. It is worth noting that allowing the coordinates to vary will introduce some erroneous matches.

The data were transformed to a standard photometric system using equations of the following form:

$$R = R_{inst} - c_1 \times (R_{inst} - I_{inst}) - c_2 \times AM - R_0 + AP_R + 2.5 \log_{10} t_R \qquad (2.3)$$

Where c_1 is the colour coefficient, c_2 is the airmass coefficient, R_0 is the zero-point offset for filter R, AP_R is the aperture correction for filter R, and t_R is the exposure time. The colours used for the calibrations are (R-I) for Cousins R &

[4]Fields LMC20 and closer to the centre of the LMC suffered data quality issues in the output of PHOTRED, potentially due to the rapidly increasing stellar density.

I, (C-M) for Washington C & M, and (Ca-C) for the Ca II filter. The DDO51 filter did not have information in all of the standard fields that were observed, so a reliable transformation equation could not be calculated using PHOTRED. Any analyses following that use the DDO51 filter are thus utilising instrumental values.

The data were then dereddened, using values from Schlegel et al. (1998) for I & R, and O'Donnell (1994) for C & M. The reddening in the Ca II filter is calculated using the same coefficient used for the C filter. The reddening towards the LMC is relatively low, with E(B - V) $\approx$ 0.06 (from Schlegel et al. (1998)). While this value will be appropriate for the outer fields, the inner fields have additional variation from line-of-sight reddening within the LMC disk. The reddening in the inner fields is still quite low, but can vary by up to E(B - V) $\approx$ 0.1 (Haschke et al. 2011).

Because the LMC lies at a distance of 50 kpc, and the LMC is viewed nearly face-on, we do not need to consider strong distance effects on individual stars within a field. However, due to the distance, and the high degree of crowding in our fields, we concentrate on the detection of RGB stars. To select these stars, visual inspection of an I vs (R-I) colour-magnitude diagram (CMD) is used, and constraints are placed on the data to analyse.

One issue to consider with this technique is the inclusion of MW foreground dwarf stars, which will occupy a similar region in the CMD. Majewski et al. (2000) detailed a method using Washington photometry in conjunction with DDO51 to distinguish between stars with high surface gravity (main-sequence), and those with low surface gravity (giant stars). We adopted this technique but allowed a more relaxed cutoff range to allow for the large scatter in the data, rejecting only the most obvious contaminants (and some with unreliable photometry). We show

an example of this in Figure 2.5, which contains all of the valid data[5] from field 13.

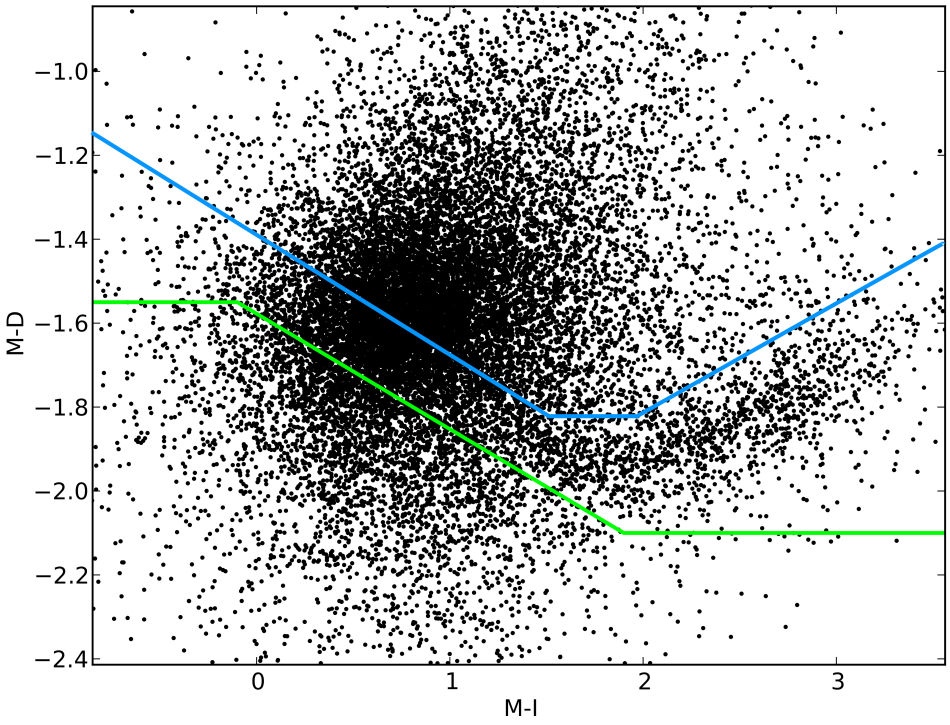

Figure 2.5: Example colour-colour plot used to reject obvious foreground stars. The blue line is approximately where the relation from Majewski et al. (2000) falls, which separates the giants (above the curve) from the dwarfs (below the curve). The green line is our rejection threshold, with any stars above this line being included in the candidate selection plots. Our rejection threshold is lowered to account for poorer quality photometry in the DDO51 filter. The 'tail' feature seen in this plot mainly consists of MW foreground objects, but may contain some number of RGB stars of interest.

Once the RGB stars are selected, they are plotted on the HK colour-colour plot.

[5]Excludes data from amplifier 6 due to poor data quality.

Stars in this plot should occupy a narrow region on the diagram corresponding to the age and metallicity of the mean of the LMC RGB population. Practically, these stars will have some random errors associated with the photometry, and some systematic errors associated with the reduction process. As the metal-poor stars we are interested in are going to occupy specific areas in relation to the main body of stars, we can greatly reduce the effects of the systematic errors by looking at the positions of stars with respect to the population mean.

To look at the positions of stars with respect to the mean, we need to get an idea of the mean stellar population. To do this, we define a region around the densest population of stars and fit a third order polynomial to the data using 2-dimensional weighted least-squares. The third order polynomial was chosen to mimic the general shape of the metal-poor stars in HK space without being influenced too greatly by outliers. The results of doing this in our most densely populated field are shown in Figure 2.6, in which we have defined the fit to the region that contains 50% of the data.

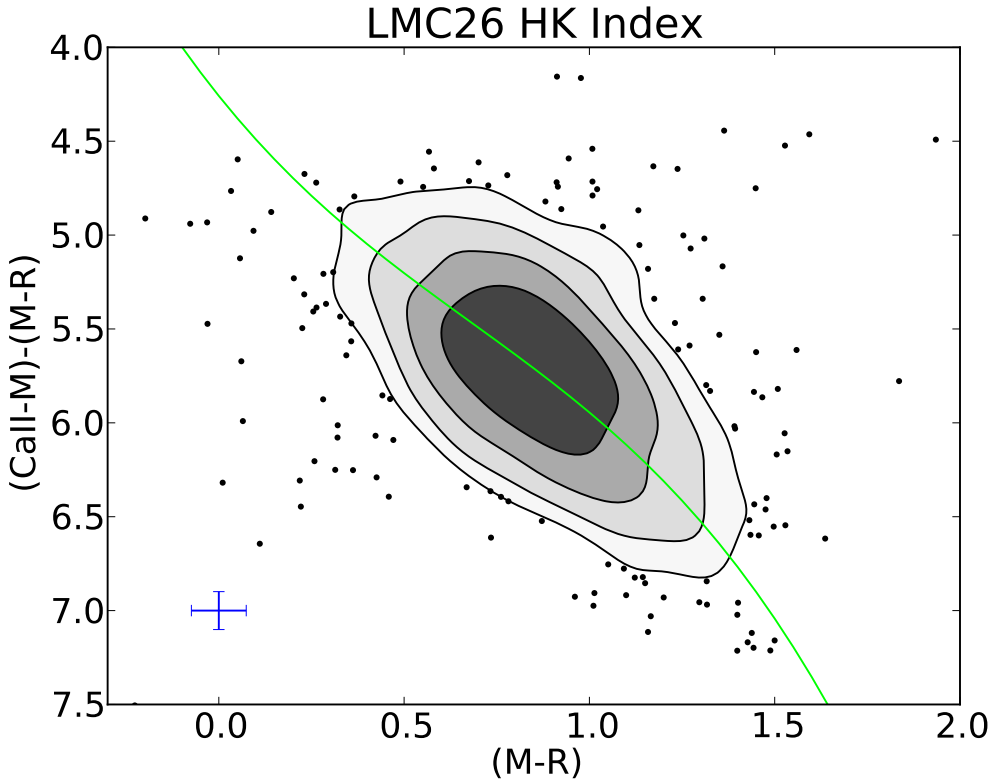

Figure 2.6: Example HK Diagram showing fit to the region (in green) containing the densest region of stars for a single amplifier LMC 26. The contour regions contain 93.75%, 87.5%, 75% and 50% of stars from lightest to darkest, respectively. Typical error bars for these data are given in the bottom-left.

We want to check that the selection of the region doesn't greatly influence the selection of candidate metal-poor stars, so we have shown an example of taking a larger proportion of the stars in Figure 2.7. Over the range of colours we are likely to find metal-poor stars, the difference between the two fits tends to be small. The region selection only begins to have a large effect at the extremes in (M-R), areas in which we are unlikely to find metal-poor stars, as shown in 2.8.

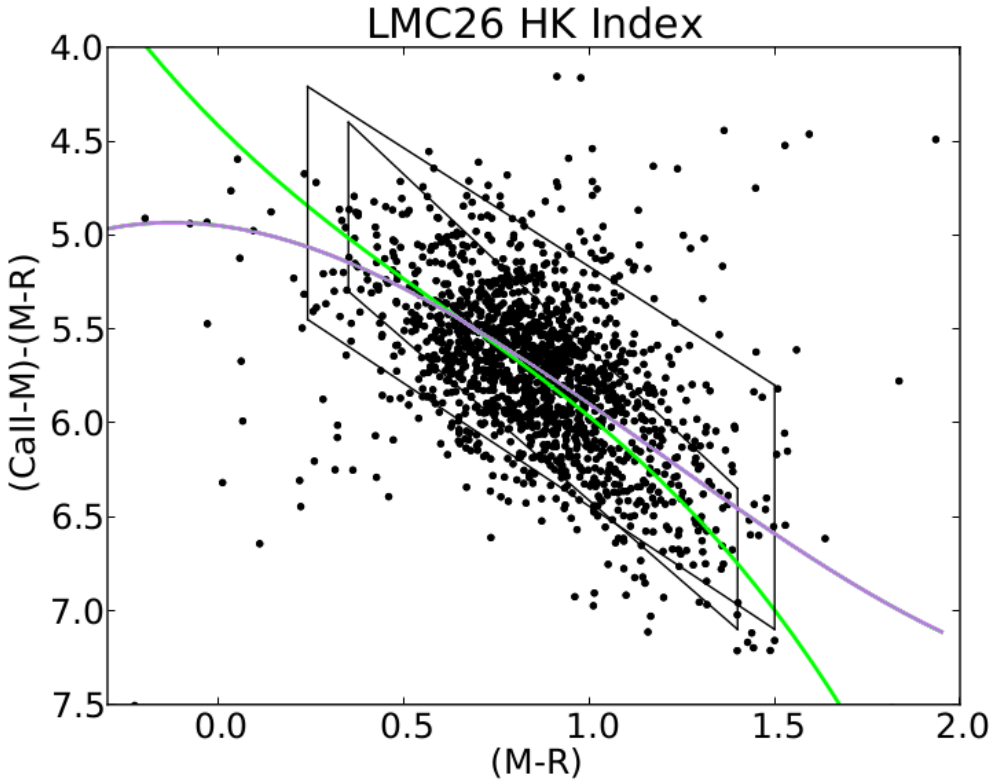

Figure 2.7: Same region as shown in Figure 2.6, without the contours. The two black parallelograms are the defined regions for the fits. The light green fit is from the strict region selection (used above), and the purple fit is from the more accommodating region selection.

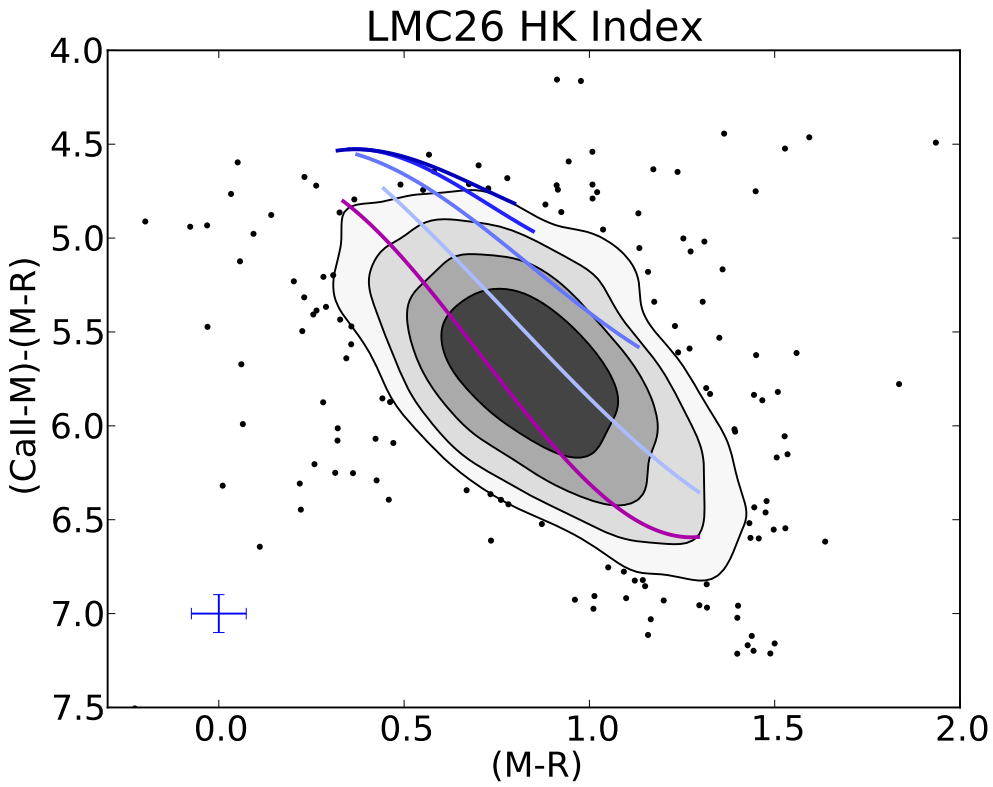

Figure 2.8: HK from WISE isochrones and interpolated ATLAS model atmosphere grids overlaid on the region shown in 2.6. Purple is an approximate typical LMC isochrone with Age = 4 Gyr, [Fe/H] = −0.5; the blue isochrones begin at [Fe/H] = −1.0 and decrease in steps of 1 dex, to [Fe/H] = −4.0, with more metal-poor isochrones being darker. Contour levels are the same as in Figure 2.6

Using this technique, we can then measure the HK separation from the mean of the population, giving us a rough idea of the metallicity compared to the rest of the observed stars. Subtracting the fit from the data yields Figure 2.9, in which we have included the isochrones from Figure 2.8. In this step, we also measure the spread of the entire population (not just the region selected for the fit) to categorise the stars. For our example (LMC26, amplifier 3), stars that had an HK index over 1.8σ from the fit fell more metal-poor than [Fe/H] = −2.0. This

is the metric by which we identify our metal-poor candidates.

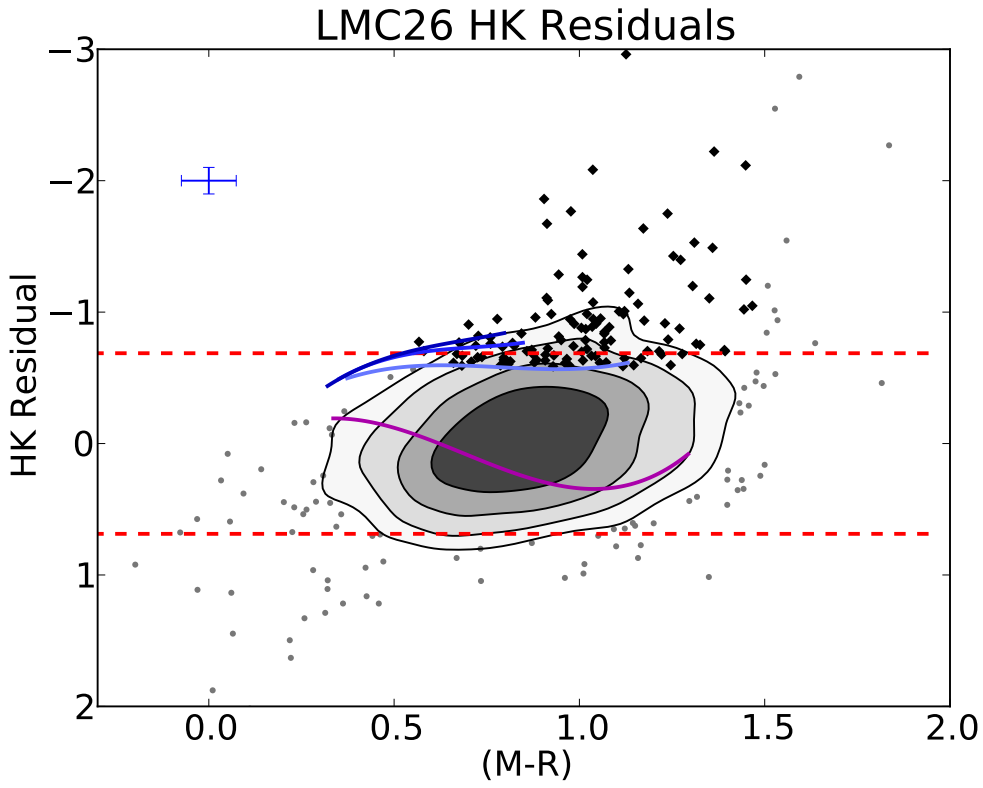

Figure 2.9: Residuals of HK diagram used to select metal-poor candidates, represented with black diamonds. Isochrones are as in Figure 2.8; blue isochrones are 13 Gyr, [Fe/H] $= -2.0, -3.0$, and -4.0, from lightest to darkest, respectively. The purple isochrone is a 4 Gyr, [Fe/H] $= -0.5$ isochrone. The dotted red lines represent the $\pm 2\sigma$ values of the HK values of all the stars in the plot. A typical error bar for the data is shown in the top-left.

The detection threshold was lowered for LMC20 to accommodate the lower number of stars in the field. For the outer fields, (fields with RA $< 4^h30^m$) both the I magnitude and the detection threshold were lowered significantly due to the very small number of targets in those fields. This will result in a higher number of

false positives, primarily foreground stars. These foreground stars are partially screened as detailed above using the DDO51 filter.

Due to issues with the data quality and the reduction pipeline, only certain fields were analysed. The science fields that were successfully reduced are LMC fields 8, 11, 13, 15, 20, 24, 25, and 26. Two of the clusters had usable data in some filters - 47 Tucanae and NGC4590. Three of the four observed metal-poor stars were also analysed: HE0107, HE0305, and HE0557.

2.3 Results

The most immediate test available to us is checking for consistency with the stars already observed in Cole et al. (2005). We see that there is good agreement between typical RGB stars and the Cole stars, with some stars having HK indices that could flag them as metal-poor under our selection criteria (Figure 2.10). There are some stars with comparatively high scatter in the CMD and HK diagram, which could indicate that there is some source of error in the photometry. These errors could be caused by incorrect matching of stars between each of the filters. Some level of mismatching is to be expected between filters due to the high degree of crowding in the inner fields. This problem should only affect a relatively small number of stars, which will diminish as we move further from the central fields. It is reassuring that the CMD and colour-colour plots show coherent, identifiable structures.

We also would like the metal-poor calibrators to be clearly identifiable in the HK diagrams, as they are all on the extreme end of the metallicity scale. From Figures 2.11, 2.12 and 2.13, we see that the metal-poor objects are all located well above the mean population constructed from stars in the ranges $0.1 < (R-I) < 0.8$ and

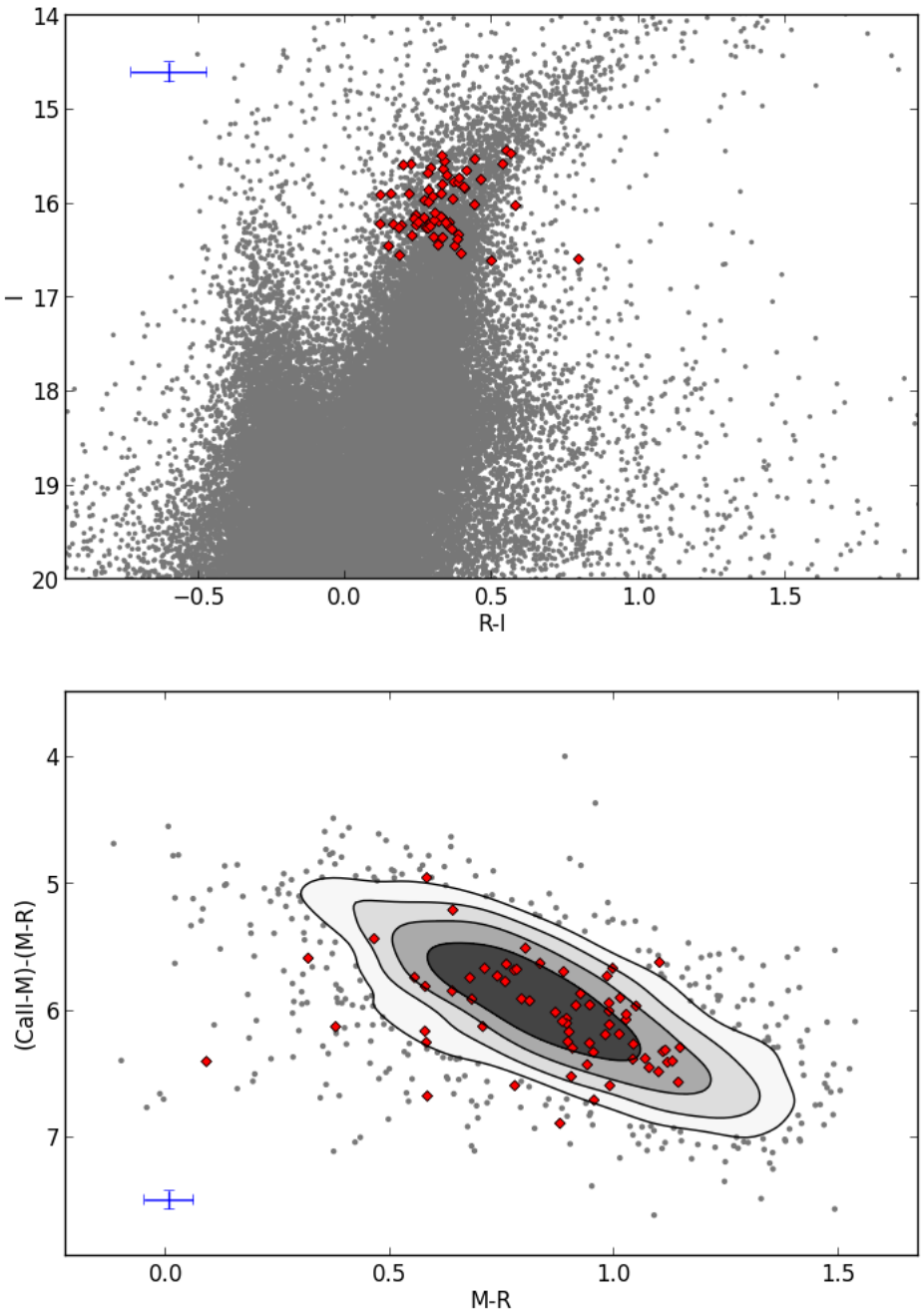

Figure 2.10: The location of the stars from Cole et al. (2005) (red diamonds) compared to other observed stars. The background data are from LMC field 26. Typical error bars for the data are given in the corners of the figures.

$10 < I < 18$. There is a higher degree of scattering in the field containing HE0305 but the metal-poor star still lies $\sim$ 0.5 dex from the mean of the population, about where we would expect metal-poor stars based off of the separation of the isochrones from Figure 2.1.

The morphology of our HK diagrams can also serve as an indicator of any issues that might be present in the data. For the inner fields[6], a large percentage of the data is RGB stars, with some minor contribution from MW foreground dwarf stars, and from MW asymptotic giant branch (AGB) stars. These foreground objects occupy the same area of the HK diagram as the RGB stars. The ratio of contaminants to genuine LMC stars increases dramatically as we move out from the central regions. To lessen the impact of these contaminants, they are filtered using the DDO51 Filter, as shown in Figure 2.5. A small number of obvious foreground objects can be removed using this method, an example of which is shown in Figure 2.14.

[6]LMC20 and inwards - those fields with RA $> 4^h30^m$.

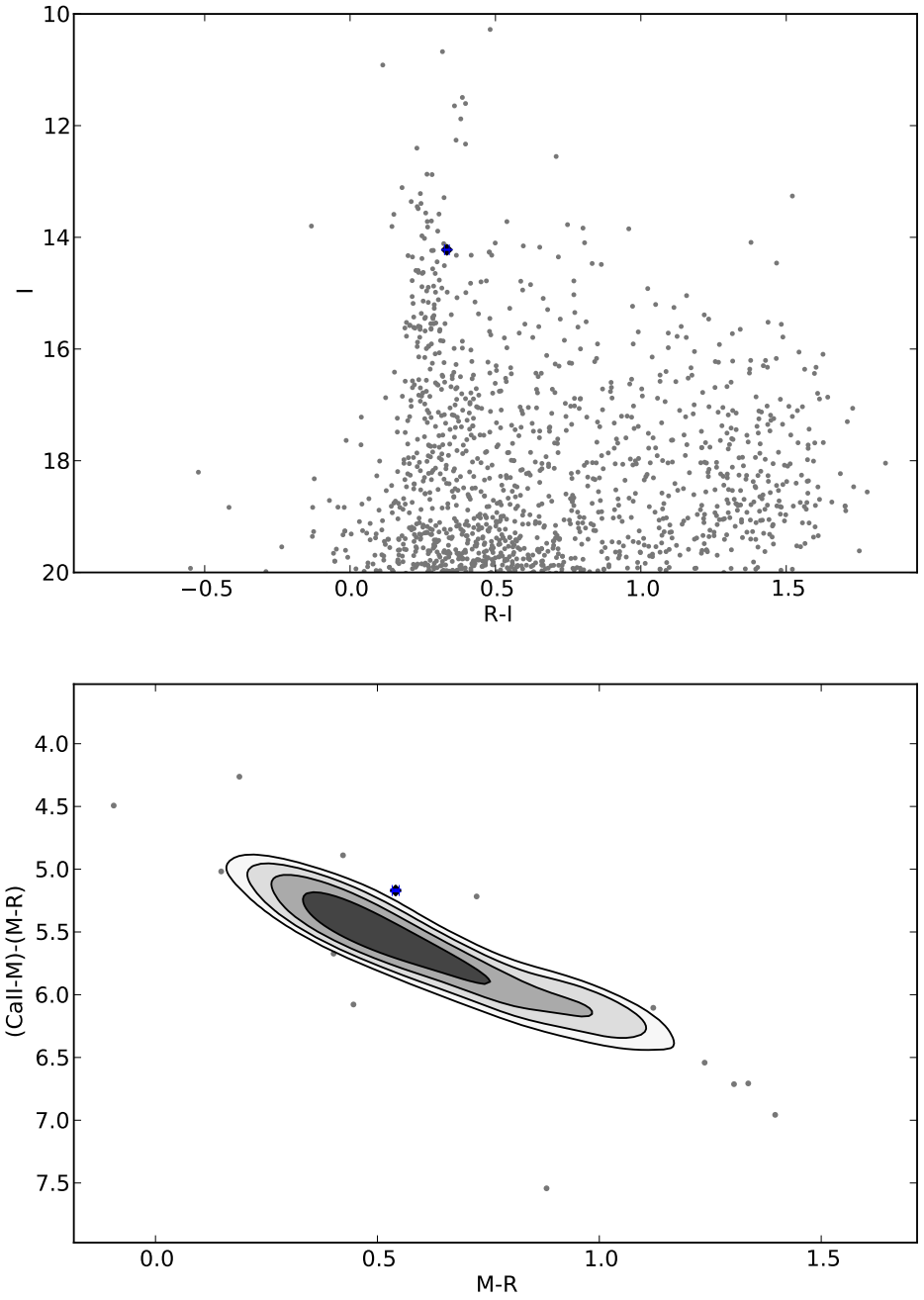

Figure 2.11: Location of HE0107 (black diamond) in the HK diagram and the CMD of the other stars in the same field. Error bars as indicated on the star. The HK diagram was constructed from stars with $0.1 < (R - I) < 0.8$ and $10 < I < 18$.

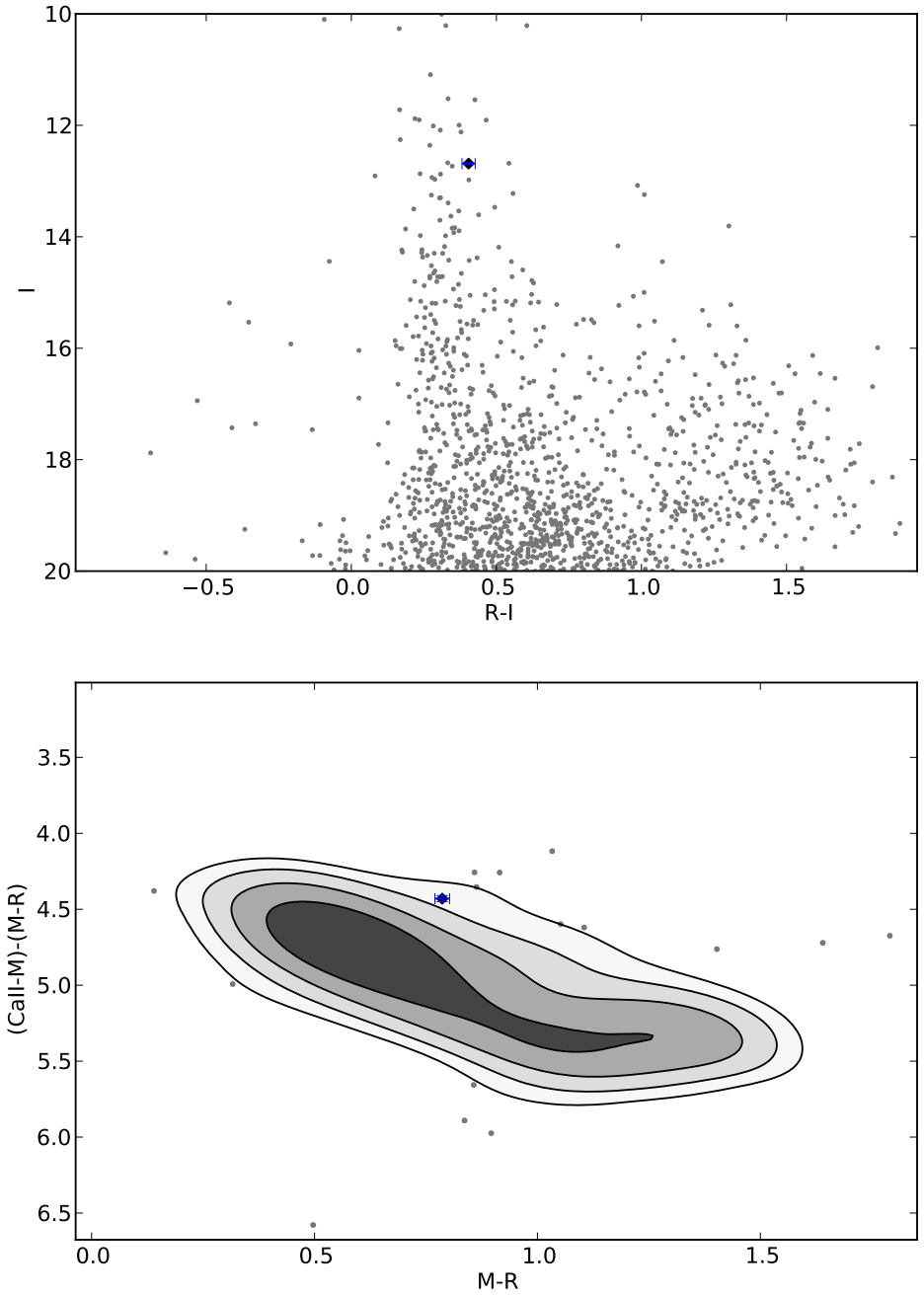

Figure 2.12: Location of HE0305 (black diamond) in the HK diagram and the CMD of the other stars in the same field. Error bars as indicated on the star. The HK diagram was constructed from stars with $0.1 < (R - I) < 0.8$ and $10 < I < 18$.

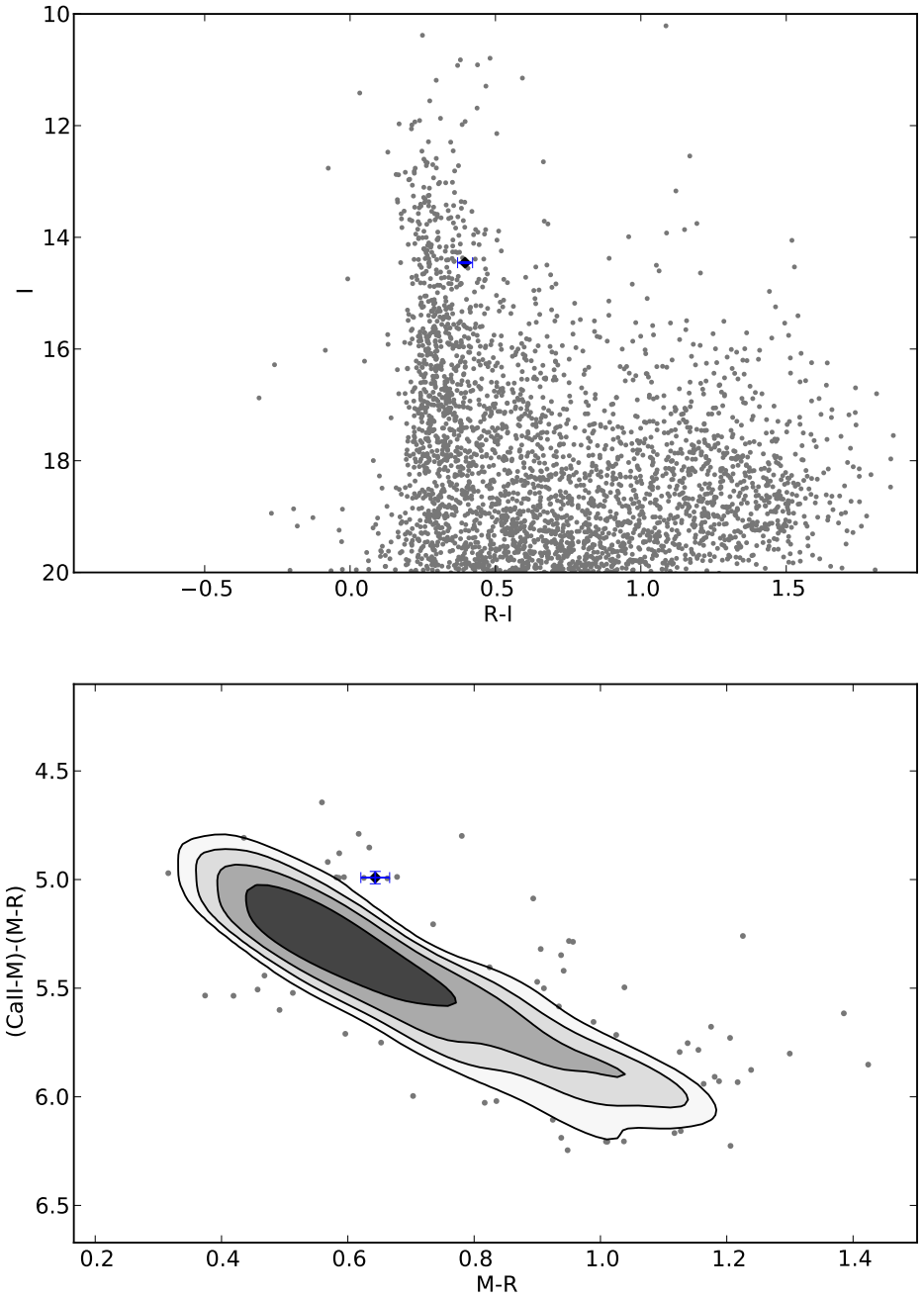

Figure 2.13: Location of HE0557 (black diamond) in the HK diagram and the CMD of the other stars in the same field. Error bars as indicated on the star. The HK diagram was constructed from stars with $0.1 < (R - I) < 0.8$ and $10 < I < 18$.

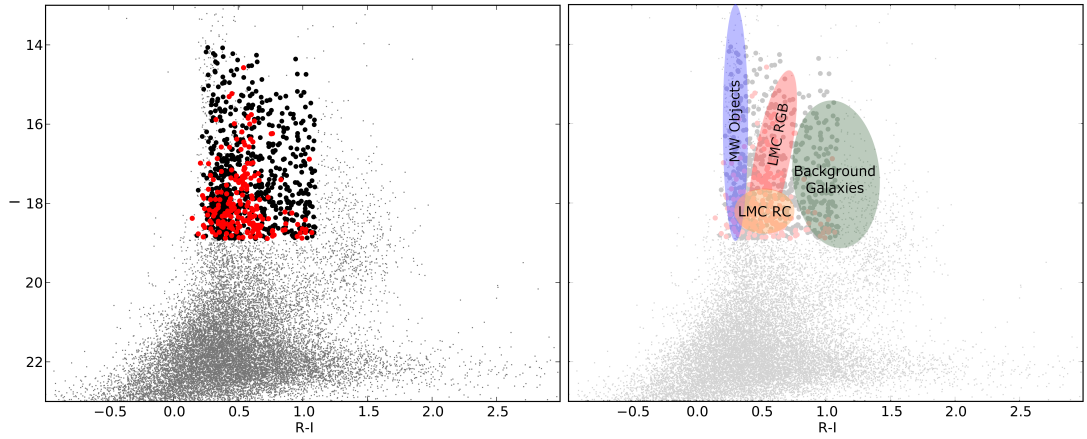

Figure 2.14: *Left*: A CMD of all available LMC13 data after filtering with DDO51, as shown in Figure 2.5. Black points are all objects considered to be non-foreground objects, and red points are the objects returned by our metal-poor selection criteria. The filtering was only performed on objects with $0 < (R-I) < 1.1$, and $14 < I < 18.9$. *Right*: The approximate locations of features in the filtered region. These feature regions only indicate where we might expect to find a majority of the labelled objects.

The inclusion of other objects is apparent in the outer fields' HK diagrams, in which a second feature below the RGB stars begins to dominate. These objects are most likely galaxies, having redder colours than the RGB stars. Ideally, these objects are filtered out in the reduction process using DAOPHOT, with the definition of the sharpness and roundness parameters allowing for rejection of very obvious galaxies. These galaxy contaminants are probably more distant (z $>$ 1.5) elliptical galaxies, whose PSF is similar enough to typical stars to pass the rejection criteria. There is also a minor spur feature in some of the diagrams, most notably in the field of 47 Tucanae (Figure 2.15). This feature could result from poor matches between filters in the photometric reduction step, caused by the high degree of crowding in the images.

The presence of these galaxies in the HK diagram is not an issue when it comes to

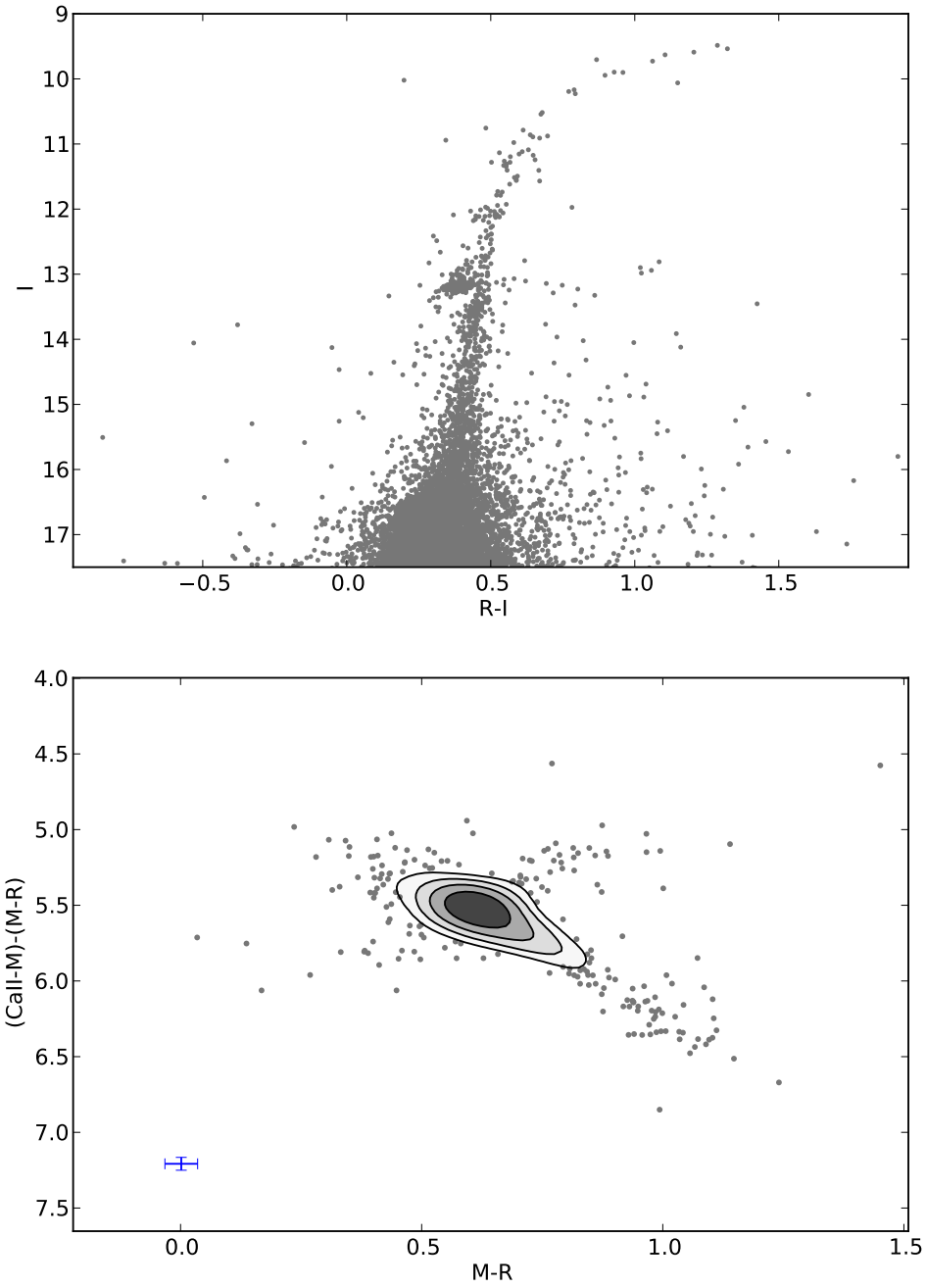

Figure 2.15: CMD and HK diagram for 47 Tucanae. Typical error bars for the data are given in the bottom left of the HK diagram. Apparent in this plot is a secondary feature that crosses the bulk of stars.

fitting our data, as the fit is still very good in the region we expect to find metal-poor stars (e.g. see Figures A.1 to A.4 in Appendix A). Due to the way in which we select the metal-poor candidates, the inclusion of these galaxies could increase the spread of HK index in the population, which we counteract by lowering the detection threshold slightly.

In the determination of metal-poor candidates, we need to consider the effect that reddening has on the HK index. From the reddening in the filters used to define the HK index, the reddening in HK is given by:

$$A_{HK} = 0.234 \times E(B - V)$$

Even if we expect at worst a variation of E(B - V) = 0.1 among stars in a field[7], the impact it will have on the HK index of the stars is < 0.05 dex. Paired with the effects of reddening on our temperature indicator, any stars with higher reddening than what we have estimated will appear to be slightly more metal-rich in the HK diagrams. These effects are much smaller than the errors from the photometry, which are likely the limiting factor for the sensitivity of our technique.

The following figures (2.16 to 2.23) show the locations of candidate objects in the HK diagram, and in the I vs (R-I) CMD for the fields we analysed. Looking at these diagrams, we can see that there is some zero-point issue between individual fields, as the location of the bulk of stars in HK space is not consistent. This could be a result of the crowding in the inner fields, as these are the fields in which the effect is the most noticeable. Comparatively, the outer fields have a much more consistent distribution of stars in HK space. As the candidates are calculated on a per-amplifier basis, this is not going to impact the identification of metal-poor stars.

In the fields with identifiable red giant branches, the candidates that are obviously

[7]From the extinction calculated from RR Lyrae stars in LMC (Haschke et al. 2011)

members of the RGB tend to lie on the blue side of the diagram. This is consistent with our understanding of metal-poor stars.

From Tumlinson (2010), the oldest and most metal-poor stars of a galaxy are most common on tightly-bound orbits in a galaxy's halo. We expect to find a majority of our metal-poor candidates in the inner fields of the LMC. In selecting candidates for follow-up, we preferentially select from these inner fields.

Table 2.2 contains a summary of our candidate numbers for each field. These objects were sorted based on their I magnitude to prepare for medium resolution follow-up spectroscopy prioritising the most easily observed targets.

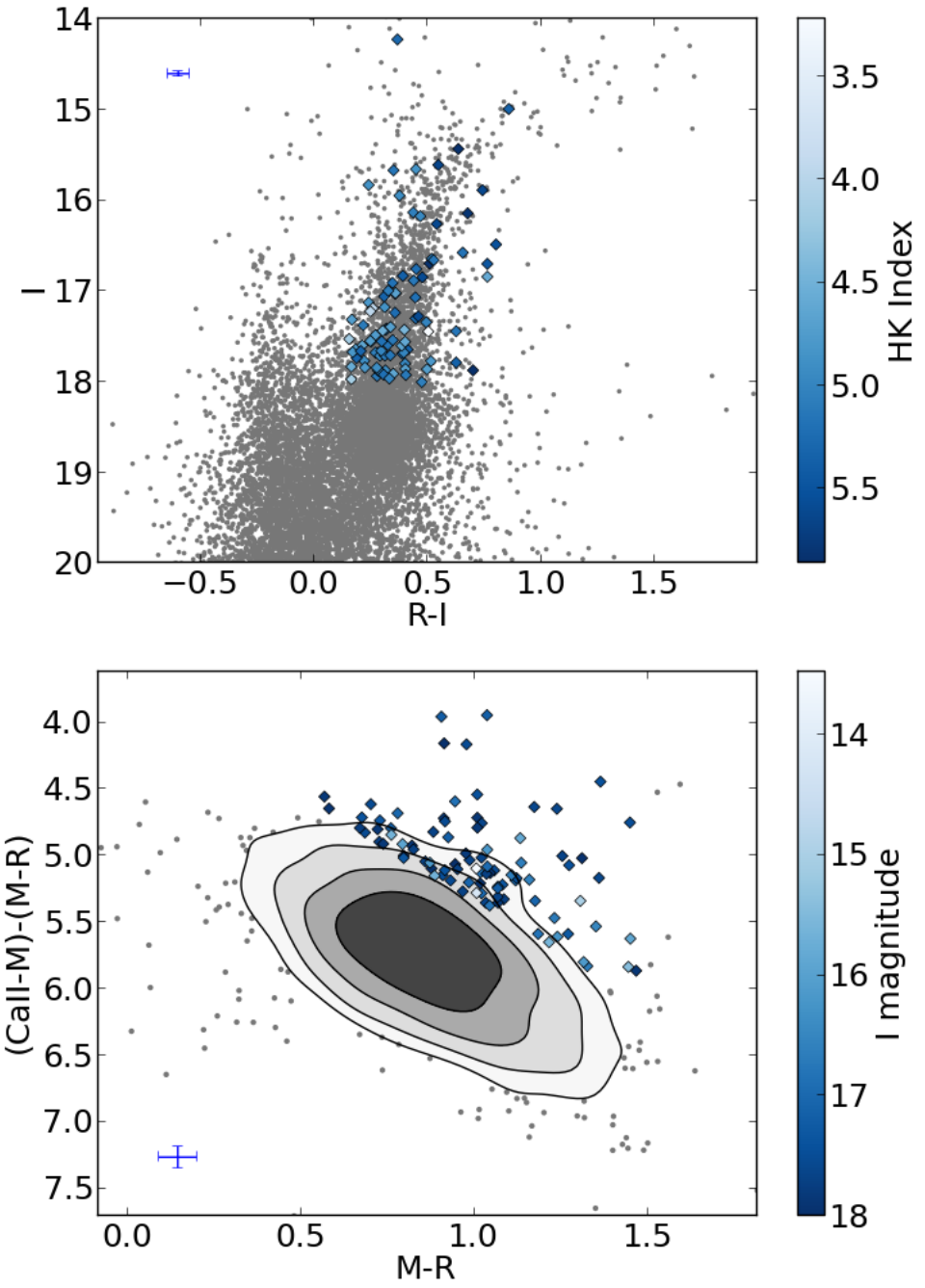

Figure 2.16: Example CMD and HK diagram for LMC26, showing the data from a single amplifier. Typical error bars of the identified metal-poor candidates (diamonds) are given in the figures.

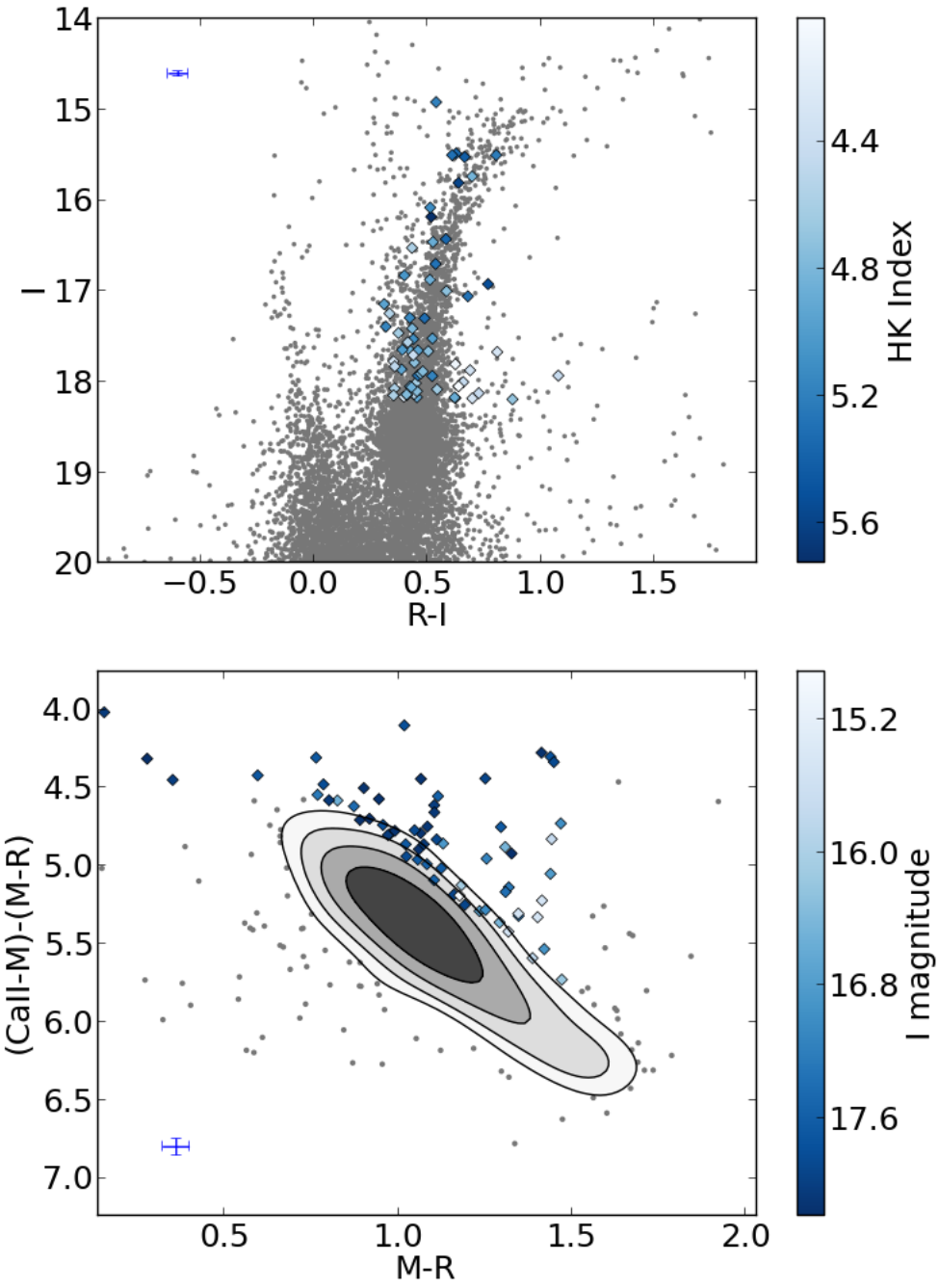

Figure 2.17: Example CMD and HK diagram for LMC field 25, showing the data from a single amplifier. Typical error bars of the identified metal-poor candidates (diamonds) are given in the figures.

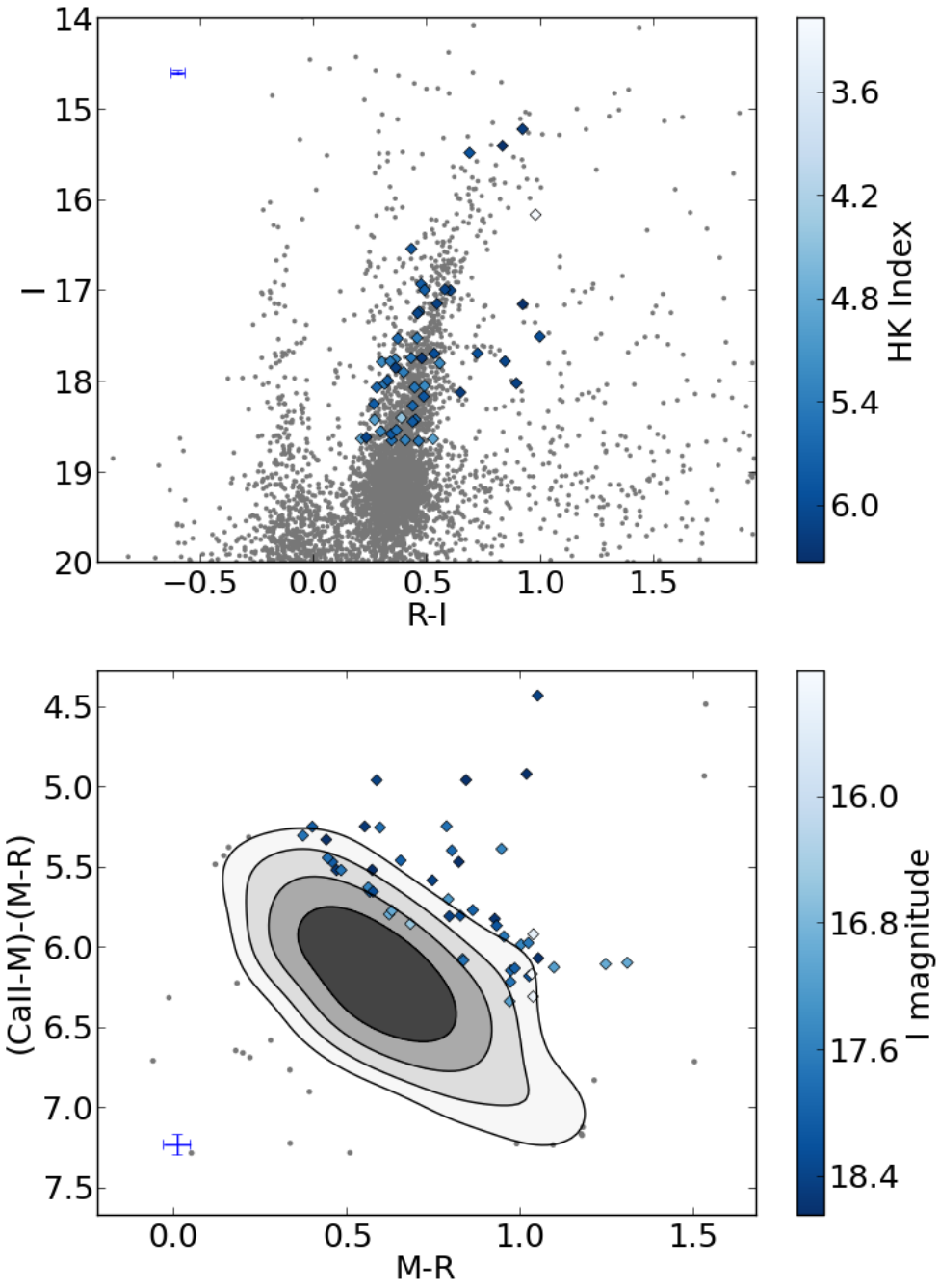

Figure 2.18: Example CMD and HK diagram for LMC field 24, showing the data from a single amplifier. Typical error bars of the identified metal-poor candidates (diamonds) are given in the figures.

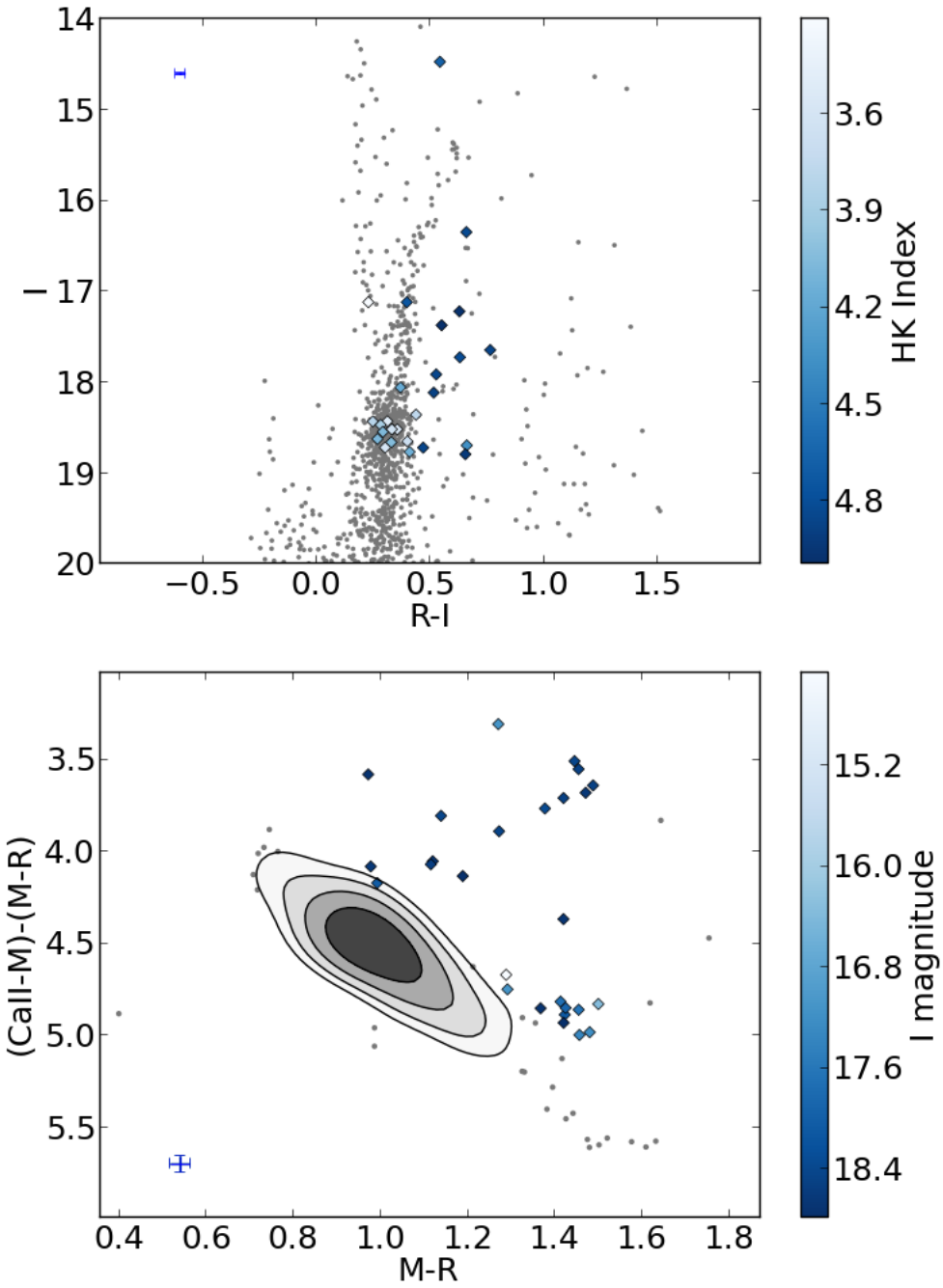

Figure 2.19: Example CMD and HK diagram for LMC field 20, showing the data from a single amplifier. Typical error bars of the identified metal-poor candidates (diamonds) are given in the figures.

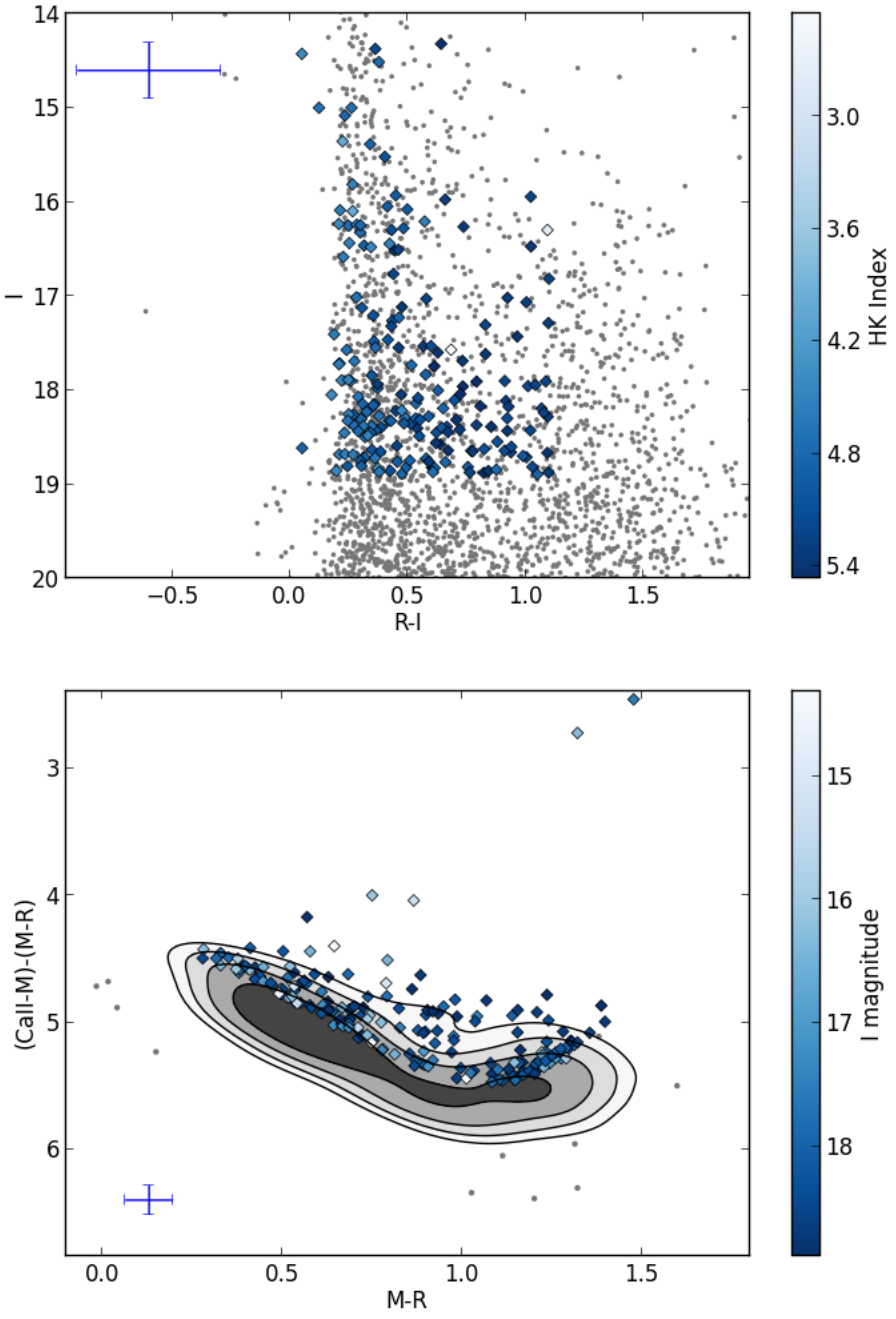

Figure 2.20: CMD and HK diagram for LMC field 15 for all amplifiers. Typical error bars of the identified metal-poor candidates (diamonds) are given in the figures.

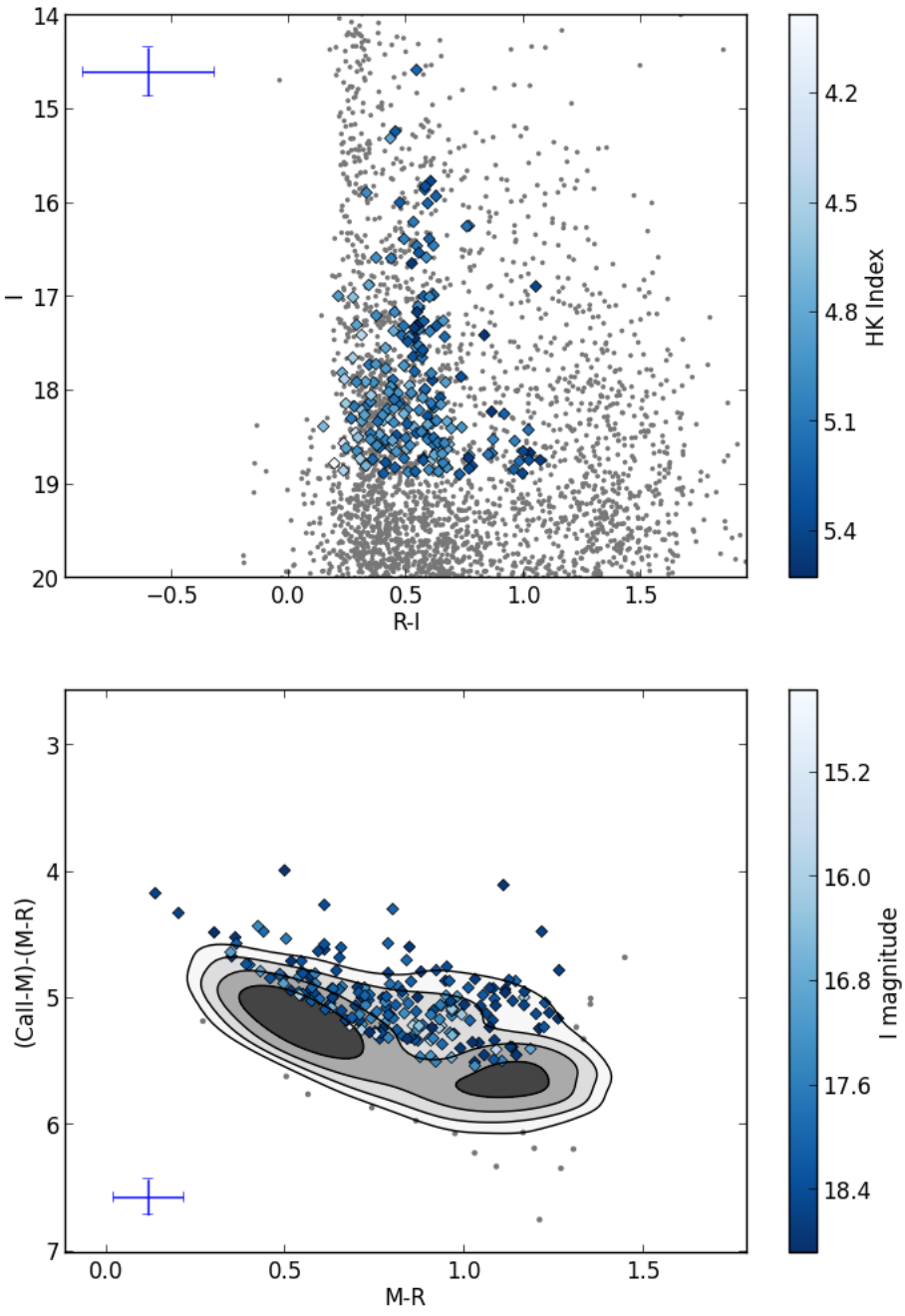

Figure 2.21: CMD and HK diagram for LMC field 13 for all amplifiers. Typical error bars of the identified metal-poor candidates (diamonds) are given in the figures

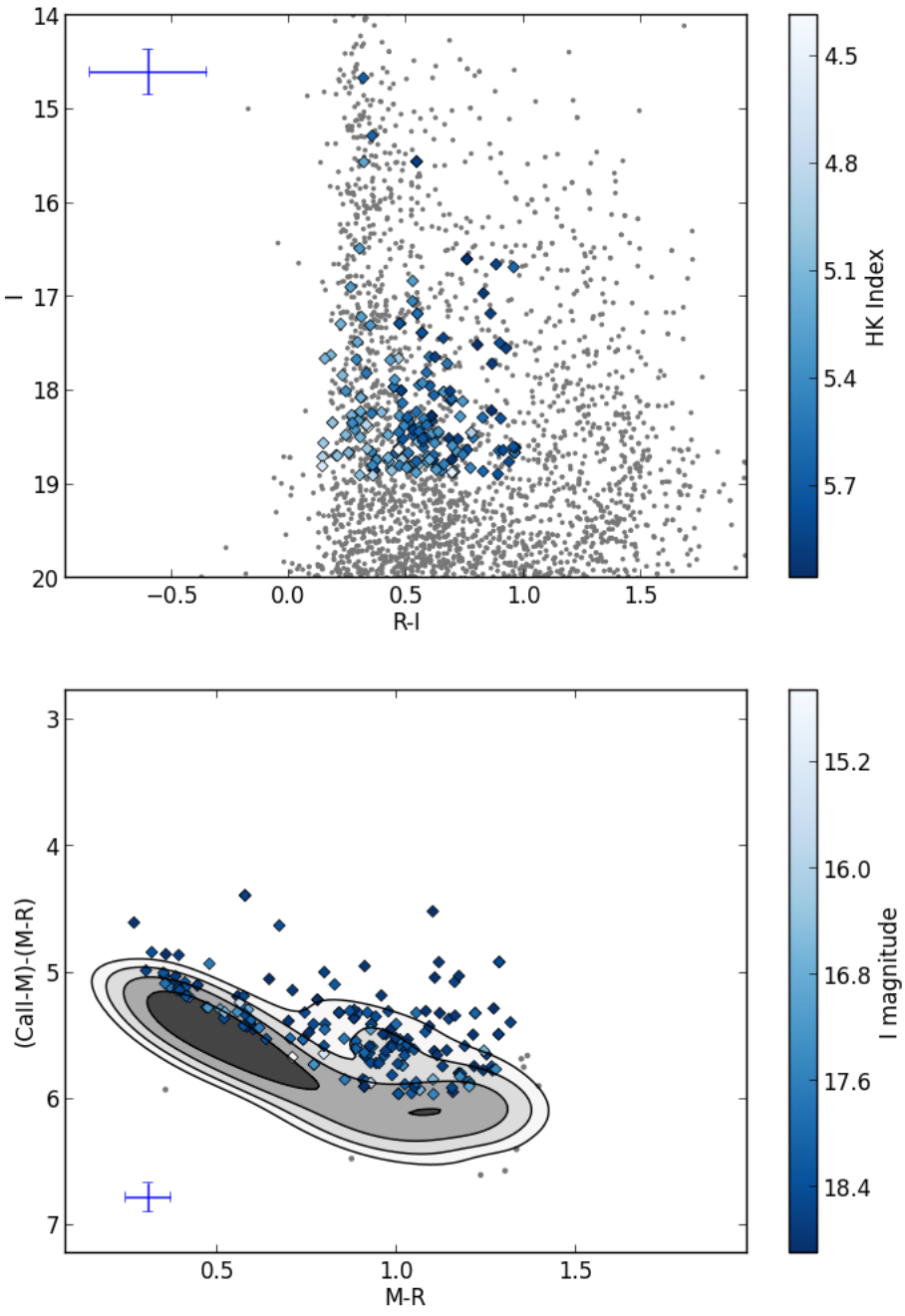

Figure 2.22: CMD and HK diagram for LMC field 11 for all amplifiers. Typical error bars of the identified metal-poor candidates (diamonds) are given in the figures.

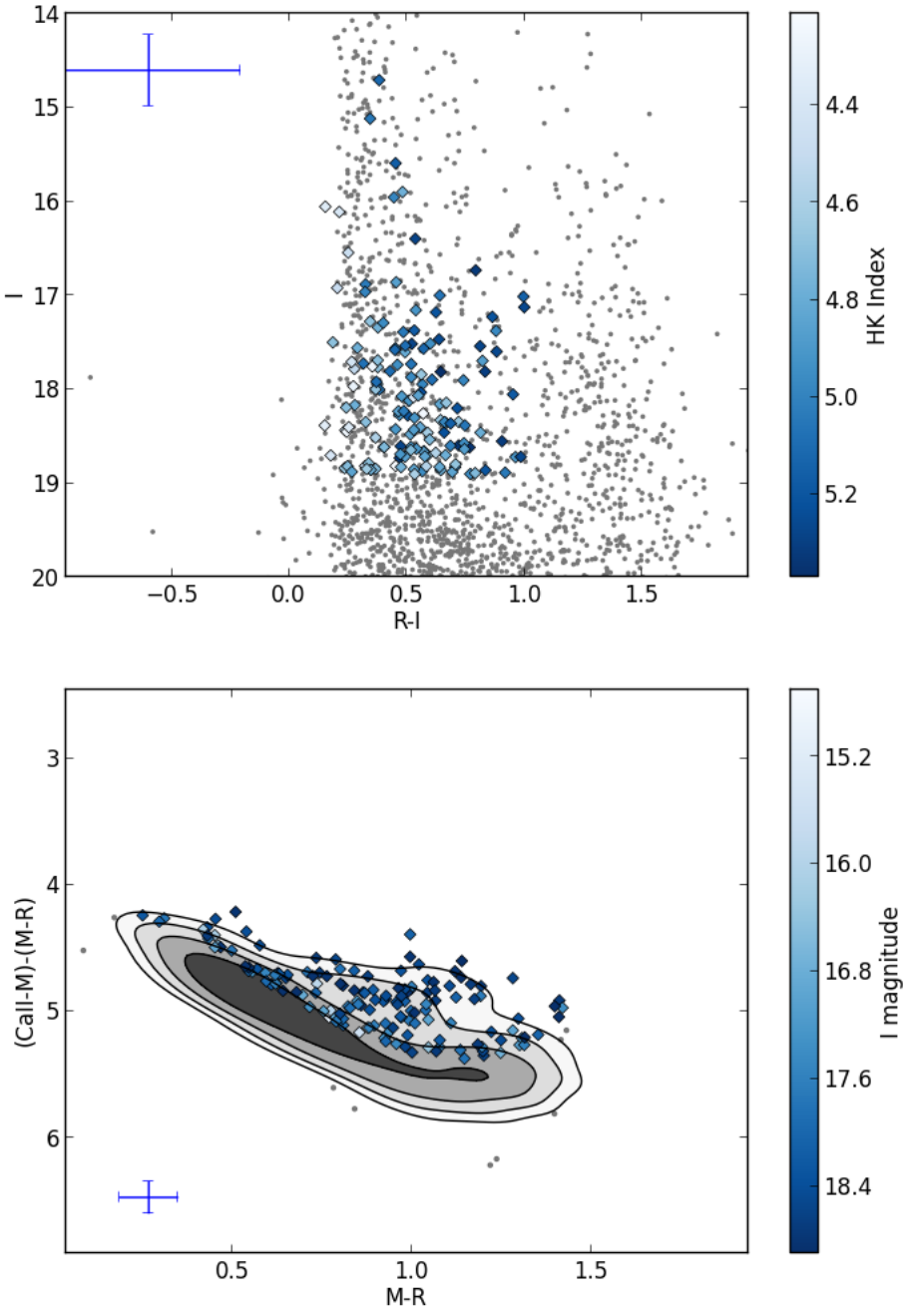

Figure 2.23: CMD and HK diagram for LMC field 8 for all amplifiers. Typical error bars of the identified metal-poor candidates (diamonds) are given in the figures.

Table 2.2: The number of candidate stars identified in fields

Field Name	Number of Candidates	Notes
LMC26	1182	[a]
LMC25	553	
LMC24	451	
LMC20	81	[b]
LMC15	156	[a,c,d,e]
LMC13	210	[a,c,d,e]
LMC11	102	[c,d,e]
LMC8	173	[a,c,d,e]

[a] Some amplifier data were not included in the selection of candidates due to issues in the reduction process.

[b] The selection criterion was lowered to $\sigma > 1.2$ due to a lower density of stars.

[c] The selection criterion was lowered to $\sigma > 0.7$ due to the extremely sparse RGB population and the inclusion of background galaxies.

[d] More strict filtering based on surface gravity was used to constrain candidates in these fields.

[e] The cutoff for I magnitude was lowered in the selection criteria.

The use of the HK index to select metal-poor candidate stars from a population has proven successful in other surveys such as PRISTINE (Starkenburg et al. 2017), SkyMapper (Schmidt et al. 2005; Keller et al. 2012), and originally in Anthony-Twarog & Twarog (1998). We have shown our HK index is capable of resolving metal-poor stars from the remainder of the fields using known EMP stars. Our choice of HK index is minimally influenced by reddening effects, which will be dwarfed by the photometric errors.

There is a range of complicating factors in considering the use of our HK diagrams. As our targets are very faint and crowded, a high degree of scatter in the central fields is to be expected. Contributions to the HK index from chromospherically active stars are also expected, something that cannot be easily distinguished solely with photometry. Finally, the effects of temperature on the index are not trivial; although we are applying our analysis to RGB stars, which have a relatively narrow range of temperatures, there is the possibility that strongly reddened spectral type A-F stars can creep into the sample based on their broadband colours, and these relatively weak HK-line stars could present many false positives.

Chapter 3

Spectroscopic Followup

In the previous chapter, we identified candidate metal-poor stars in each of our fields based on their HK index when compared to the rest of the stars in the field. Each candidate list was filtered to select feasible follow-up targets for observation at medium resolution, in order to confirm their metallicities. In this chapter, we will discuss these follow-up observations and the analyses performed on the collected data.

3.1 Observations

We were awarded three nights of observations on the nights of the 9th, 10th and 11th of December, 2017 at the Australian Astronomical Observatory (AAO). The observations were conducted using the AAOmega +2dF instruments, using two spectral gratings. Our blue spectra were taken with the 580V grating, which contains the Ca II H & K lines, the Mg triplet, and the Hβ line at a resolution of R $\sim$ 1500. The red spectra were observed using the 1700D grating, to cover the Ca II NIR triplet at a resolution of R $\sim$ 10000.

AAOmega + 2dF is capable of observing up to 392 stars simultaneously within its 2-degree field of view, with a fibre positional accuracy of 0.3 arcsec. The fibres for each field are configured using a priority system, with 8 of the 400 fibres reserved for fiducial stars. An additional minimum subset of fibres is reserved for dark sky, which is used by the reduction software to subtract the sky light from the image. The general fibre allocations used in our observations are given in Table 3.1.

Table 3.1: The object types observed with AAOmega + 2dF, with the assigned priorities used in the fibre configuration software. Included are the 2MASS J magnitudes of the objects.

Target Type	**Priority**	**2MASS J Magnitudes**
Fiducial Stars	9	$10.5 < 13.5$
Members of NGC1939	9	< 17.0
CTIO matched with 2MASS	8	< 17.0
Blank Sky	8	–
Cole et al. (2005) star	7	< 17.0
CTIO not matched with 2MASS	6	> 17.0
Spitzer-Selected Targets	2	$13 < 17$

For each field, approximately 15 fiducial stars were selected from the 2MASS catalogue with J magnitude between 10.5 and 13.5. For each fiducial star, proper motions were obtained from the SIMBAD database (Wenger et al. 2000). These stars constrain any rotation and translation of the field during observations, keeping the science targets on their assigned fibres. In each field, between 30 and 60 sky fibres were allocated by eye from examining DSS images of the regions, checked in 2MASS. Each observation assigned approximately 25 fibres to the blank sky for calibration.

The remaining fibres were assigned to science targets, attempting to minimise any fibre collisions, e.g. see Figure 3.1. We split our metal-poor candidates into two categories - stars that had a corresponding 2MASS catalogue object, and stars that did not. Because of the high degree of accuracy in positioning the fibres, we gave higher priority to the targets that had 2MASS coordinates, as we could not be certain the fainter objects without 2MASS coordinates would have starlight in the fibres.

As some fields did not have enough candidates to fill all the fibres, additional stars were selected from the Spitzer/SAGE and 2MASS catalogues. These stars also serve to populate the region around our relatively small CTIO fields within the AAOMega + 2dF field of view. These were given a low priority in the observations, so as to not compete for fibre allocation with the CTIO candidates.

These additional stars were inspired by the Schlaufman & Casey (2014) survey, albeit selected with less rigorous criteria. Stars that qualified for inclusion had $0.6 < \mathrm{J} - \mathrm{K} < 1.2$, and $12.0 < K < 14.0$ from 2MASS. Spitzer 3.6 micron and 4.5 micron IRAC magnitudes were used to further filter these stars for potentially metal-poor objects. As CO bands would cause [3.6] - [4.5] colours to be bluer, we opted for redder objects, selecting stars with colours $0.01 \leqslant [3.6] - [4.5] \leqslant 0.25$.

Across the nights, three test metal-poor objects were observed, listed in Table 3.2. These metal-poor objects span metallicities from [Fe/H] = -3.0 down to [Fe/H] = -4.0. Observing these stars allows us to check various methods of accurately identifying metallicity.

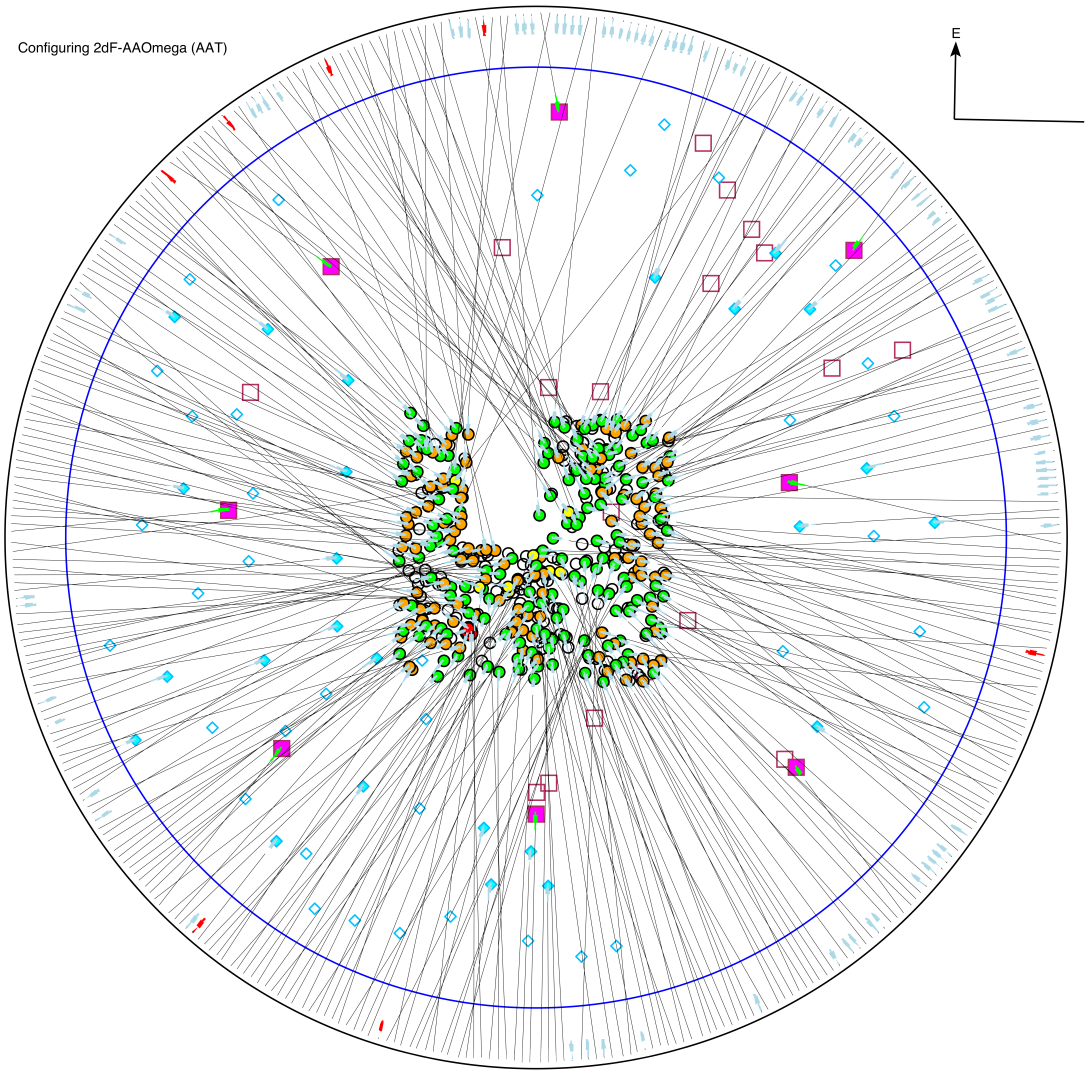

Figure 3.1: Example fibre allocation for LMC field 26 with 2dF + AAOmega. Magenta squares are fiducial (guide) stars, cyan diamonds are blank sky regions, red circles are members of NGC1939, orange circles are stars with associated 2MASS objects, yellow circles are Cole et al. (2005) stars, and green circles are stars without an associated 2MASS object. Unfilled objects have not been assigned a fibre.

Table 3.2: The three metal-poor objects that we observed during our AAO run.

Target	**[Fe/H]**	$\mathbf{V}_{HEL}$	$\mathbf{T}_{Eff}$	**log g**	**Nights Observed**
CS 31072-118	-2.94[a]	145.8[b]	4606[b]	1.25[b]	Nights 2 & 3
HE 0305-5442	-3.56[c]	158.3[d]	4850[c]	1.70[c]	Night 3
HE 0044-3755	-4.0[e]	46.4[f]	4650[e]	0.95[e]	Night 3

[a] Christlieb et al. (2004b)

[b] Barklem et al. (2005)

[c] Hansen et al. (2013)

[d] Cohen et al. (2013)

[e] Hollek et al. (2011)

[f] Gontcharov (2006)

The observations of the science fields all consisted of 3 × 20-minute exposures, with the exception of the observations of LMC fields 25 and 26 on the second night, which were 3 × 30-minute exposures. The increase in exposure time was because these second observations contained the fainter candidates from the CTIO data. Repeat observations of fields 25 and 26 also were configured with the high priority targets that were not assigned fibres in the previous observations. Seeing varied between 1.2" and 2.0" on each night, with the average seeing being $\sim$ 1.6".

3.2 Data Analysis

At the beginning of each night, a set of bias images were taken for the calibration of the images. Also required for calibration are a set of arc lamp exposures, for wavelength calibration, and flat exposures, to correct for the response along the CCD. Every science observation has a set of corresponding arc lamp and flat

exposures, taken before the science exposures.

The flat exposures were performed using a 75W lamp, with an exposure time of 25 seconds for the blue CCD and 40 seconds for the red CCD. To calibrate the wavelength in the two CCDs, a He+CuAr+FeAr+CuNe lamp was used, with 45 and 75 second exposures for the blue and red CCDs, respectively.

The AAO data were reduced using the 2dFdr reduction software. The 2dFdr software streamlines the data reduction process, which we will outline briefly. First, all bias frames from a single night are combined, rejecting any cosmic rays in the images. The combined bias frame is subtracted from each of the subsequent frames in the reduction process.

2dFdr has a list of expected lines from each element present in the arc lamps and attempts to match up the positions of the emission lines on the CCD. Any poorly fit lines are not used in the wavelength solution. Again, any cosmic rays detected are rejected from the images.

The flat frames are used to model the response of the CCD across the image using a 4th order polynomial for each fibre. Any missing fibres from the image have a response interpolated from the nearby fibres. The science images are then divided by these flats, to normalise the response.

Each of the three exposures per science field is reduced individually, with some additional calibrations. The wavelength solution calculated with the arc lamps is adjusted based on any strong sky lines in the image. This is only performed on the red images, as there are only two strong sky lines in the blue wavelengths. Once the calibrations on each image are complete, the three exposures are combined, adjusting the continuum levels to be consistent between exposures.

During the observations, we observed a number of stars that were observed in Cole

et al. (2005), to use as metallicity and velocity standards for our observations. The spectra of these stars were extracted from their respective fits images to perform velocity calibration. The fits header information was edited to include the velocities of the calibration stars, to perform Fourier cross-correlation on the data.

The velocities of each star were determined using the IRAF `fxcor` package. We used 20 of the Cole et al. (2005) stars as velocity standards with the red images to determine the velocity of each object. The cross-correlation was also performed on the velocity standards, to compare the derived velocities to the literature values (shown in Table 3.4). With the resolution of the red images and the number of reference spectra used, we are able to get the velocities accurate to within ± 5 km s^{-1}.

We then measured the equivalent widths of the stars using IRAF routines. The spectra were first normalised using `continuum` before measuring the equivalent widths using `fitprofs`. These tasks were performed in batches on individual apertures of the fits images, which were binned based on their velocity. The velocity bins were selected with comfortable margins for the LMC, including stars in the range 150 km s^{-1} to 420 km s^{-1}, with a bin size of 30 km s^{-1}. A majority of stars were binned in the range 220 km s^{-1} to 300 km s^{-1} (see e.g. Figure 3.2).

Each spectrum was checked by hand after processing through the automated IRAF equivalent width measurements, which missed a handful of spectra. The equivalent widths of the Ca II triplet lines were measured by hand using `splot` and the interactive plot window.

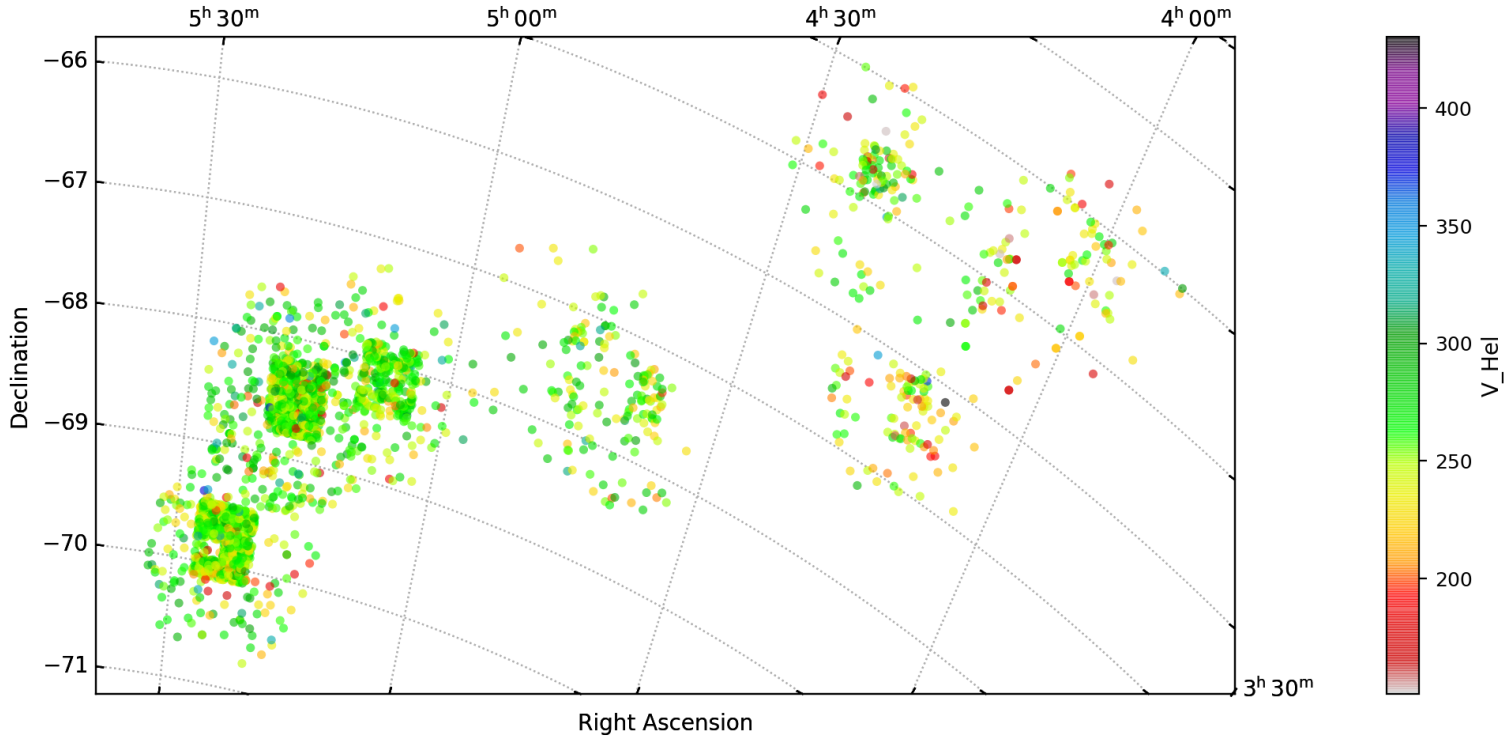

Figure 3.2: Velocity of measured stars in the LMC by position

3.3 Results

To calculate the metallicity of our stars, we use the relation between the equivalent widths of the two strongest lines of the calcium triplet (λ = 8542Å and λ = 8662Å), with the magnitude of the star, as described in Starkenburg et al. (2010):

$$[Fe/H] = -2.87 + 0.195 \times (V - V_{HB}) + 0.458 \times EW_{(2+3)} - 0.913 \times EW_{(2+3)}^{-1.5} + 0.0155 \times EW_{(2+3)} \times (V - V_{HB}) \quad (3.1)$$

We cross-matched our stars with results from the LMC photometric survey (Zaritsky et al. 2004) for the $(V - V_{HB})$ value required in equation 3.1. We use a value of $V_{\rm HB} \sim 19.3$ for all of our calculations, based off of the RR-Lyrae population reported by Clementini et al. (2003). For stars that were not observed in the LMC photometric survey, we convert our CTIO photometric I magnitudes to absolute magnitudes[1], and use the following equation from Starkenburg et al. (2010):

$$[Fe/H] = -2.78 + 0.193 \times M_I + 0.442 \times EW_{(2+3)} - 0.834 \times EW_{(2+3)}^{-1.5} + 0.0017 \times EW_{(2+3)} \times M_I \quad (3.2)$$

For stars for which we were unable to obtain V magnitude or I magnitude, we instead used the following empirical relation (Cole, unpublished):

$$[Fe/H] = -3.287(\pm 0.038) + 0.374 \sum EW_{Ca\,II} + 0.143(\pm 0.009)(J - J_{tRGB}) \quad (3.3)$$

Where J_{tRGB} is the 2MASS J magnitude of the tip of the RGB, and $\sum EW_{Ca\,II}$ is the sum of the equivalent widths of all three lines in the Ca II triplet.

The positions of all stars with velocities between 150 km s^{-1} and 420 km s^{-1} are shown in Figure 3.2. The velocity of stars within the LMC appears slightly higher

[1]Assuming a distance of 50 kpc, and a reddening of E(B - V) = 0.06.

in the central fields that we observed, with a majority of stars having $v > 250$ km s^{-1}, compared to the outer fields, with a greater proportion of stars having velocities $v < 250$ km s^{-1}, In accordance with the rotation curve of the LMC disk.

3.3.1 Metal-Poor Calibrator Stars

As the metallicity decreases (at fixed T_{eff} and log g) we should see a decrease in the widths of the Ca II triplet. The Ca II triplet also has strong surface gravity sensitivity, and some temperature dependence across late G and K giant stars. The widths of the Ca II triplet will decrease as log g increases, and as temperature increases (Jorgensen et al. 1992). We see the effects of decreasing metallicity in the spectra of our metal-poor calibration stars, CS31072-118, HE 0305-5442, and HE0044-3755, shown in Figure 3.3. These stars vary in T_{Eff} by ~ 200 K, and in log g by ~ 0.8. In this figure, we have included a comparatively metal-rich star, in which we can see many of the other metal lines that should be subtle at lower metallicities.

The Fe I line at λ8688 is a noteworthy feature that visibly diminishes as the metallicity decreases. As it is not very strong compared to the Ca II triplet, with $EW(\lambda8688)/EW(\lambda8542) \sim 0.1$ (Ginestet et al. 1994), it is hard to use as an indicator of metallicity at the typical signal-to-noise of our spectra.

The equivalent widths of the λ8542 and λ8662 lines for the three stars are given in Table 3.3.

Table 3.3: The equivalent widths of our metal-poor calibrator stars as measured in IRAF.

Star	**EW** λ8498	**EW** λ8542	**EW** λ8662
CS 31072-118	1.11 ± 0.09	1.82 ± 0.45	1.50 ± 0.15
HE 0305-5442	0.30 ± 0.07	0.66 ± 0.13	0.62 ± 0.18
HE 0044-3755	0.32 ± 0.11	0.47 ± 0.12	0.51 ± 0.08

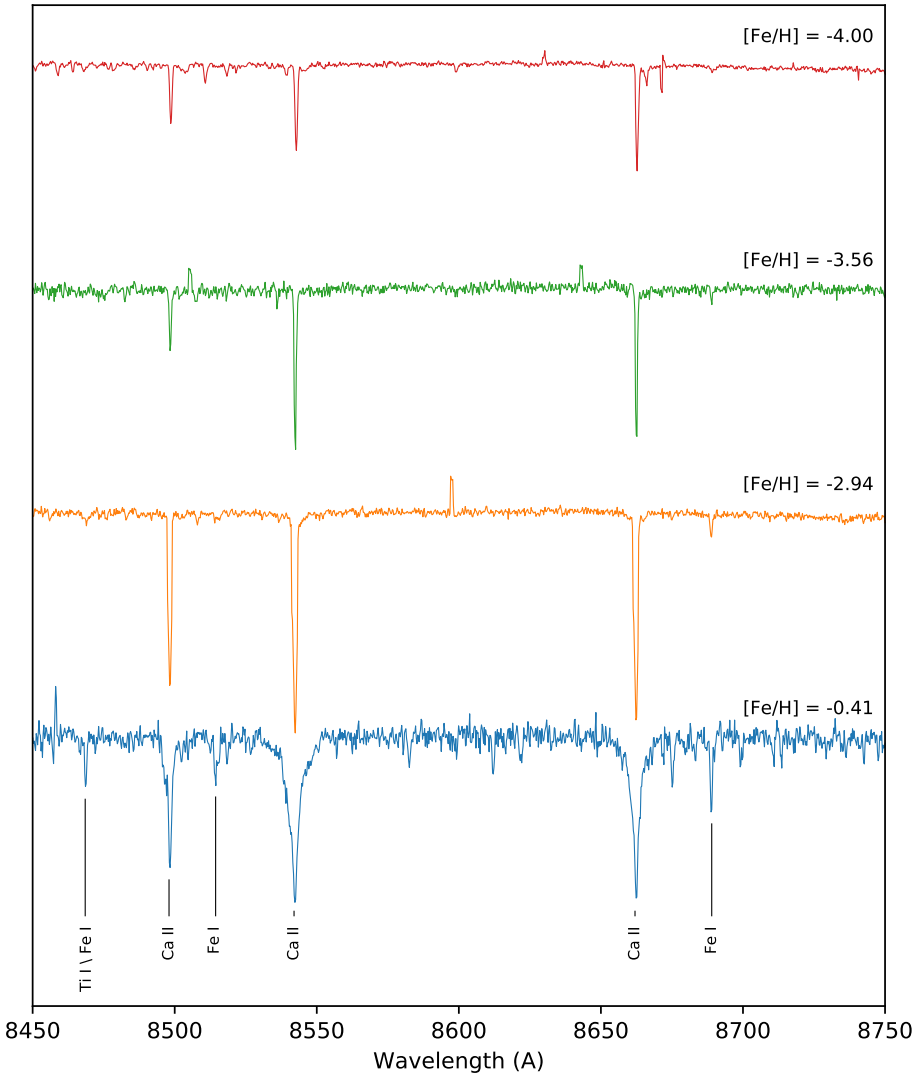

Figure 3.3: Normalised spectra for the metal-poor stars HE 0044-3755, HE 0305-5442, CS 31072-118, and a Cole et al. (2005) star 2MASS 05232680-6953109, from top to bottom, respectively. The stronger lines apparent in the stars are labelled

3.3.2 Cole et al. 2005 Stars

Across the three nights, we observed a total of 22 stars from the Cole et al. (2005) study. We performed a Fourier cross-correlation on these stars, as a test of our ability to measure the radial velocities accurately. Two of these velocity standard calibrators were not included in the Fourier cross-correlation because of consistent calculated velocity offsets when compared to the other stars. This could be due to the fibres being assigned to a star that is different to the ones measured in the 2005 study, which used a slit spectrograph. The stars not included in velocity calibration are 2M05240613-6953529 and 2M05223316-6951389. The velocity discrepancies can be seen in Table 3.4.

The results of the cross-correlation are shown in Figure 3.4 and in Table 3.4. The majority of stars have a relatively close velocity to those previously reported, with only four stars having a velocity difference of more than 10 km s^{-1}. The mean velocity offset was $v = -0.7$ km s^{-1}, with $v_{rms} = 7.6$ km s^{-1}.

In Figure 3.5 and Table 3.5, we show the metallicities calculated using equations 3.1 and 3.2. There are three stars that were calculated to have larger metallicities than previously measured. In these stars, we have derived metallicities up to ~ 1 dex higher compared to the Cole et al. (2005) metallicities. Of these three outliers, two are stars that we previously noted as problematic in the velocity calibration step. Of the two problematic stars, 2M05223316-6951389 was the reddest metal-poor star in the 2005 study, which could indicate that some form of stellar activity was partially filling the Ca II lines, making the star appear more metal-poor in 2005.

To ensure that the errors are not caused by our methodology, we calculated the metallicities of the stars from Cole et al. (2005) using the equivalent widths measured during their study (Cole, private communication). We found that the re-

sulting metallicities agreed within 0.05 dex, with a mean offset of less than [Fe/H] = +0.02 dex. When our metallicities are compared to the metallicities in Van der Swaelmen et al. (2013), we find that only one of our discrepant metallicities is justified. Star 2M05232680-6953109 has a reported metallicity of [Fe/H] = -0.58 ± 0.03, with the remaining stars having a metallicity similar to that reported in Cole et al. (2005). There was one additional star that was flagged as an outlier from the automatic line width detection process, with [Fe/H] = −0.79, δ[Fe/H] = +0.62. This star (2M05230370-6944219) was measured again manually, from which we derived a revised metallicity of [Fe/H] = −1.24. This places it much closer to the value reported in the 2005 study. Figure 3.5 and Table 3.5 reflect the correctly measured values.

When including the outliers, our metallicities have a mean offset of [Fe/H] = +0.2, with $[\mathrm{Fe/H}]_{rms} = 0.38$. If we exclude these four outliers, the mean offset in metallicity is [Fe/H] = +0.07 with $[\mathrm{Fe/H}]_{rms} = 0.15$.

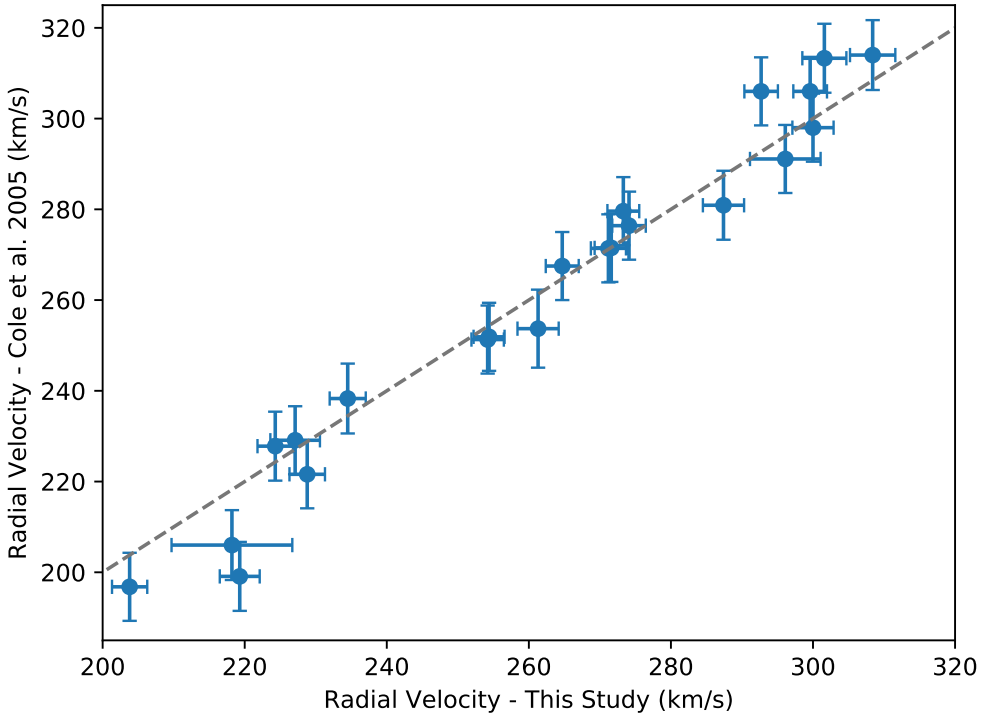

Figure 3.4: Velocities from Cole et al. (2005) of stars observed in this study compared to the velocities determined with Fourier cross-correlation from our spectra. The dashed line represents a 1-to-1 relation.

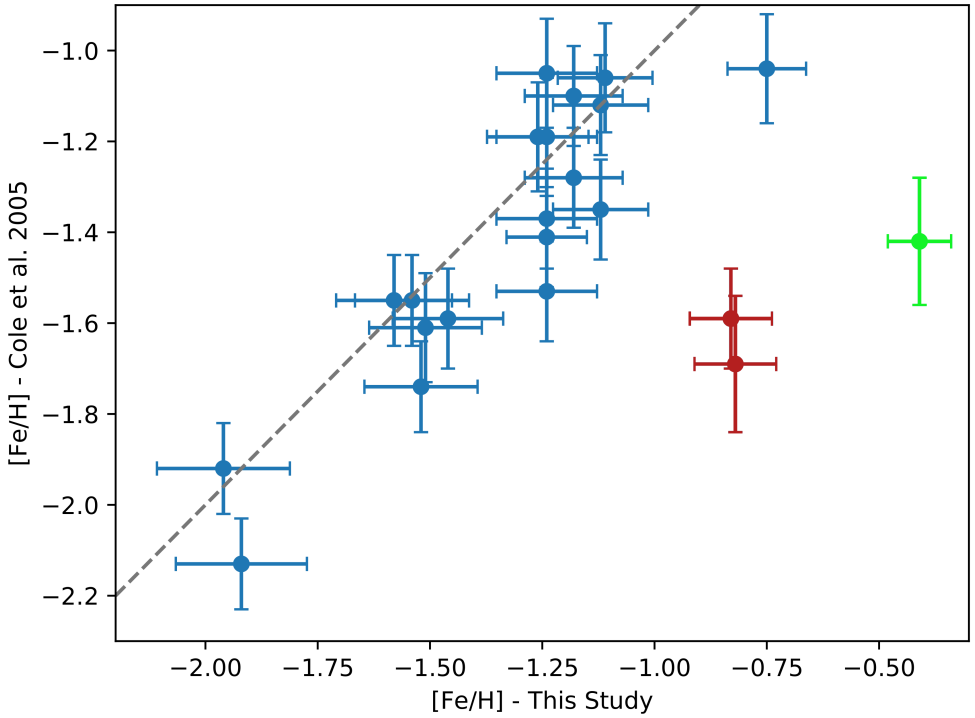

Figure 3.5: [Fe/H] from Cole et al. (2005) of stars observed in this study compared to the [Fe/H] determined using the (V-V_{HB}) from Cole et al. (2005). The dashed line represents a 1-to-1 relation. The two red points represent the two stars that were excluded in the velocity calibration due to consistent velocity offsets. The green point represents a star with a reported metallicity of [Fe/H] = -0.58 ± 0.03 (Van der Swaelmen et al. 2013).

Table 3.4: The stars from Cole et al. (2005) that were observed with AAOmega + 2dfdr. Given here are the velocities calculated for each of the stars based on their spectra. Also listed are the velocity values from Cole et al. (2005).

Star ID (2MASS)	$\mathbf{V}_{HEL}$ km s^{-1}	$\mathbf{V}_{HEL-Cole}$ km s^{-1}	δ km s^{-1}
$05240613-6953529$	218.2 ± 8.5	206.0 ± 7.7	$+12.2$
$05242202-6945073$	301.6 ± 3.1	313.3 ± 7.6	-11.7
$05244408-6942423$	300.0 ± 2.9	298.0 ± 7.5	$+2.0$
$05232680-6953109$	261.3 ± 2.9	253.7 ± 8.6	$+7.6$
$05225632-6942269$	287.4 ± 2.9	280.9 ± 7.6	$+6.5$
$05223557-6943373$	224.3 ± 2.5	227.8 ± 7.6	-3.5
$05223416-6944433$	228.8 ± 2.5	221.6 ± 7.5	$+7.2$
$05243669-6943358$	292.7 ± 2.4	306.0 ± 7.5	-13.3
$05230203-6935557$	254.4 ± 2.2	251.9 ± 7.5	$+2.5$
$05231074-6939184$	203.8 ± 2.5	196.8 ± 7.5	$+7.0$
$05253235-6943137$	271.2 ± 2.5	271.4 ± 7.5	-0.2
$05244301-6943412$	296.1 ± 5.0	291.1 ± 7.5	$+5.0$
$05223878-6955441$	299.6 ± 2.4	306.0 ± 7.6	-6.4
$05233236-6948257$	227.1 ± 3.5	229.1 ± 7.5	-2.0
$05223758-6949576$	254.2 ± 2.3	251.3 ± 7.5	$+2.9$
$05224088-6951471$	264.7 ± 2.3	267.5 ± 7.5	-2.8
$05230647-6944394$	234.5 ± 2.5	238.3 ± 7.7	-3.8
$05230776-6946082$	273.3 ± 2.2	279.6 ± 7.5	-6.3
$05252958-6959234$	308.4 ± 3.2	314.0 ± 7.7	-5.6
$05223316-6951389$	219.3 ± 2.8	199.1 ± 7.6	$+20.2$
$05255102-6937103$	271.6 ± 2.3	271.5 ± 7.5	$+0.1$
$05230370-6944219$	274.1 ± 2.4	276.4 ± 7.5	-2.3

Table 3.5: The stars from Cole et al. (2005) that were observed with AAOmega + 2dfdr. Given here are the equivalent widths and the metallicities calculated for each of the stars based on equation 3.1. Also listed are the $\sum$EW values from Cole et al. (2005) and the metallicities derived therein.

Star ID (2MASS)	**EW**$_{8542+8662}$ Å	**[Fe/H]**	**EW**$_{Cole}$ Å	**[Fe/H]**$_{\rm Cole}$
$05240613-6953529$	5.76	-0.83	5.04 ± 0.13	-1.59 ± 0.11
$05242202-6945073$	3.45	-1.92	3.58 ± 0.12	-2.13 ± 0.10
$05244408-6942423$	5.16	-1.26	6.58 ± 0.14	-1.19 ± 0.12
$05232680-6953109$	6.84	-0.41	5.71 ± 0.22	-1.42 ± 0.14
$05225632-6942269$	5.11	-1.24	6.41 ± 0.20	-1.19 ± 0.13
$05223557-6943373$	5.03	-1.18	5.93 ± 0.09	-1.28 ± 0.11
$05223416-6944433$	5.01	-1.24	6.63 ± 0.11	-1.05 ± 0.12
$05243669-6943358$	5.09	-1.24	5.41 ± 0.15	-1.53 ± 0.11
$05230203-6935557$	5.24	-1.12	6.55 ± 0.08	-1.12 ± 0.11
$05231074-6939184$	5.36	-1.12	6.11 ± 0.07	-1.35 ± 0.11
$05253235-6943137$	4.39	-1.51	5.14 ± 0.21	-1.61 ± 0.12
$05244301-6943412$	4.58	-1.54	5.69 ± 0.08	-1.55 ± 0.10
$05223878-6955441$	4.39	-1.52	4.79 ± 0.09	-1.74 ± 0.10
$05233236-6948257$	5.76	-0.75	6.47 ± 0.12	-1.04 ± 0.12
$05223758-6949576$	5.51	-1.11	6.93 ± 0.08	-1.06 ± 0.12
$05224088-6951471$	3.46	-1.96	4.43 ± 0.09	-1.92 ± 0.10
$05230647-6944394$	4.32	-1.58	5.34 ± 0.05	-1.55 ± 0.10
$05230776-6946082$	5.31	-1.18	6.74 ± 0.09	-1.10 ± 0.11
$05252958-6959234$	4.22	-1.46	4.98 ± 0.10	-1.59 ± 0.11
$05223316-6951389$	5.59	-0.82	4.63 ± 0.33	-1.69 ± 0.15
$05255102-6937103$	5.13	-1.24	6.01 ± 0.06	-1.37 ± 0.11
$05230370-6944219$	5.36	-1.24	6.21 ± 0.11	-1.41 ± 0.11

3.3.3 NGC 1939

In configuring the fields, we assigned some fibres to NGC1939 with the highest priority. As it is a metal-poor globular cluster with a photometrically estimated metallicity of [Fe/H] $= -2.10 \pm 0.19$ (Mackey & Gilmore 2004), it serves as a good test of our ability to identify the metal-poor spectra amongst our CTIO and Spitzer/2MASS stars. Due to the very small size of the cluster with respect to the field of view, only 6 fibres were assigned to the region over the three nights, all from the periphery of the globular cluster.

We found that three of the six stars were likely to be members of NGC1939, with very similar radial velocities, and a low metallicity. Using these three stars, we derived a metallicity of [Fe/H] $= -2.12 \pm 0.13$. The velocity of NGC1939 is estimated to be 259.8 ± 4.7 km s^{-1}. This is the first reliable radial velocity measurement for this LMC globular cluster. Our results are summarised in Table 3.6, inclusive of the stars we rejected based on their spectra, shown in Figure 3.6. These results have been incorporated into (Piatti et al. 2018b), and compare well to both the mean and estimated error of high dispersion measurements from the Gemini 8m telescope.

As seen in Tables B.2 and B.3, the members we have suggested as NGC1939 stars were identified along with other stars from the field as being potentially metal-poor.

Table 3.6: Stars selected from the 2MASS catalogue around the center of NGC1939, with their measured equivalent widths ($\lambda8542 + \lambda8662$), radial velocities, and derived metallicities using equation 3.2 .

Field ID	**Target ID**	$\mathbf{V}_{HEL}$	$\sum$**EW**	**[Fe/H]**	**Reject?**
LMC 26_2	ngc21	270.2 ± 2.8	6.83	-0.57 ± 0.12	yes
LMC 26_2	ngc28	282.5 ± 3.4	4.85	-0.53 ± 0.40	yes
LMC 26_2	ngc38	259.9 ± 2.8	3.18	-2.01 ± 0.11	no
LMC 26_3	ngc36	257.9 ± 3.5	6.43	-0.89 ± 0.52	yes
LMC 26_3	ngc31	259.9 ± 2.5	2.56	-2.54 ± 0.29	no
LMC 26_3	ngc37	259.6 ± 2.8	3.29	-1.82 ± 0.17	no

3.3.4 Metal-Poor Candidates

From our measurements of the equivalent widths of stars in each LMC velocity bin, we identified stars that had combined equivalent widths of less than 4 for the $\lambda8652$ and $\lambda8662$ lines. By using a static cutoff, there is potential to miss some stars that are in the MP category, but from equation 3.1 the brightest stars (with V > 16.2) would have a minimum metallicity of [Fe/H] > -1.9.

We observed a total of 3448 spectra over the three nights, 1999 of which were metal-poor candidates identified from the CTIO data. Spectra were obtained for 656 objects pre-selected based off of Spitzer/SAGE and 2MASS criteria, and 762 spectra using only 2MASS selection criteria, in the regions not covered by Spitzer/SAGE.

From these, a total of 104 spectra were identified as being potentially metal-poor, using the above criterion. Of these 88 were candidates from the CTIO data, 11

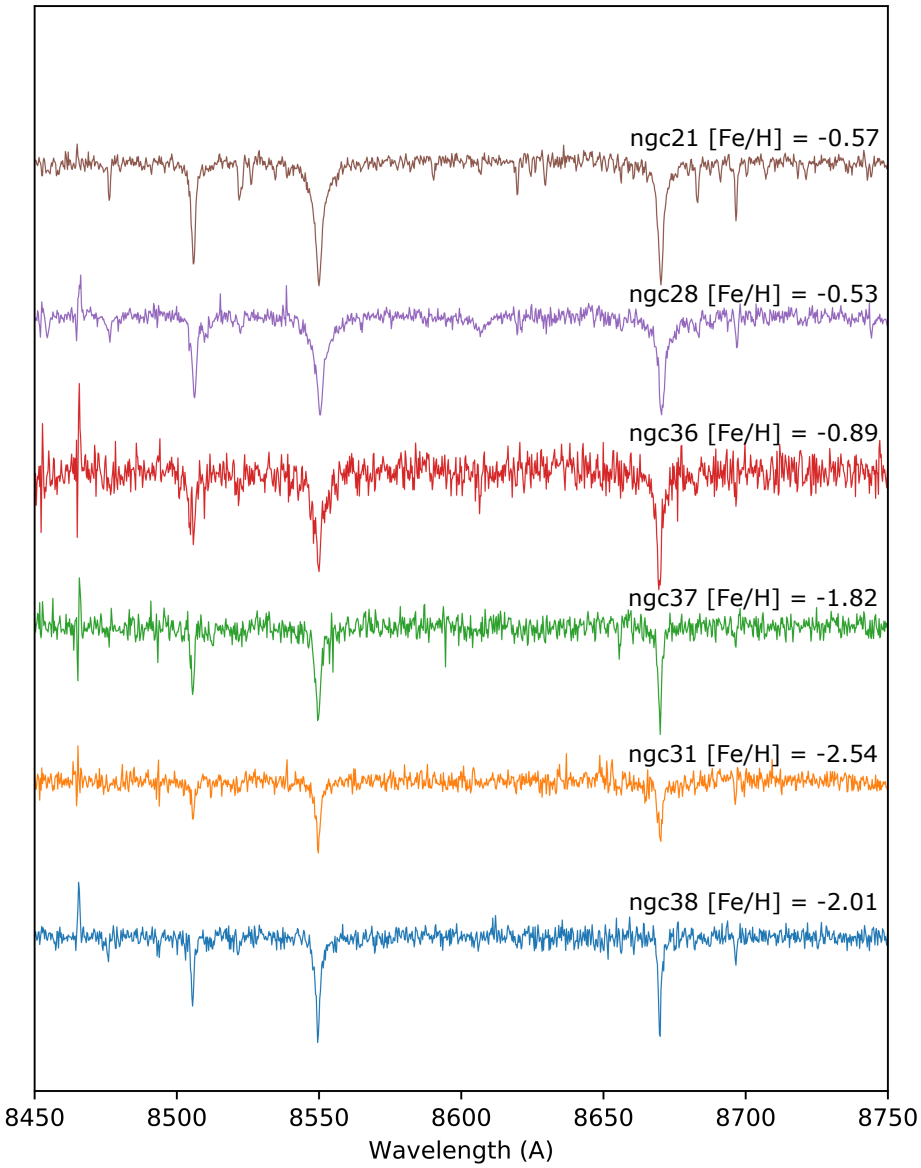

Figure 3.6: The spectra for the observed potential members of NGC1939. Only the lower three spectra are the suspected true members of NGC1939.

were Spitzer-selected, 3 were NGC1939 potential members, and 2 were Cole et al. (2005) stars. The data for these stars are shown in Tables B.1 to B.11.

We show examples spanning the range of metallicities determined using the equivalent widths in Figure 3.7. We can see the presence of some additional lines in the spectra, down to [Fe/H] = −2.0, even with the lower signal-to-noise. Many spectra suffer from low signal-to-noise, which can drown out all the lines but the Ca II triplet.

A total of 35 stars were identified in the VMP category, which is the cutoff we were originally working with in the CTIO data reduction for the inner LMC fields. The distribution of metallicities for all stars in the sample is shown in Figure 3.8. Because of our cutoff criterion for equivalent widths, there will be stars not reported in our sample more metal-rich than [Fe/H] = −1.6, which accounts for the drop-off at higher metallicities.

The mean metallicity of the objects we report on is [Fe/H] = −1.9. Our most metal-poor object was calculated to have a metallicity of [Fe/H] = −2.93, just shy of the EMP threshold. This star had low signal-to-noise, and we estimate the uncertainty in the metallicity to be $\gtrsim 0.2$ dex.

Of the Spitzer objects observed, some have equivalent widths that flag them as metal-poor but show strong iron and titanium lines in their spectra. These stars are likely type M late RGB/AGB stars, with heavy TiO presence in the spectra. The spectra of these objects can be seen in Figures B.6 (636-Sz) and B.12 (840-Sz).

Some objects are brighter than is recommended for using the metallicity calculations based on the equivalent widths, by as much as 1 magnitude. The reported metallicities of any stars outside the ranges $-3 < (V - V_{HB}) < 0$, or $-4 < M_I < 0$ should be treated with scepticism.

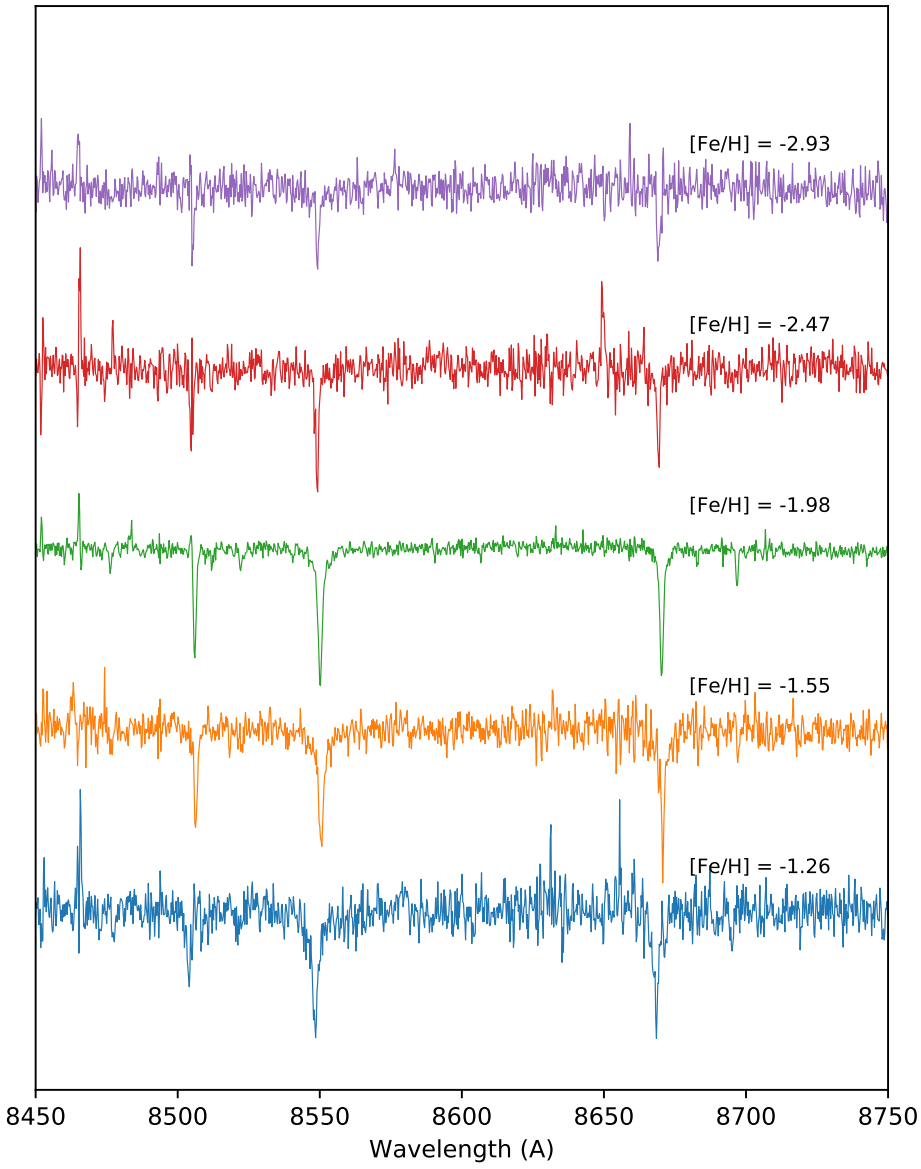

Figure 3.7: A selection of spectra from our results, at steps of roughly 0.5 dex, as listed on the spectra. From top to bottom: LMC26$_1$ 3$_{23}$, LMC26$_3$ 1$_{37}$, LMC25$_1$ 6$_5$, LMC25$_1$ 6$_{22}$, and LMC24 4$_4$.

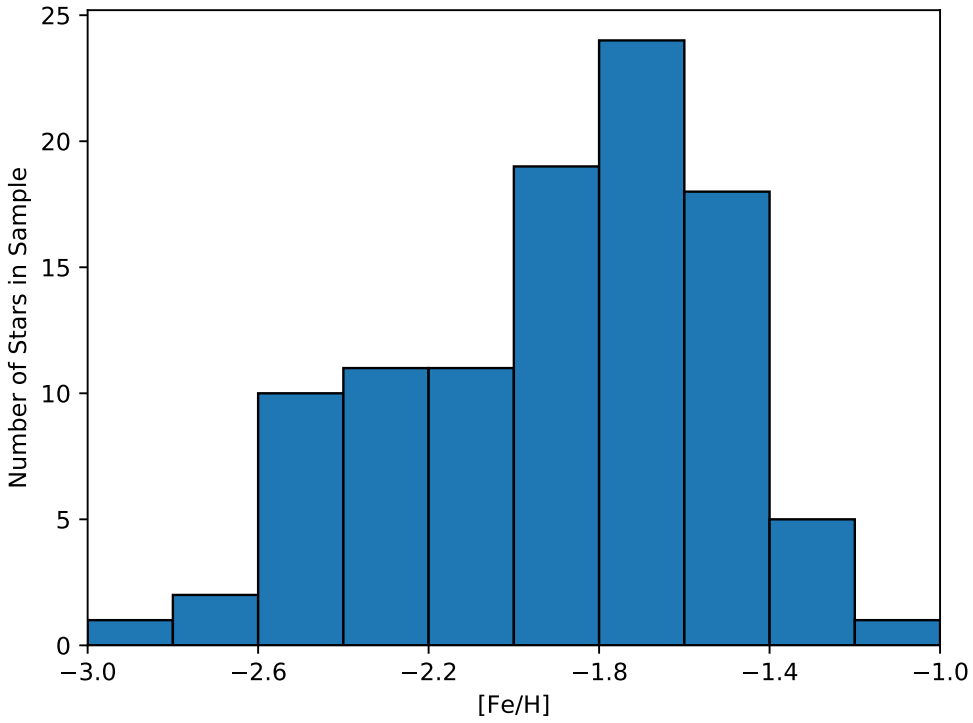

Figure 3.8: Number of stars between [Fe/H] = −1.0 and [Fe/H] = −3.0 from all fields, filtered into bins of 0.2 dex, roughly the size of the errors for our lower S/N stars. The frequency of low metallicity objects drops off sharply as the metallicity decreases, as expected.

Chapter 4

Discussion

4.1 HK Selection

We initially identified 2908 candidate metal-poor objects in our CTIO data in 8 fields of the LMC. We obtained spectra of 1999 of these objects, about 69% of our candidate list. For most of our LMC fields, we observed more than 80% of our candidates, with the exceptions of LMC fields 26 and 24.

We noted that some of the candidates were likely foreground objects in Chapter 2. The number of LMC objects observed can be roughly estimated based on the spectra of the objects. We checked this with our velocity calculations -any object with $v < 150$km s^{-1} were classified as 'non-LMC'. The remaining spectra will inevitably contain some number of MW halo objects, but this method is capable of removing any MW disk and low-velocity halo objects. Some spectra may be falsely rejected if they were too noisy to determine an accurate velocity. In these cases, the spectra would be no use to us for analysis.

For the inner fields (24, 25, and 26), the number of contaminants is minor compared to the number of candidates. In the outermost fields, only ~ 25 fibre objects

are likely to be stars in the LMC. After applying the velocity rejection, we have 1535 stars remaining in our fields, giving an overall rejection rate of $\sim 25\%$.

We examine the efficiency of the selection in Figure 4.1. We see that $\sim 5\%$ of candidates selected using the HK index are flagged as metal-poor after measuring the equivalent widths of the Ca II triplet. The relatively low detection efficiency within each field could be a side effect of the scatter in the HK plot for those fields, LMC field 26 had one of the worst scatters in the HK index of all of our fields, and after accounting for foreground objects in the HK candidates, had the lowest efficiency of all of our fields. This could also prove to be a symptom of an issue with the custom Ca II filter, in which the PSF was not Gaussian. There was an additional halo on bright stars caused by internal reflections from the filter, which makes PSF-Fitting and aperture corrections even more difficult in extremely crowded fields.

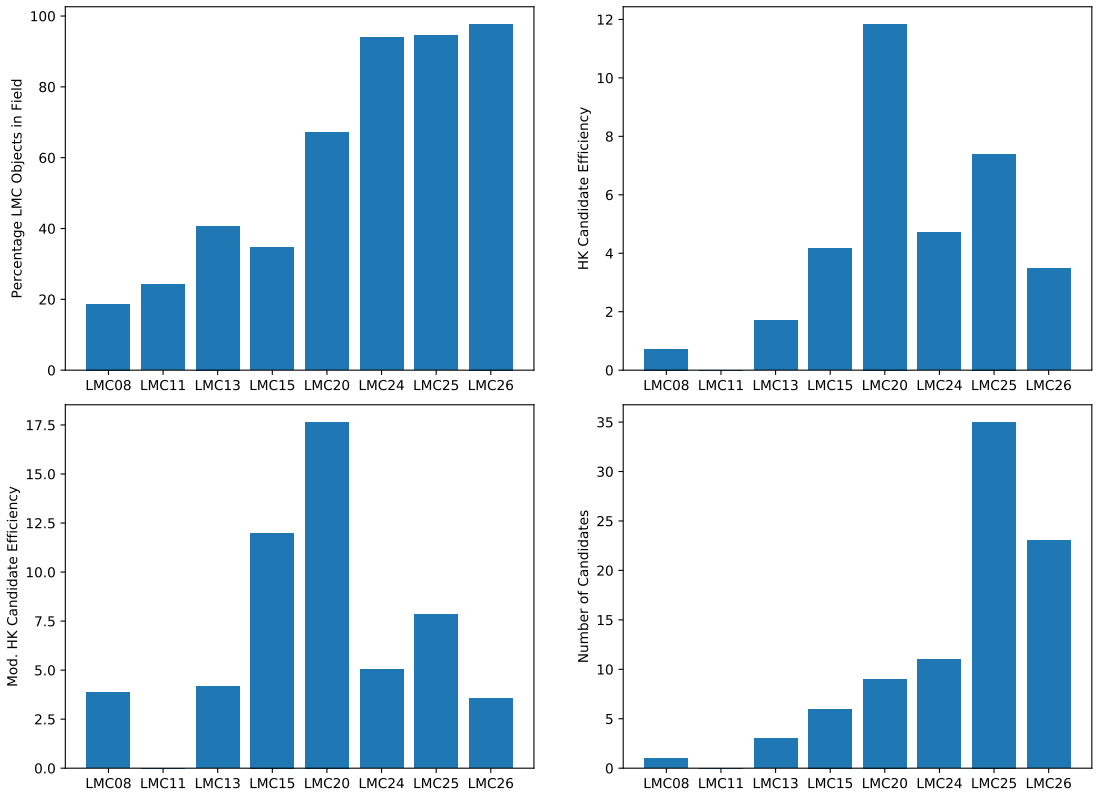

Figure 4.1: A look at the efficiency of the HK index candidate selection by field. *Top left*: The percentage of CTIO-selected candidates that had velocities within the accepted range of LMC velocities. *Top right*: The percentage of CTIO-selected candidates that were flagged as metal-poor based on the equivalent widths of the Ca II triplet. *Bottom left*: The percentage of CTIO-selected candidates flagged as metal-poor, normalised by the number of CTIO candidates accepted as having LMC velocities. *Bottom right*: Total number of CTIO candidates per field.

We also look at the measured HK index of the stars in an example field compared to the derived metallicities of the stars. Figure 4.2 shows the rough upper limit to our HK diagram, selected by being a specified distance from the mean stellar population. There is no obvious trend for metallicity in these diagrams when measuring either the separation from the mean or the HK index itself. There are

interesting stars that appear very blue in M-R, and also a small number of very red stars with low metallicities. The positions of these stars are not apparent when displayed on the corresponding CMD, shown in Figure 4.3.

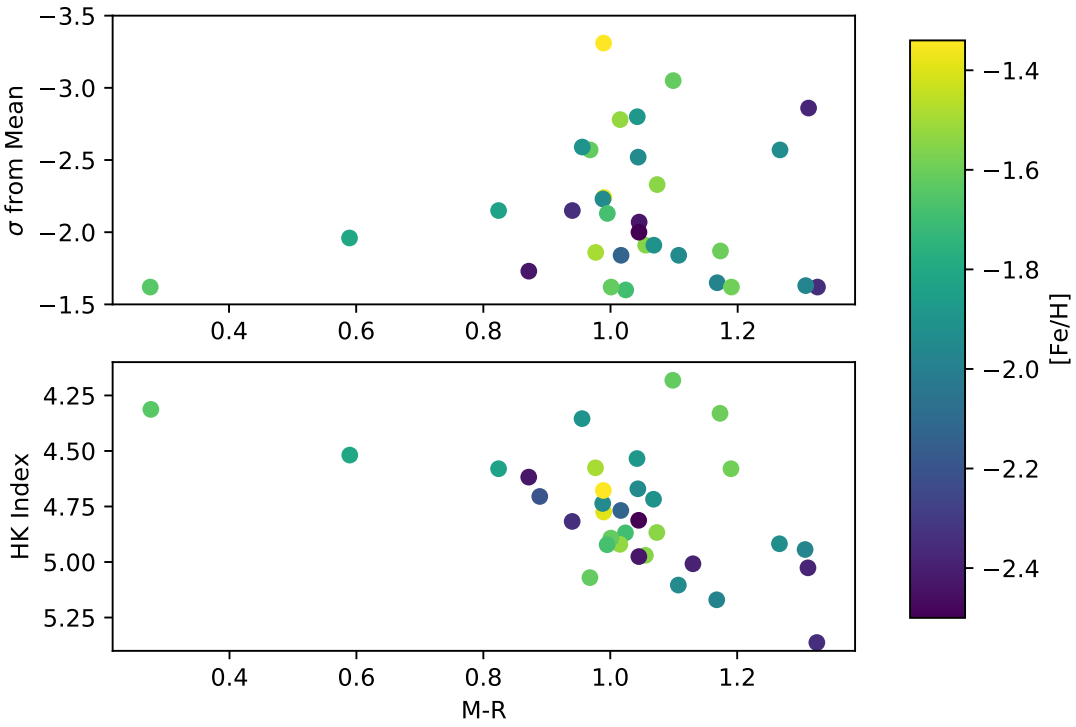

Figure 4.2: The measured HK indices for all stars identified as metal-poor by their spectra in LMC field 25. The top panel shows the distance from the mean of the population on a per-amplifier basis, in standard deviations. The HK diagram for these stars is included in the lower plot.

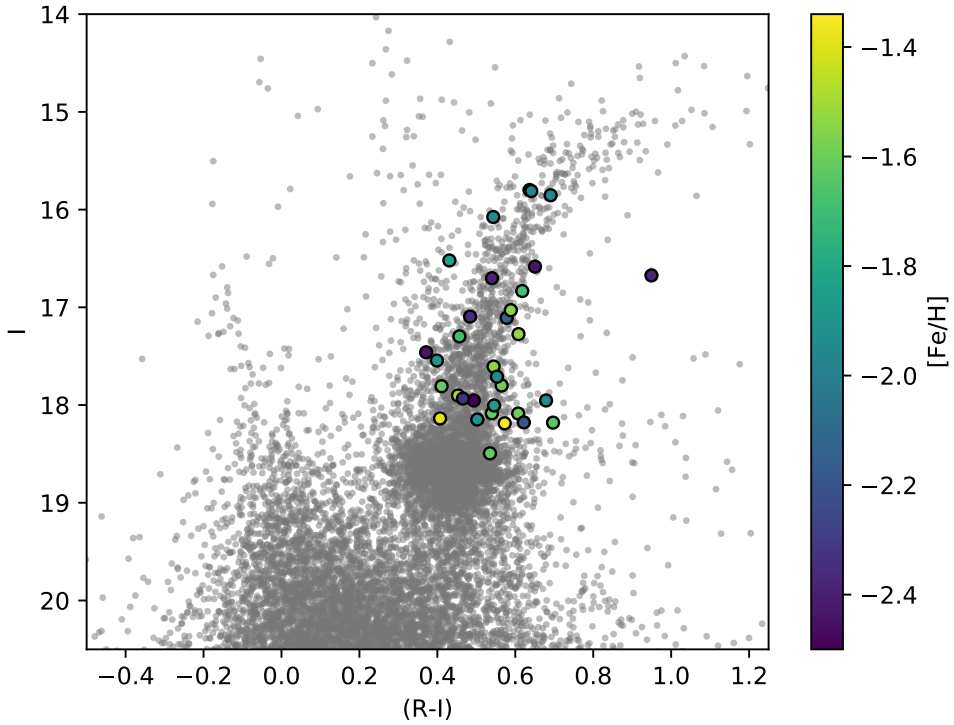

Figure 4.3: The locations of the metal-poor stars from Figure 4.2 on the CMD of LMC field 25.

A majority of the stars do appear to be associated with the RGB of the LMC, with the exception of a single star very redward from the RGB. We are unable to dismiss errors introduced in the photometry as the reason behind the unusual location of this star on the CMD.

There are several types of objects that could be identified as candidate metal-poor stars when classifying by the HK index. Unresolved galaxies were a major source of non-LMC objects in the data set, one that was easily dismissed due to their highly redshifted blue spectra. Another source of potential contamination is chromospherically active stars, which would confuse the HK index with emission

in the wavelengths covered by our calcium filter (e.g. see Figure 4.5). We did note that there were some stars with associated hydrogen emission in our sample, which are likely due to HII regions along the line of sight, seen in Figure 4.4.

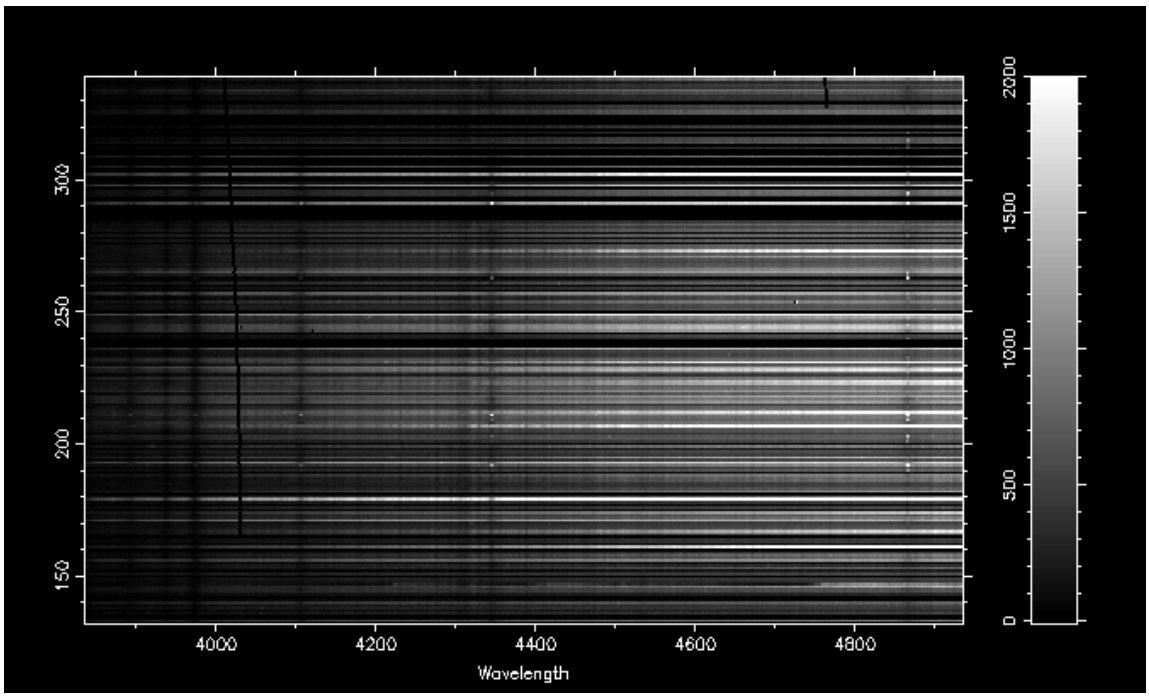

Figure 4.4: A subset of the spectra in LMC field 24, showing a number of stars with associated hydrogen emission. The Hε is visible in the Ca II line in some of the spectra (e.g. #291). The results of a bad pixel column can be seen between the Ca II H line and Hδ. Image is scaled to the 95^{th} percentile count values.

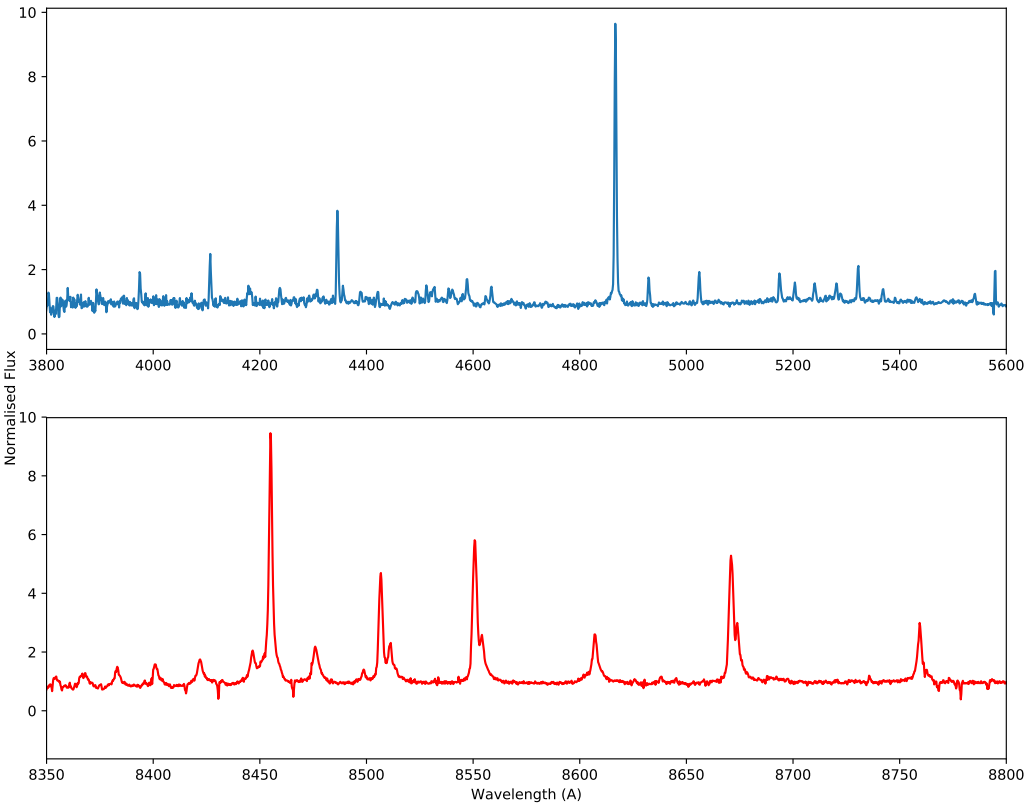

Figure 4.5: An example of a star with a blue spectrum that has a false-positive HK index. This is one of the more extreme examples of emission seen in our candidates. The emission in Hε at λ3970 is within the bandpass of the custom Ca II filter. This object is likely to be an extremely chromospherically active star, or is associated with an H II emission near to the star. This star has $V_{HEL} = 387.3 \pm 11.5$ km s^{-1} and the associated H II emission has $V_{HEL} = 379.2 \pm 14.4$ km s^{-1}.

4.2 Identified Metal-Poor Stars

Our AAO observations resulted in 104 stars of at least MP classification, 34 of which are likely VMP stars. A majority of these stars were located in LMC fields 25 and 26, which is expected given the amount of time dedicated to these fields.

We break down the distribution of metallicities per field in Figure 4.6 for LMC fields 20, 24, 25 and 26 individually. Figure 4.7 details the combined results of the remaining fields, as they contained a very small number of candidates between them.

The peak of the metallicity distribution in LMC field 24 and the combined outer fields is around [Fe/H] = −1.7, whereas the LMC field 25 has the peak in identified stars slightly more metal-poor, at around [Fe/H] = −1.9. LMC field 26 has a large dispersion in the derived metallicities, with the peak occurring at about [Fe/H] = −1.5.

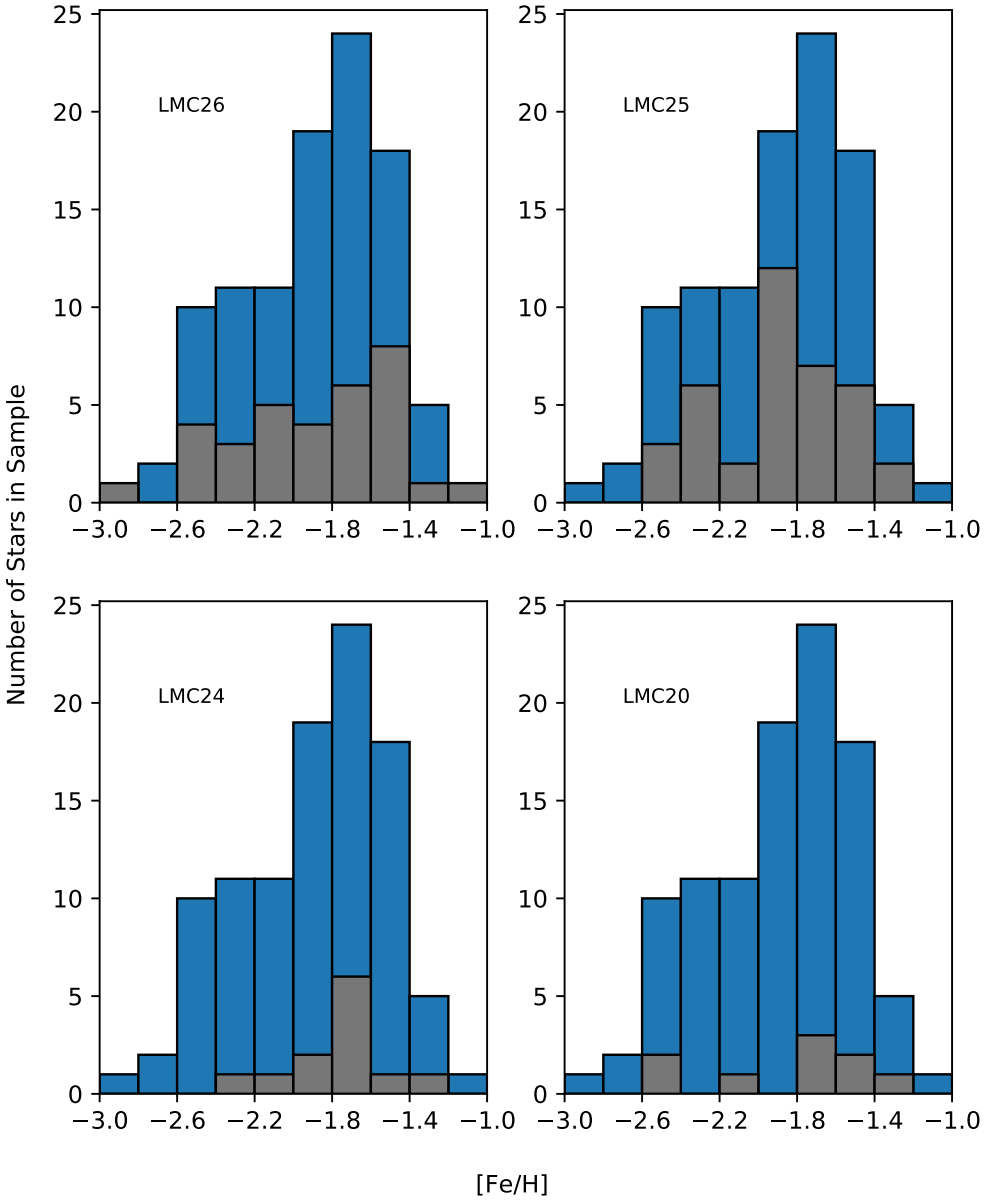

Figure 4.6: Contribution of the inner fields (grey) to the total metallicity distribution (blue) shown in Figure 3.8.

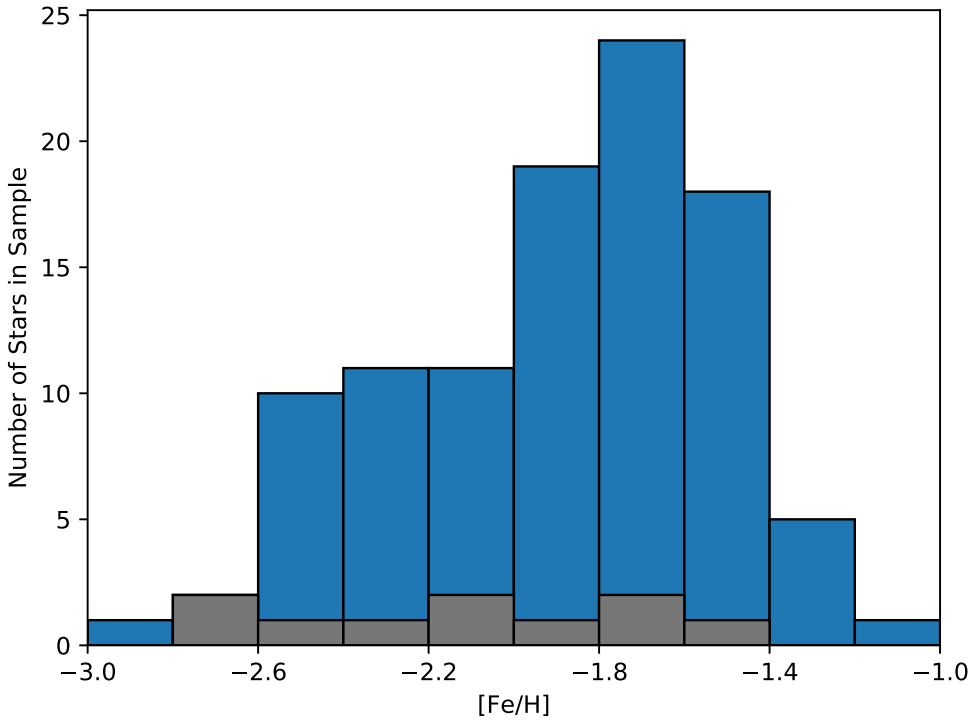

Figure 4.7: Combined contribution of the outer fields (LMC fields 15, 11, 13, and 8 - in grey) to the total metallicity distribution (blue) shown in Figure 3.8.

We look at the velocity distribution of our spectra in Figure 4.8. The mean velocity of all LMC objects that we observed is $v = 256$ km s^{-1}, with $\sigma_v = 29.0$ km s^{-1}. The metal-poor objects in our survey have mean velocity $v = 258$ km s^{-1}, with $\sigma_v = 36.4$ km s^{-1}. This increased dispersion for the metal-poor objects is consistent with the observations in Cole et al. (2005).

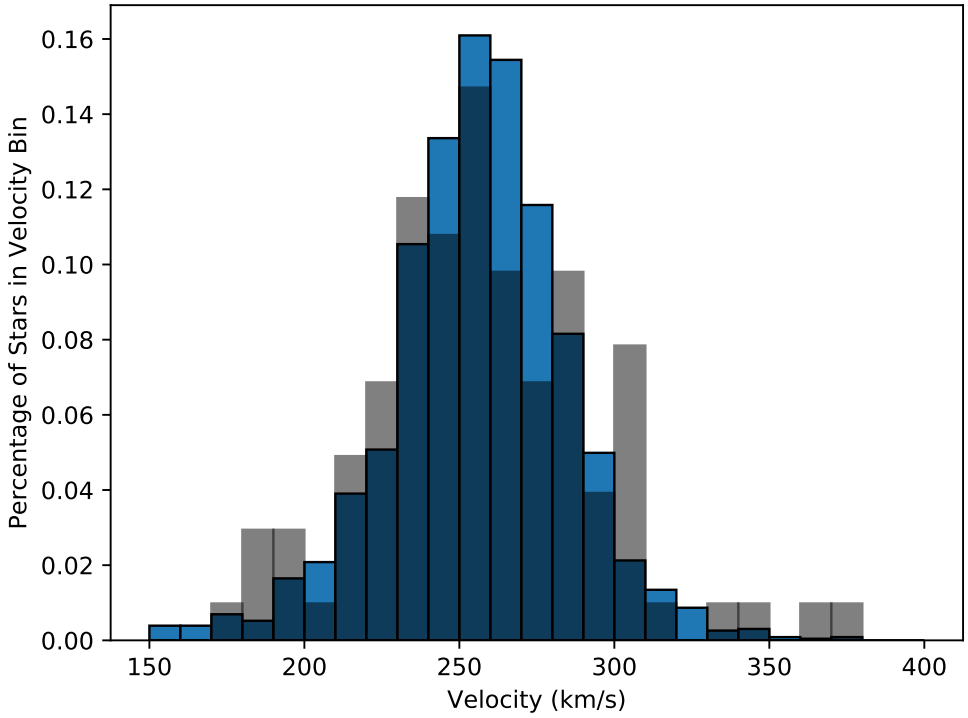

Figure 4.8: The velocity distribution of the metal-poor stars from the tables in Appendix B is shown in grey, compared to the velocity distribution of all LMC stars observed at AAO in blue. The mean velocity of the metal-poor stars is $v = 258$ km s^{-1}, with $\sigma_v = 36.4$ km s^{-1}.

4.2.1 Stars -2 < [Fe/H] < -1

Due to our method of selecting metal-poor stars, we have likely missed a great number of stars in the range $-1.6 <$ [Fe/H] < -1.0. These stars were not the primary focus of this study, but are still of interest for studies of chemical evolution and nucleosynthesis of the LMC disk over the last 10 Gyr (Van der Swaelmen et al. 2013). A total of 69 of our stars fall into the MP category. These stars are listed

in their respective fields in Appendix B.

4.2.2 Stars -3 < [Fe/H] < -2

The following table (4.1) contains the stars for which we have derived a metallicity of [Fe/H] < -2.0. Seven of these objects are Spitzer-selected objects, representing just under 80% of the Spitzer candidates identified in the previous chapter. Three of these objects, 1278-Sz, 996-Sz, and 897-Sz all have $(V - V_{HB})$ that place them above the tRGB. This makes their metallicity estimates unreliable, as the methodology was not calibrated for stars outside of the RGB (Starkenburg et al. 2010).

Table 4.1: List of VMP stars from measurement of the equivalent widths of Ca II triplet, ordered by decreasing metallicity.

Field	**ID**	**[Fe/H]**	**RA**	**Dec**	**Ref. Table**
$LMC8$	6_{16}	-2.00	60.2784625	-64.35233889	B.11
$LMC13$	3_{5}	-2.01	65.17905	-64.80896111	B.9
$LMC26_3$	$996 - Sz$	-2.03	82.20256667	-69.83586944	B.3
$LMC24$	1_{31}	-2.08	76.188475	-68.32318056	B.6
$LMC26_2$	7_{85}	-2.09	81.54134167	-69.67529722	B.2
$LMC26_3$	$897 - Sz$	-2.12	79.77772917	-70.46395833	B.3
$LMC26_1$	1_{40}	-2.13	80.743625	-69.98683056	B.1
$LMC26_3$	$1155 - Sz$	-2.13	79.80668333	-70.071	B.3
$LMC25_1$	5_{20}	-2.13	79.563725	-68.7471	B.4
$LMC15$	5_{17}	-2.13	62.57295833	-66.56230278	B.8

Table 4.2: Continued from Table 4.1

Field	ID	[Fe/H]	RA	Dec	Ref. Table
$LMC25_2$	2_{79}	-2.20	78.95541667	-68.58128333	B.5
$LMC26_1$	8_{46}	-2.22	81.49677917	-69.53025833	B.1
$LMC26_3$	$636 - Sz$	-2.25	81.6692	-70.52192778	B.3
$LMC13$	4_8	-2.28	64.84802083	-64.59836667	B.9
$LMC25_2$	$684 - Sz$	-2.32	77.5740125	-68.39771944	B.5
$LMC25_2$	2_{54}	-2.34	78.52710417	-68.62089722	B.5
$LMC25_1$	3_{10}	-2.35	78.86254167	-68.38204167	B.4
$LMC24$	5_9	-2.35	77.45242917	-68.35164722	B.6
$LMC25_1$	5_{15}	-2.38	80.10868333	-68.64505	B.4
$LMC26_3$	$1278 - Sz$	-2.39	80.96734167	-69.42678056	B.3
$LMC25_2$	4_8	-2.39	79.03309583	-68.28346667	B.5
$LMC25_1$	2_{29}	-2.43	78.88388333	-68.61231111	B.4
$LMC25_1$	6_{12}	-2.43	79.76059583	-68.59452222	B.4
$LMC26_3$	$1107 - Sz$	-2.46	80.64054167	-69.00909444	B.3
$LMC26_3$	1_{37}	-2.47	80.67133333	-70.06971111	B.3
$LMC26_3$	4_{97}	-2.47	80.53413333	-69.61342222	B.3
$LMC25_1$	4_{36}	-2.50	78.9665375	-68.24855	B.4
$LMC20$	3_7	-2.50	69.26322917	-67.31796944	B.7
$LMC15$	1_{20}	-2.50	62.32884583	-66.55605278	B.8
$LMC20$	4_1	-2.52	69.0176875	-67.26973611	B.7
$LMC26_3$	$ngc31$	-2.54	80.3425125	-69.95204167	B.3
$LMC15$	7_9	-2.60	63.105	-66.228025	B.8
$LMC13$	5_3	-2.69	65.9377375	-65.11655278	B.9
$LMC26_1$	3_{23}	-2.93	80.24459167	-69.80548889	B.1

Previously, only a handful of stars with metallicity [Fe/H] < -2.0 were known in the LMC. Our results greatly increase the number of known VMP LMC stars.

4.2.3 Potential EMP Stars in the LMC

There were no stars detected with Ca II triplet equivalent widths that resulted in a derived metallicity of [Fe/H] < -3.0. However, from our metal-poor calibration stars, we know that there is the potential to underestimate how metal-poor an object is. Taking this into account with the errors in our metallicity, there is a potential for two of our stars to fall within the EMP category, star 3_{23} in LMC field 26, and star 5_3 in LMC field 25.

3_{23} has 2MASS designation 05205870-6948197, and 5_3 has 2MASS designation 04234505-6506595. Our measured equivalent widths for each star are given in table 4.3.

The red spectrum for our most metal-poor candidate is noisy, with a signal-to-noise of $\sim$15. As we have spectra at blue wavelengths, we can also test the strength of the Ca II H & K lines. Figure 4.9 shows our potential EMP star compared to two of our metal-poor calibration stars, after accounting for radial velocity. The widths of the Ca II H & K lines for 2M05205870-694819 aren't as narrow as HE0305 at [Fe/H] $= -3.56$. We see that when compared to CS 31072, at [Fe/H] $= -2.94$, the widths of the Ca II H & K lines are narrower and weaker than the metal-poor calibrator. The CH/Fe blend at λ4308 is comparable to that of HE0305, which is not carbon enhanced, with [C/Fe] $= +0.27$ (Placco et al. 2014).

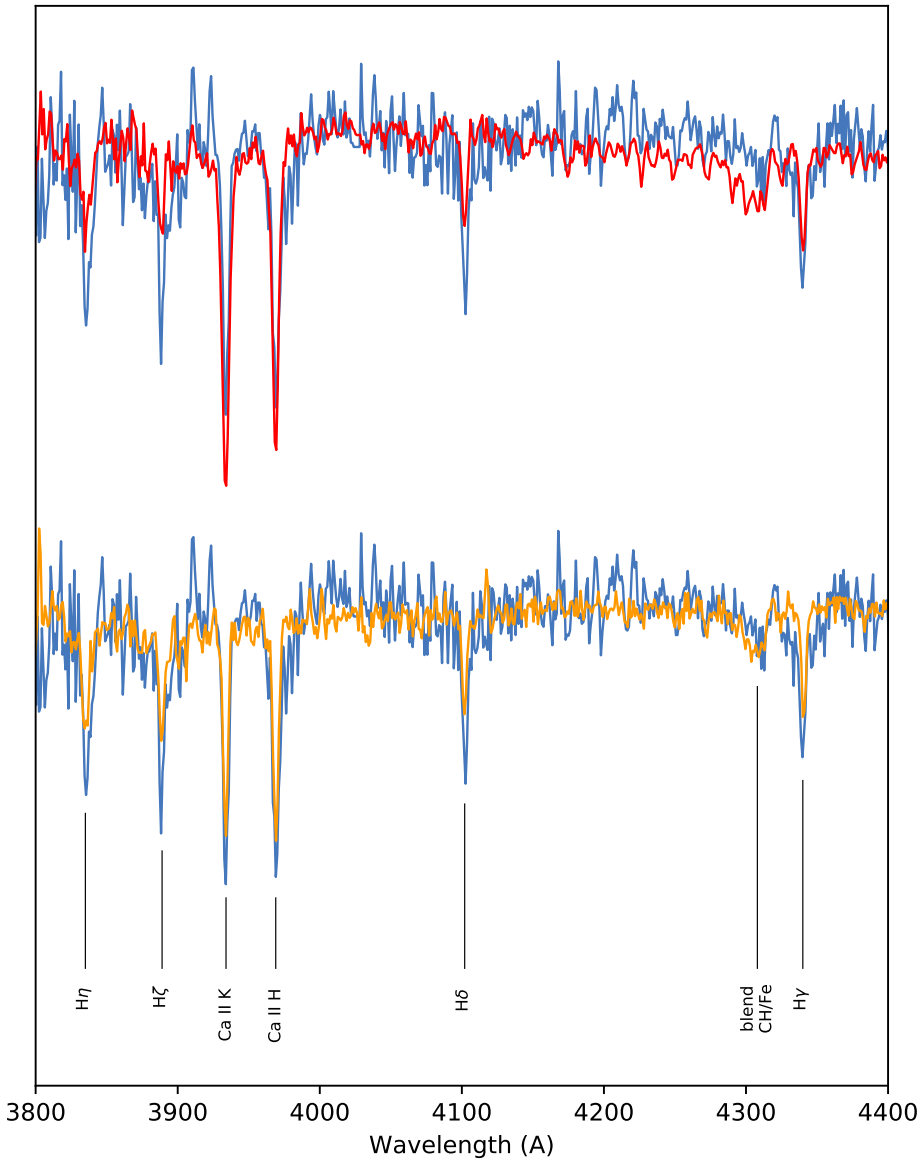

Figure 4.9: Normalised spectrum for metal-poor candidate in LMC field 26_1, ID: 3_{23}. Overlaid in red (top) is the spectrum for CS 31072-118, with [Fe/H] = −2.94, overlaid in orange (bottom) is the spectrum for HE0305-5442, with [Fe/H] = −3.56. Spectra have been shifted to rest-frame wavelengths.

The same comparison is used on 2M04234505-6506595 in Figure 4.10. This star shows much stronger Ca II H & K lines, with both metal-poor calibration stars having narrower lines than our star. The CH/Fe blend is very pronounced in our star, indicating potential carbon enhancement. It should be noted that this star is very bright, lying above the tRGB of the LMC, so the metallicity calibrations in Starkenburg et al. (2010) cannot be applied accurately. The equivalent widths of this object are still very narrow, and its brightness makes it a suitable target for follow-up spectroscopic observations at higher resolution.

Table 4.3: Potential EMP stars in the LMC, and the equivalent widths in Angstroms of all three lines of the Ca II triplet.

2MASS ID	$\mathbf{M}_I$	$\mathbf{EW}_{\lambda 8498}$	$\mathbf{EW}_{\lambda 8542}$	$\mathbf{EW}_{\lambda 8662}$
04234505-6506595	-1.91	0.43	0.92	0.78
05205870-6948197	-4.63	0.66	1.42	1.28

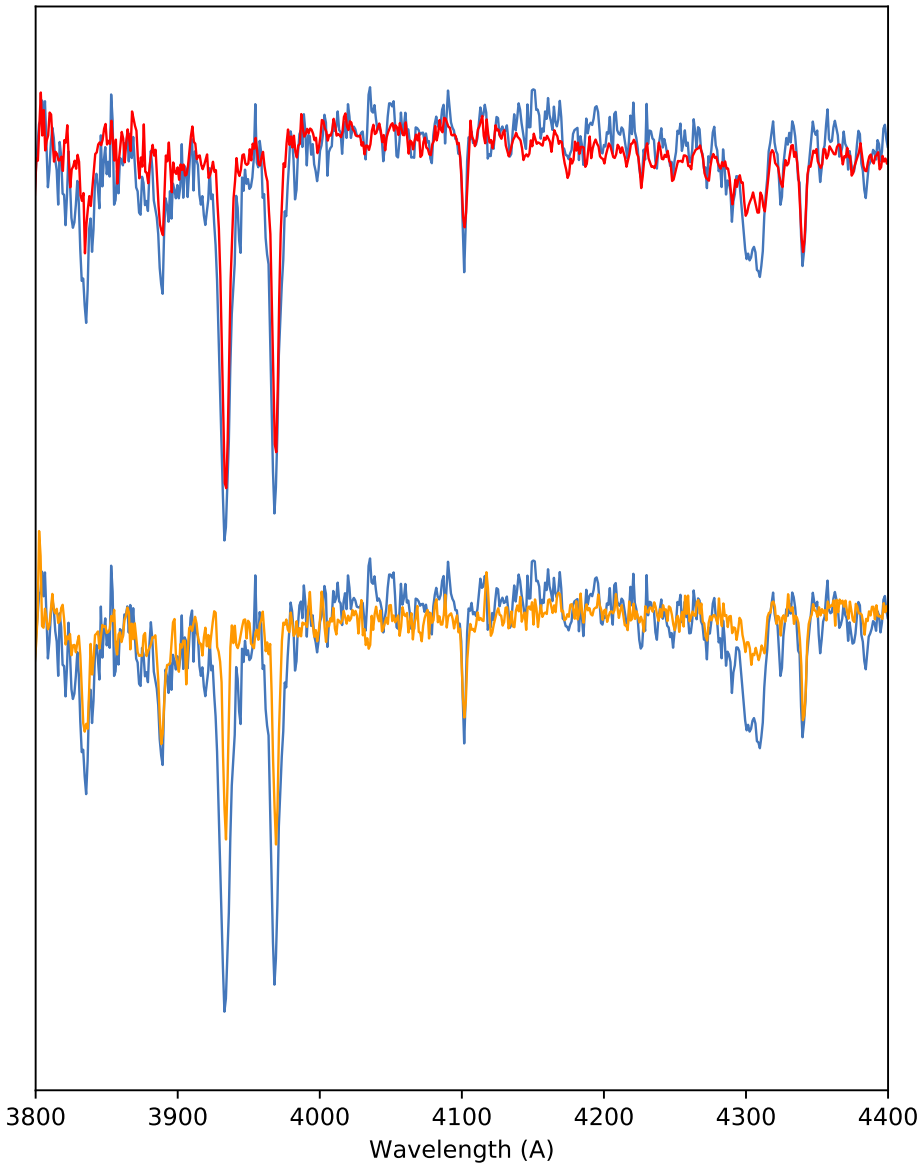

Figure 4.10: To compare to Figure 4.9, the second most metal-poor star from our sample is shown: from LMC field 13, ID 5_3. Overlaid spectra are as in Figure 4.9.

4.3 Concluding Remarks

From Cole et al. (2005), only 10% of RGB stars had [Fe/H] < -0.7, with only 5% being more metal-poor than [Fe/H] $= -1.1$. Our resultant spectra were screened for stars exhibiting narrow Ca II triplet lines, resulting in 104 identified spectra. 33% of those identified stars are in the VMP category, with two star potentially classifiable as EMP. These stars are the most metal-poor stars currently known in the LMC, with [Fe/H] $= -2.93$ and [Fe/H] $= -2.69$.

The number of confirmed metal-poor candidates varied drastically from field to field and appeared to have some relation to the quality of the photometry in those fields. With high-precision photometry, the identification rate of metal-poor objects could be in excess of 20%. Given the distribution of metal-poor stars in the LMC, our selection techniques have been broadly successful in identifying metal-poor stars in the LMC, greatly expanding the known number of VMP stars. The frequency of metal-poor stars we observed appears to be consistent with the observed frequency versus metallicity trend reported for the MW. We observed approximately a factor 10 decrease in frequency for each 1 dex decrease in metallicity over a 1.5 dex range.

From our sample, eight stars are more metal-poor than [Fe/H] $= -2.5$, and thus warrant further investigation with high-resolution spectroscopy. This study has only scratched the surface of the oldest and most metal-poor stars to be found. There is great potential to further increase the number of identified metal-poor objects in the LMC.

Appendix A

Photometry: Additional Figures and Tables

Table A.1: Summary observation log for CTIO data.

Field ID	**Night**	**I**	**R**	**M**	**C**	**DDO51**	**Ca**	**Seeing**
PG 0231	27 Dec	1	1	2	10	15	90	0.9”
LMC 16	27 Dec	30	30	60	-	120	1080 × 2	1.1”
LMC 17	27 Dec	30	30	60	-	360	1080 × 2	1.1”
LMC 26	27 Dec	30	30	60	-	360	1080 × 2	1.2”
SA 98	27 Dec	1	1	2	8	-	120	1.0”
SA 101	27 Dec	4	4	4	20	-	240	1.0”
NGC 1851	27 Dec	2	2	4	20	-	240	0.8”
LMC 25	27 Dec	30	30	60	-	360	1080 × 2	1.2”
NGC 4590	27 Dec	3	3	6	15	-	300	1.0”
SA 101	27 Dec	4	4	4	20	-	240	1.0”
SA 98	27 Dec	1	1	2	8	-	120	1.0”

Table A.2: Summary observation log for CTIO data - continued.

Field ID	**Night**	**I**	**R**	**M**	**C**	**DDO51**	**Ca**	**Seeing**
PG 0231	28 Dec	2	2	2	10	15	150	1.0”
HE 0044	28 Dec	1	1	2.5	10	20	150	1.1”
47 Tuc	28 Dec	1	1	2.5	15	-	240	1.3”
LMC 11	28 Dec	30	30	60	420	360	1080 × 2	1.2”
LMC 18	28 Dec	30	30	60	420	360	1080 × 2	1.3”
LMC 19	28 Dec	30	30	60	420	360	1080 × 2	1.2”
SA 98	28 Dec	1	1	2	8	-	150	1.5”
SA 98 13’ NE	28 Dec	1	1	2	8	-	150	1.5”
SA 101	28 Dec	4	4	4	20	-	240	1.6”
LMC 24	28 Dec	30	30	60	-	360	1080 × 2	1.6”
HE 0557	28 Dec	15	15	20	80	120	300 + 600	1.3”
SA 101	28 Dec	4	4	4	20	-	240	1.1”
SA 98	28 Dec	1	1	2	8	-	150	1.7”
SA 98 13’ N	28 Dec	1	1	2	8	-	150	1.7”
PG 0231	29 Dec	2	2	2	10	15	150	1.4”
HE 0107	29 Dec	15	15	20	150	150	420 × 2	1.2”
LMC 14	29 Dec	30	30	60	300	360	1080 × 2	1.4”
LMC 21	29 Dec	30	30	60	-	360	1080 × 2	1.6”
LMC 22	29 Dec	30	30	60	-	360	1080 × 2	1.5”
SA 98	29 Dec	1	1	2	8	-	150	1.1”
SA 98 6’ S	29 Dec	1	1	2	8	-	150	1.3”
SA 101	29 Dec	4	4	4	20	-	240	1.6”

Table A.3: Summary observation log for CTIO data - continued.

Field ID	**Night**	**I**	**R**	**M**	**C**	**DDO51**	**Ca**	**Seeing**
NGC1904	29 Dec	3	3	4.5	25	-	300	1.1”
LMC 23	29 Dec	30	30	60	-	360	1080 × 2	1.4”
SA 101	29 Dec	4	4	4	20	-	240	1.3”
SA 101 9’N 3’E	29 Dec	4	4	4	20	-	240	1.2”
SA 98	29 Dec	1	1	2	8	-	150	1.2”
SA 98 6’ S	29 Dec	1	1	2	8	30	150	1.2”
SA 101	29 Dec	4	4	4	20	-	240	1.6”
PG 0231	30 Dec	2	2	2	10	15	150	0.9”
HE 0107	30 Dec	2	2	3	20	35	240	1.0”
LMC 8	30 Dec	30	30	60	300	360	1080 × 2	1.1”
LMC 15	30 Dec	30	30	45	300	300	1080 × 2	0.9”
LMC 13	30 Dec	20	20	30	300	270	1080 × 2	1.0”
SA 98	30 Dec	1	1	2	8	-	150	0.9”
SA 98 5’E 5’N	30 Dec	1	1	2	8	-	150	0.9”
SA 101	30 Dec	3	3	3	15	-	180	1.0”
LMC 20	30 Dec	20	20	45	-	300	1080 × 2	1.0”
Mel 66	30 Dec	1	1	2.5	20	20	210	1.0”
SA 101	30 Dec	3	3	3	15	-	180	1.0”
SA 98	30 Dec	1	1	2	8	-	150	0.9”

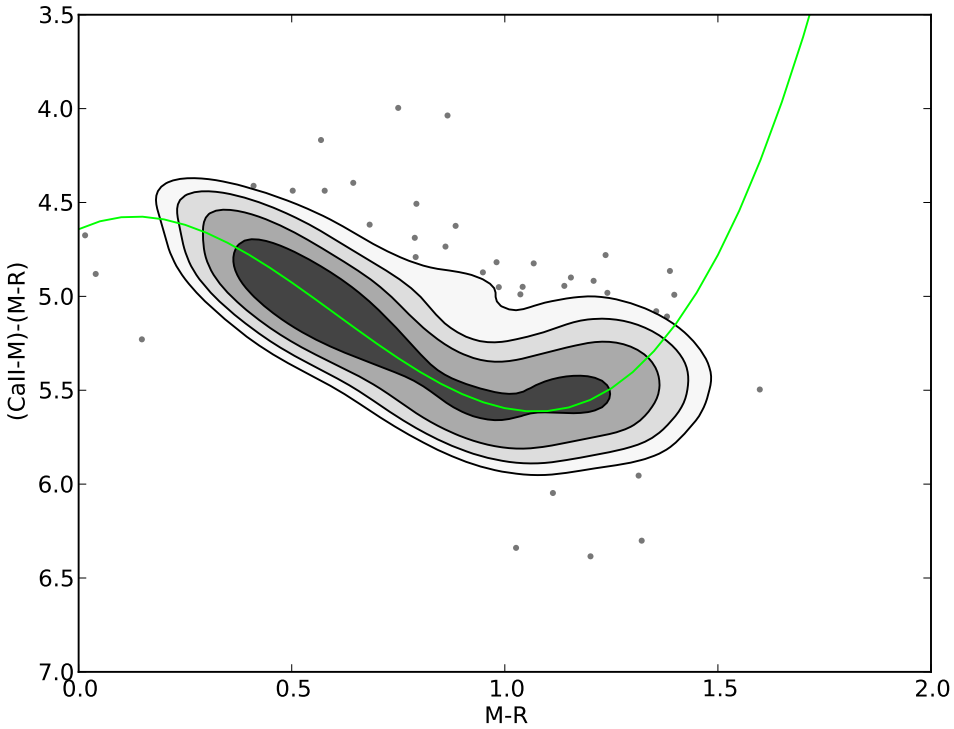

Figure A.1: Our fit to the data for LMC field 15 when the background galaxies are still included. The inclusion of these non-RGB objects increases the spread of the population slightly in HK space, but does not have a large effect on the candidature of metal-poor stars.

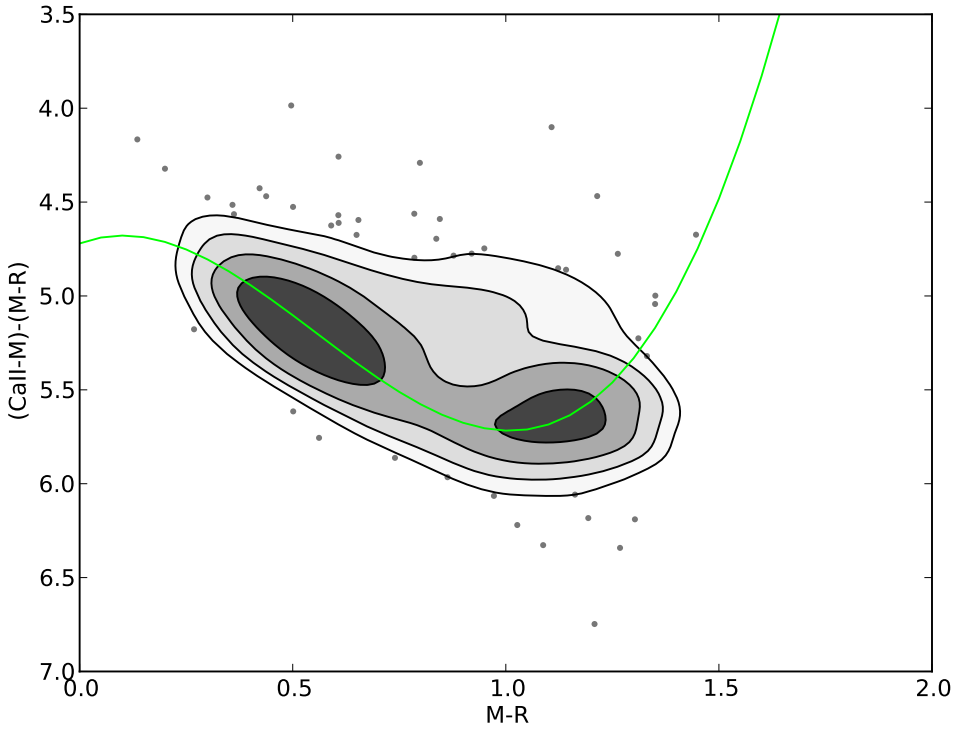

Figure A.2: Our fit to the data for LMC field 13 when the background galaxies are still included.

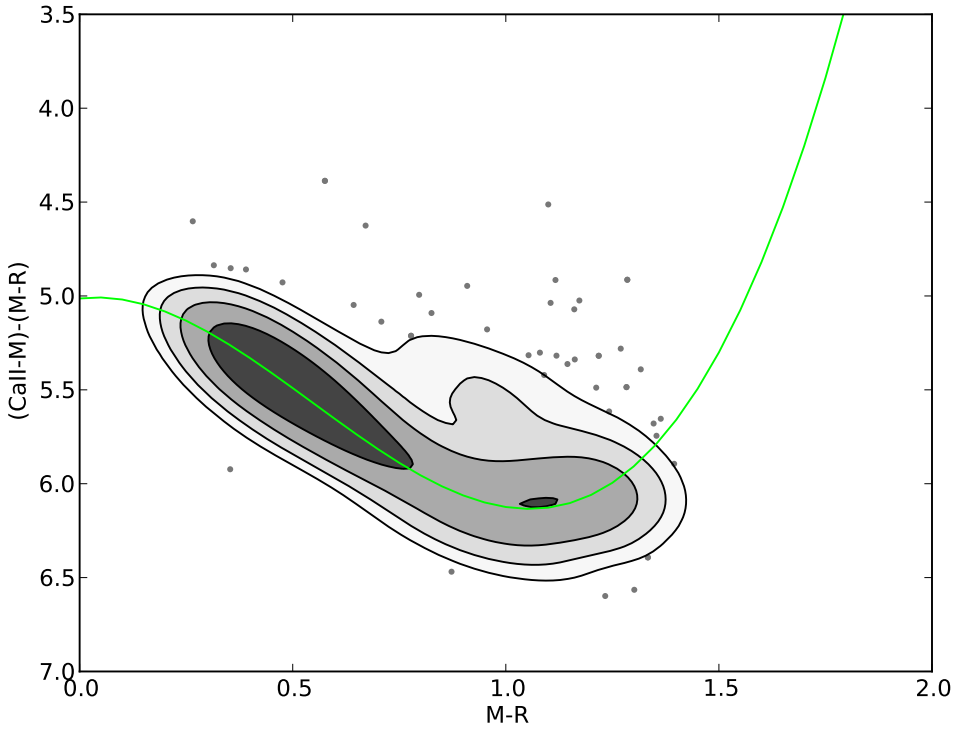

Figure A.3: Our fit to the data for LMC field 11 when the background galaxies are still included.

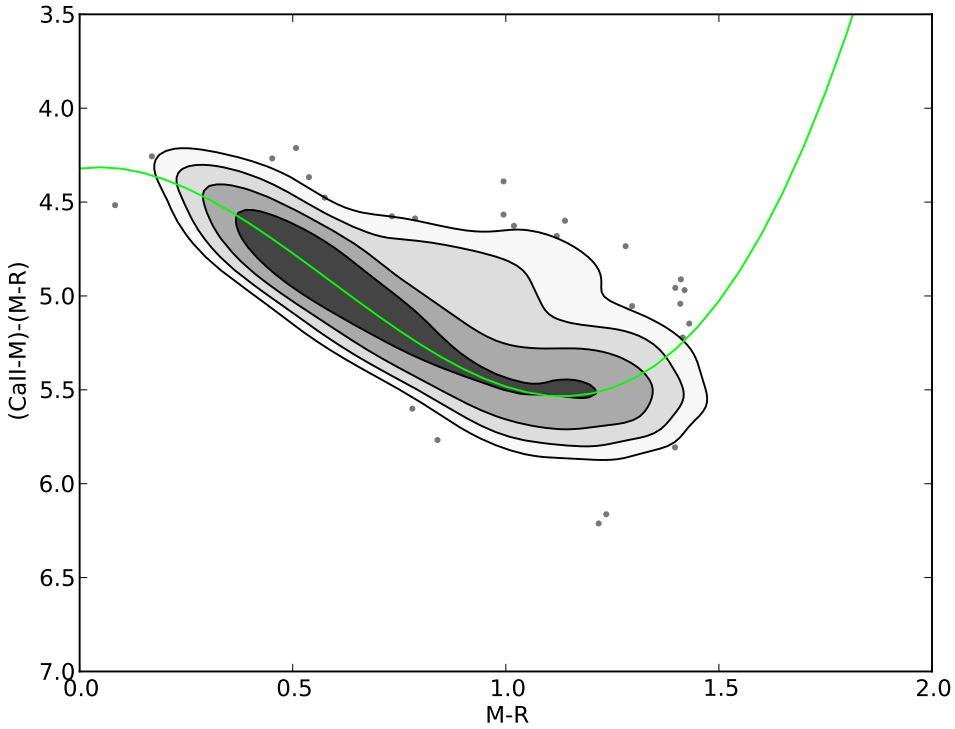

Figure A.4: Our fit to the data for LMC field 8 when the background galaxies are still included.

A.1 Example HK Residual Figures

In the following figures, we show for each field an example HK residual plot (the outer fields show all data available in that field). In each figure, the contour levels are normalised densities of the point in HK space, at levels of 0.5, 0.25, 0.125, and 0.0625, from darkest to lightest, respectively. The black diamonds are all candidate stars within the displayed data, which have typical error bars equal to those given in the diagram. The 2σ variance of the data is given by the two dotted red lines.

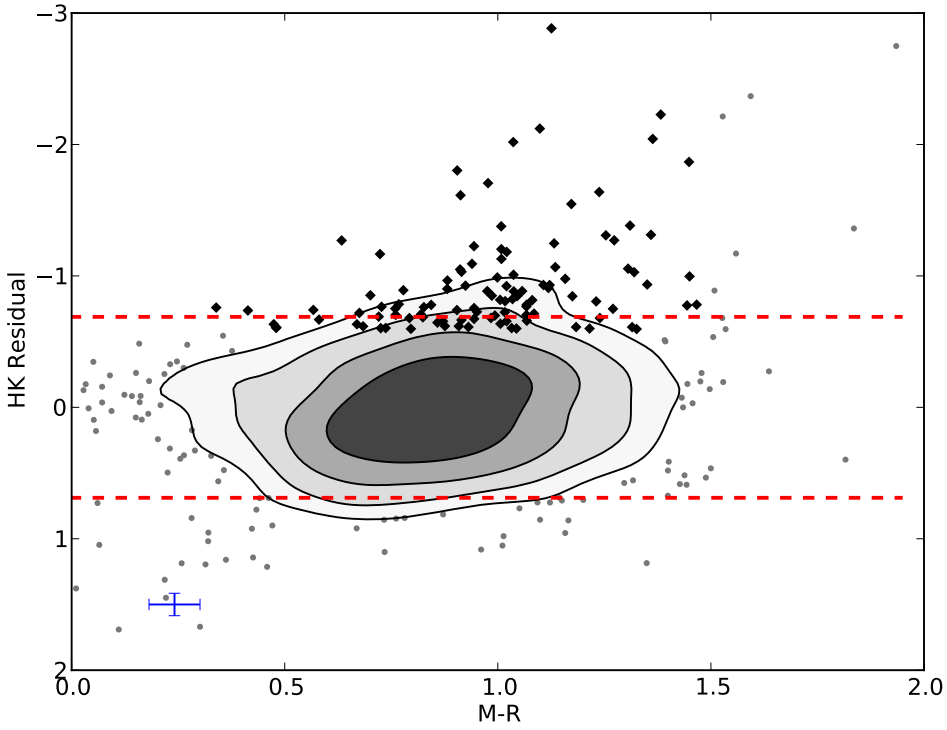

Figure A.5: HK index residuals from our fit to the data, for a single amplifier in LMC field 26.

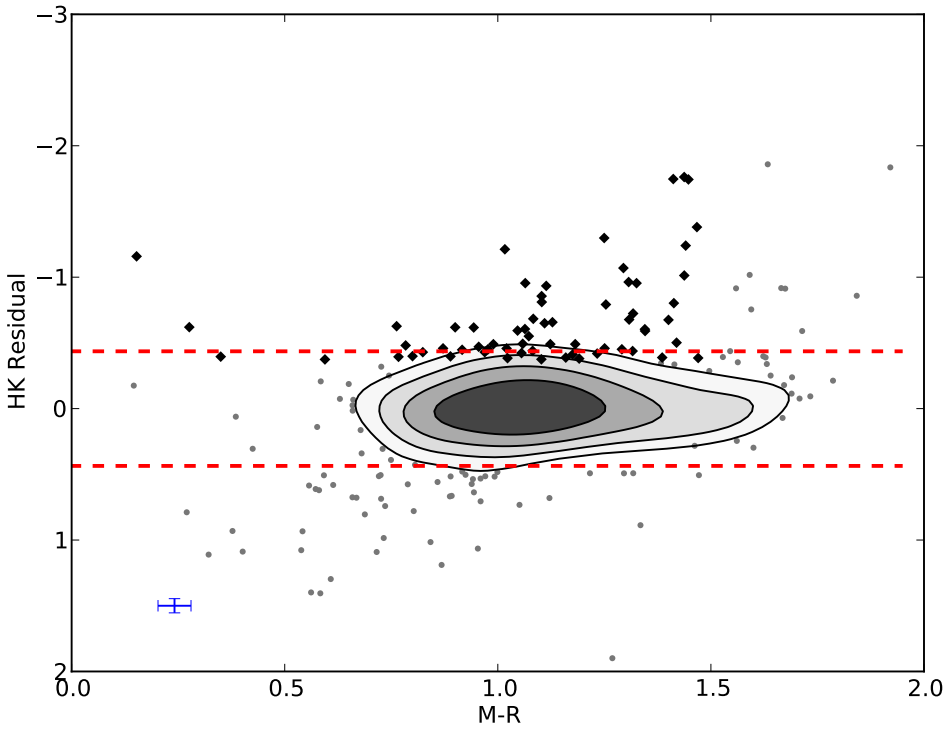

Figure A.6: HK index residuals from our fit to the data, for a single amplifier in LMC field 25.

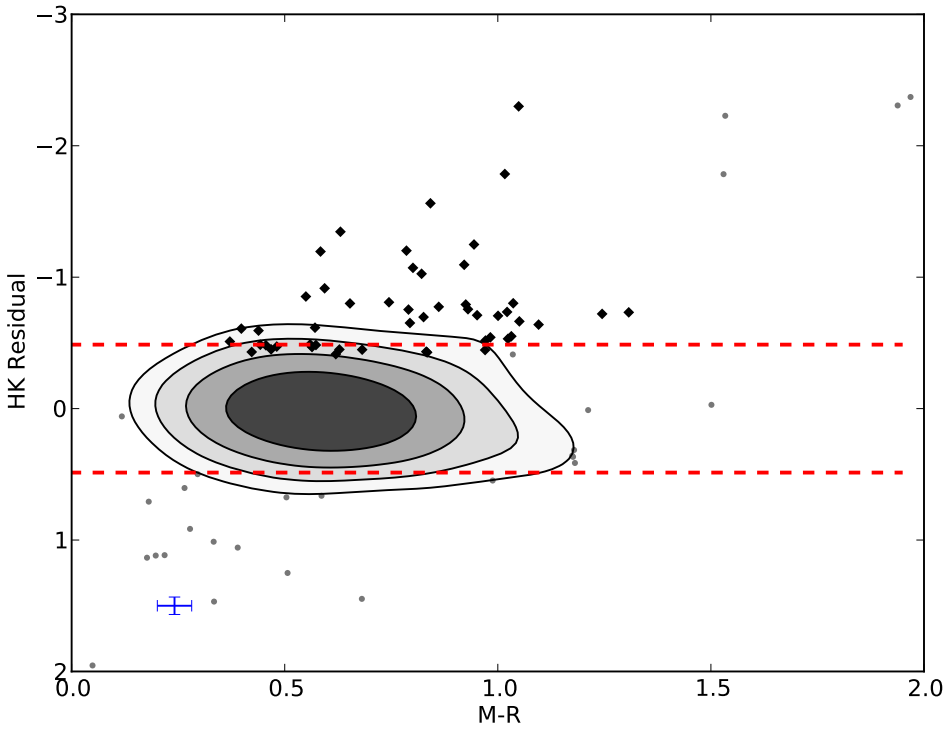

Figure A.7: HK index residuals from our fit to the data, for a single amplifier in LMC field 24.

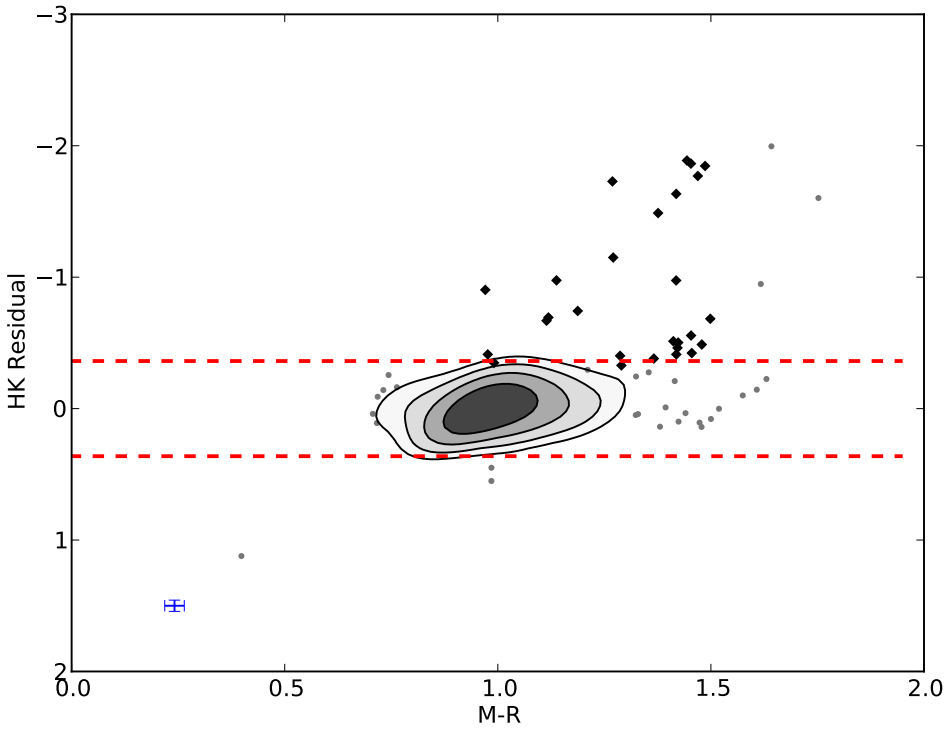

Figure A.8: HK index residuals from our fit to the data, for a single amplifier in LMC field 20.

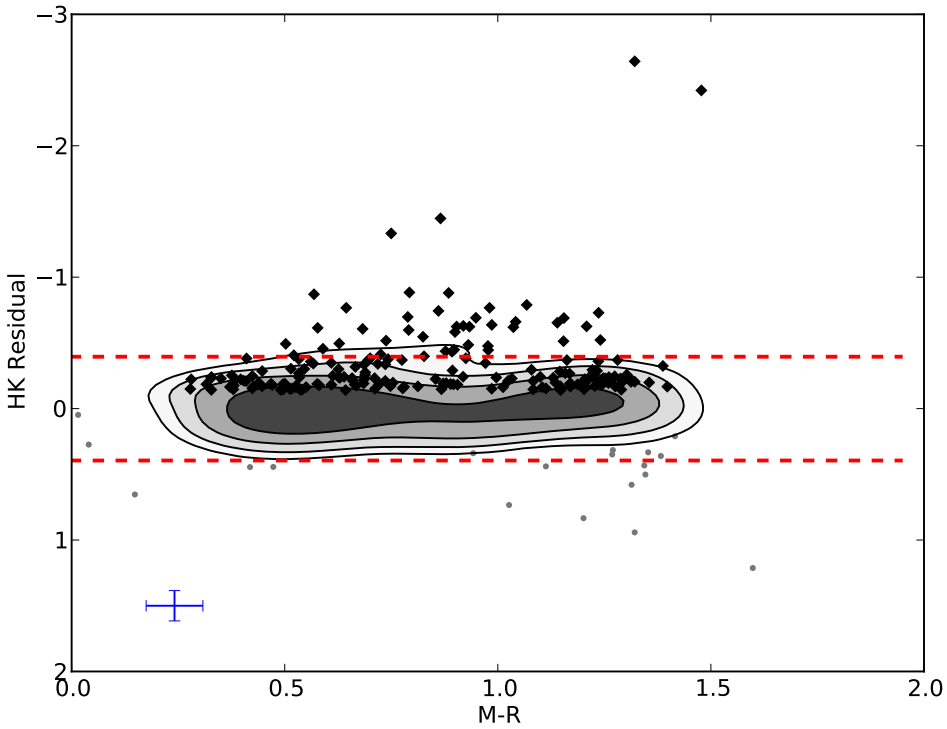

Figure A.9: HK index residuals from our fit to the data, for all available data in LMC field 15.

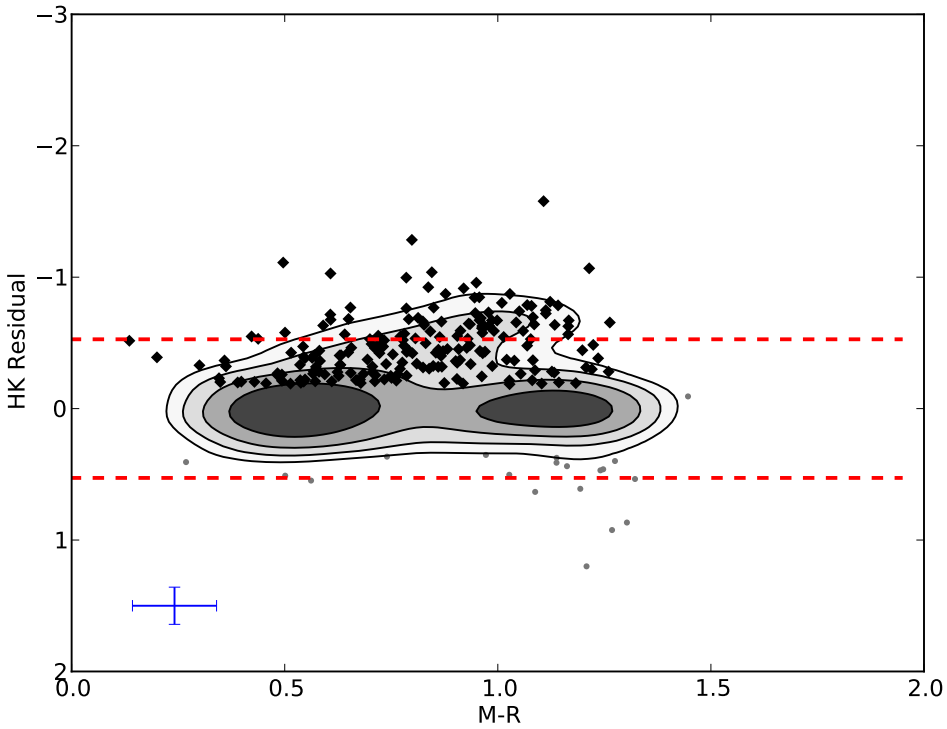

Figure A.10: HK index residuals from our fit to the data, for all available data in LMC field 13.

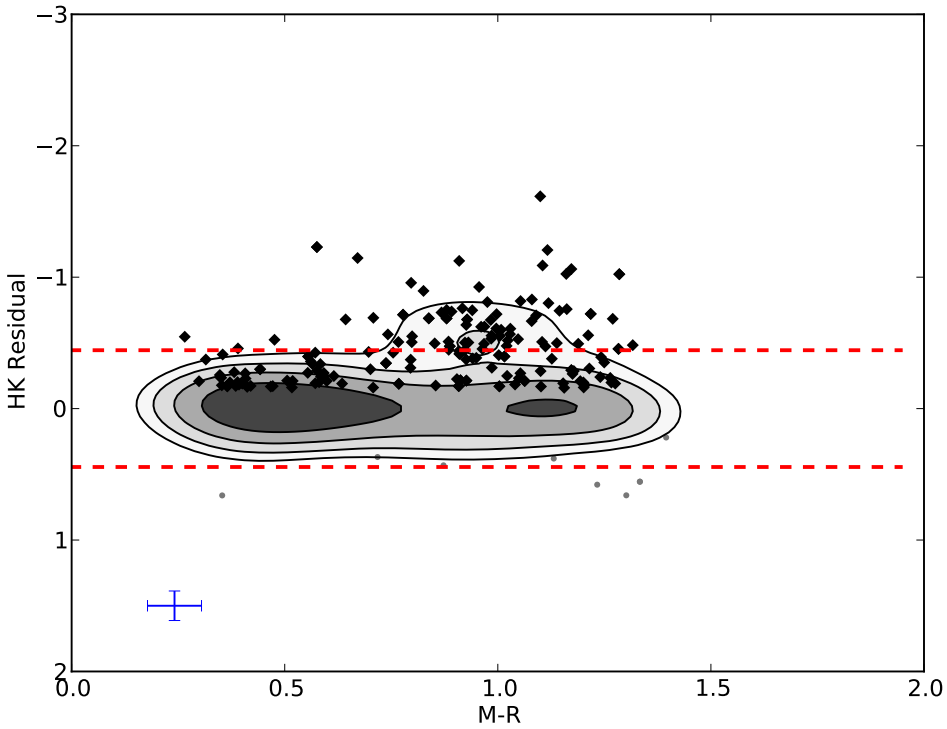

Figure A.11: HK index residuals from our fit to the data, for all available data in LMC field 11.

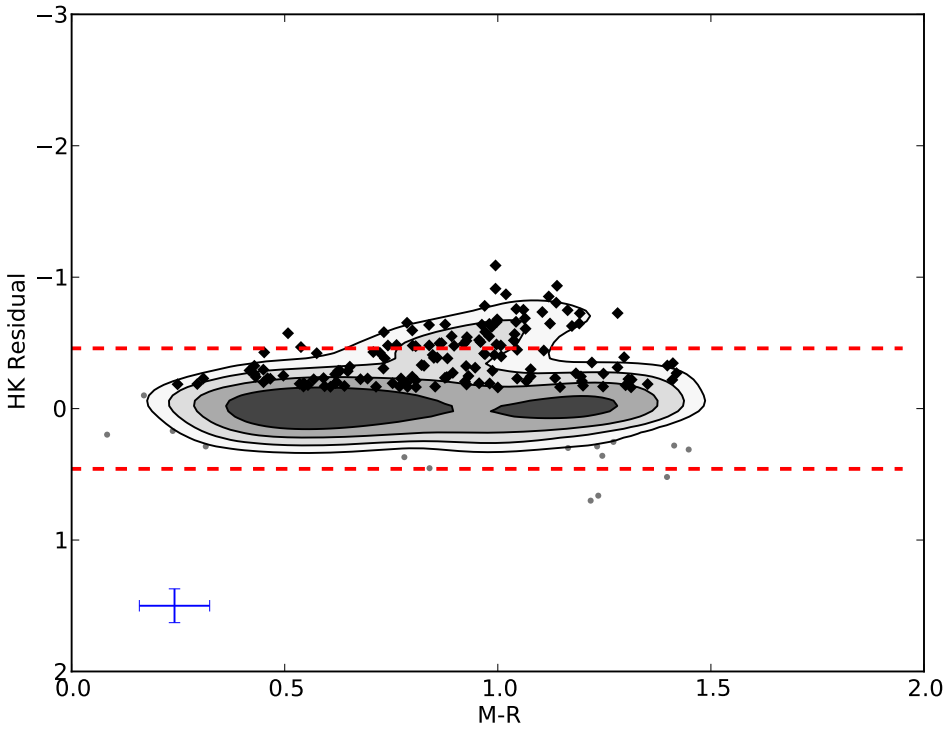

Figure A.12: HK index residuals from our fit to the data, for all available data in LMC field 8.

A.2 Surface Gravity Rejection in Outer Fields

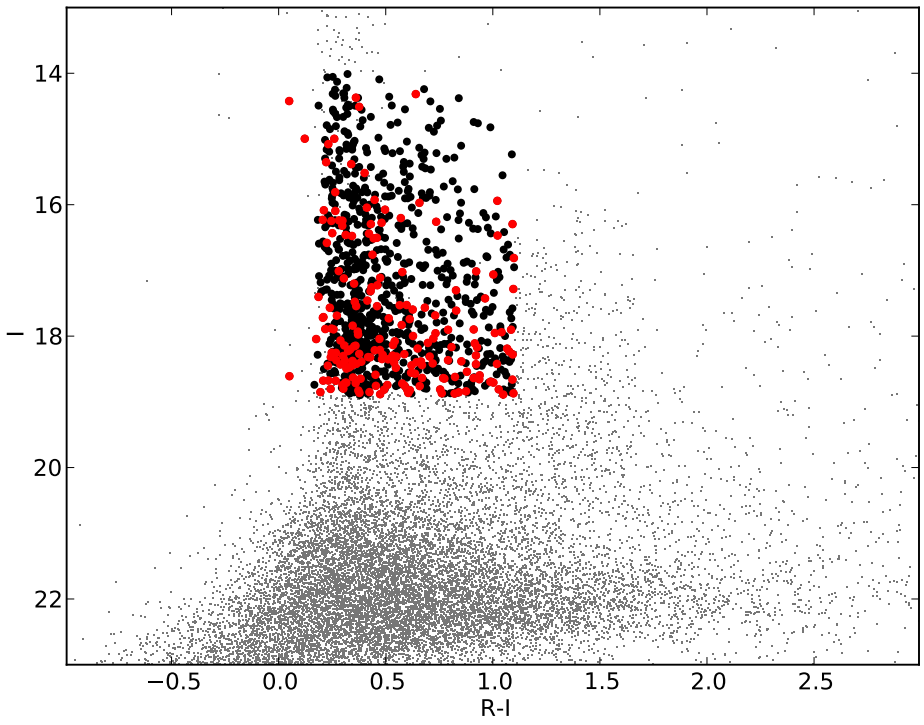

Figure A.13: A CMD of all available LMC field 15 data after filtering with DDO51, as shown in Figure 2.5. Black points are all objects that passed the DDO51 filtering, and red points are the objects returned by our metal-poor selection criteria. The filtering was only performed on objects with $0.1 < (R - I) < 1.1$, and $18.9 < I < 14$.

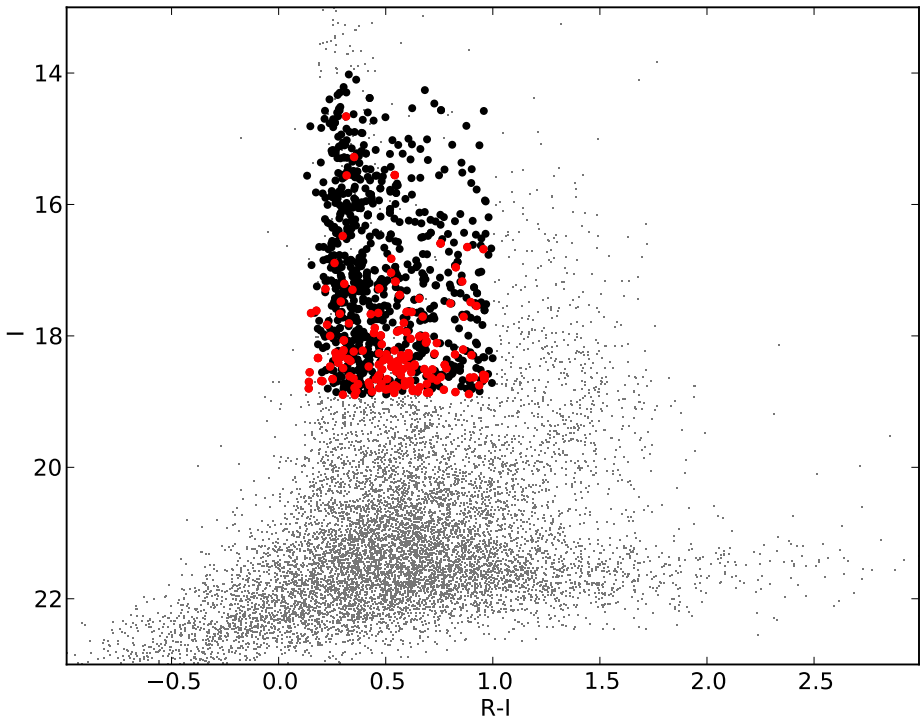

Figure A.14: A CMD of all available LMC field 11 data after filtering with DDO51, as shown in Figure 2.5. Black points are all objects that passed the DDO51 filtering, and red points are the objects returned by our metal-poor selection criteria. The filtering was only performed on objects with $0.1 < (R - I) < 1.1$, and $18.9 < I < 14$.

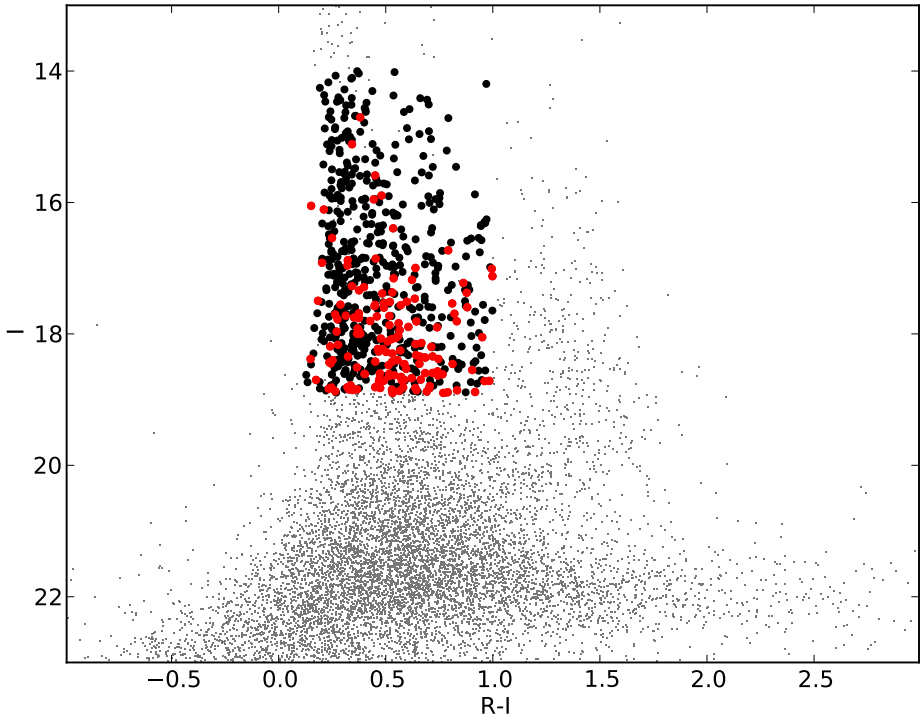

Figure A.15: A CMD of all available LMC field 8 data after filtering with DDO51, as shown in Figure 2.5. Black points are all objects that passed the DDO51 filtering, and red points are the objects returned by our metal-poor selection criteria. The filtering was only performed on objects with $0.1 < (R - I) < 1.1$, and $18.9 < I < 14$.

Appendix B

Spectroscopy: Additional Figures and Tables

B.1 Tables of MP Stars

The following are tables of the metal-poor stars, identified through the summation of the two strongest NIR Ca II triplet lines. We have listed all stars for each field with the equivalent widths below a certain threshold, which is relaxed in the outer fields, due to low numbers of LMC stars.

The magnitudes used in calculating the metallicity are either (V-V_{HB}), using primarily the Zaritsky et al. (2004) LMC photometric survey, or M_I, from our CTIO observations. Refer to the headers for which system is used, any exceptions to the system are noted.

Note, $\sum EW$ refers to the sum of the equivalent widths of the two strongest lines of the NIR Ca II triplet (8542Å and 8662Å).

Table B.1: Stars with $\sum$EW < 4 in LMC field 26 - observation 1.

ID	$\mathbf{V}_{HEL}$	$\sum EW$	V-V_{HB}	[Fe/H]	**RA**	**Dec**
	km s^{-1}	Å			deg.	deg.
7_{20}	234.8±5.0	3.96	-1.72	-1.61	81.71577917	-69.70820556
1_{40}	242.4±2.1	2.93	-1.74	-2.13	80.743625	-69.98683056
3_{23}	247.5±1.6	1.70	-1.94	-2.93	80.24459167	-69.80548889
4_{45}	264.7±2.7	3.82	-1.63	-1.53	80.34376667	-69.56726111
7_{22}	262.2±7.1	3.55	-1.83	-1.84	81.79984167	-69.78395
8_{46}	298.7±3.4	2.84	-1.91	-2.22	81.49677917	-69.53025833
*cgm*19	301.6±3.1	3.45	-2.06	-1.94	81.09175	-69.75202778

Table B.2: Stars with $\sum$EW < 4 in LMC field 26 - observation 2.

ID	$\mathbf{V}_{HEL}$	$\sum EW$	M_I	[Fe/H]	**RA**	**Dec**
	km s^{-1}	Å			deg.	deg.
4_{87}	239.6±3.1	3.75	-0.92	-1.42	80.06425	-69.636925
2_{56}	214.9±3.4	3.87	+0.10	-1.16	80.69129583	-69.83413611
7_{85}	234.5±3.0	2.34	-0.55	-2.09	81.54134167	-69.67529722
*cgm*13	264.7±2.3	3.46	*-2.19*[a]	-1.96	80.67033333	-69.86308333
*ngc*38	259.9±2.8	3.18	*-1.24*[b]	-2.01	80.35881667	-69.95503889
8_{87}	260.4±2.5	3.85	-0.74	-1.34	81.678825	-69.50028333
2_{81}	272.1±2.5	3.26	-0.75	-1.63	80.10145833	-69.87688333
8_{65}	285.4±5.1	3.43	-0.92	-1.58	81.40270833	-69.59741111
5_{79}	304.9±2.9	3.32	-0.86	-1.62	81.247125	-70.02731944
2_{51}	304.1±3.0	3.54	-1.22	-1.58	80.48095417	-69.81703889

[a] V-V_{HB} magnitude, V magnitude from Cole et al. (2005).

[b] $J - J_{tRGB}$ magnitude.

Table B.3: Stars with $\sum$EW < 4 in LMC field 26 - observation 3.

ID	$\mathbf{V}_{HEL}$	$\sum EW$	V-V_{HB}	[Fe/H]	**RA**	**Dec**
	km s^{-1}	Å			deg.	deg.
$1155 - Sz$	199.3±2.3	3.43	-2.78	-2.13	79.80668333	-70.071
2_{99}	236.5±1.4	3.98	-1.53	-1.56	80.873375	-69.92678611
4_{64}	238.5±3.0	3.72	*-1.16*[a]	-1.48	80.55395833	-69.58610833
$246 - Sz$	234.6±2.0	3.77	-2.11	-1.80	72.83761667	-66.68377778
3_{67}	224.4±0.3	3.74	-0.64	-1.44	80.89366667	-69.7938
$636 - Sz$	257.3±4.2	3.28	-2.96	-2.25	81.6692	-70.52192778
1_{95}	240.7±1.4	2.91	-0.82	-1.92	80.51539167	-70.07503333
1_{37}	240.0±1.8	2.33	-1.77	-2.47	80.67133333	-70.06971111
$ngc31$	259.9±2.5	2.56	*-3.47*[a]	-2.54	80.3425125	-69.95204167
$ngc37$	259.6±2.8	3.29	*-1.79*[a]	-1.82	80.3592	-69.94283333
3_{89}	253.1±3.5	3.62	-0.56	-1.49	80.56979167	-69.78492222
$777 - Sz$	263.7±2.7	3.98	*-3.34*[a]	-1.79	78.39390417	-69.30423611
4_{97}	262.3±2.9	2.25	-1.58	-2.47	80.53413333	-69.61342222
$1107 - Sz$	249.3±2.0	2.77	-2.77	-2.46	80.64054167	-69.00909444
$1278 - Sz$	246.2±2.4	3.22	-3.41	-2.39	80.96734167	-69.42678056
$996 - Sz$	309.5±7.1	3.83	-3.12	-2.03	82.20256667	-69.83586944
$897 - Sz$	301.2±2.4	3.84	-3.48	-2.12	79.77772917	-70.46395833
8_{60}	305.8±2.7	3.71	-1.35	-1.64	80.95258333	-69.64394444
$447 - Sz$	336.3±2.5	3.89	-2.73	-1.91	81.576125	-70.23481111
5_{82}	229.1±0.7	2.1[†]	-1.12	-2.5	81.42866667	-70.07773889

[a] I magnitude used.

[†] Hand-measured in IRAF, not picked up by automatic routine.

Table B.4: Stars with $\sum$EW < 4 in LMC field 25 - observation 1.

ID	$\mathbf{V}_{HEL}$	$\sum EW$	V-V_{HB}	[Fe/H]	**RA**	**Dec**
	km s^{-1}	Å			deg.	deg.
2_{29}	196.1±1.3	2.24	-1.36	-2.43	78.88388333	-68.61231111
5_{40}	236.0±2.2	3.86	-1.25	-1.54	79.45187917	-68.78643056
3_{18}	227.5±2.9	3.64	-1.13	-1.62	79.16069583	-68.37823611
3_{10}	222.7±1.4	2.44	-1.53	-2.35	78.86254167	-68.38204167
4_{16}	238.4±2.8	3.64	-1.42	-1.69	78.98137917	-68.30273333
4_{5}	229.5±2.4	3.69	-2.55	-1.95	79.2833625	-68.20621389
6_{30}	259.1±5.8	3.94	-1.36	-1.53	79.76925417	-68.52238611
5_{20}	251.9±2.0	2.87	-1.63	-2.13	79.563725	-68.7471
6_{22}	288.9±3.6	4.00	-1.53	-1.55	79.63940417	-68.54972778
5_{15}	277.9±2.5	2.41	-1.57	-2.38	80.10868333	-68.64505
6_{5}	277.1±2.3	3.67	-2.64	-1.98	79.35690417	-68.49156944
6_{12}	283.9±2.1	2.46	-1.95	-2.43	79.76059583	-68.59452222
2_{12}	274.5±2.6	3.82	-2.30	-1.83	79.11425	-68.53266389
$840 - Sz$	295.1±5.1	3.72	-2.29	-1.87	80.92086667	-67.94127778
8_{4}	295.3±2.6	3.80	-2.66	-1.93	80.0859125	-68.27439167
4_{36}	329.3±0.0	2.0†	-0.77	-2.5	78.9665375	-68.24855
8_{28}	328.6±3.0	3.2†	-1.39	-1.9	79.652225	-68.29254167

† Hand-measured in IRAF, not picked up by automatic routine.

Table B.5: Stars with $\sum$EW < 4 in LMC field 25 - observation 2.

ID	$\mathbf{V}_{HEL}$	$\sum EW$	V-V_{HB}	[Fe/H]	**RA**	**Dec**
	km s^{-1}	Å			deg.	deg.
1_{88}	192.4±2.3	3.09	-0.79	-1.81	79.214125	-68.73783333
5_{66}	239.6±0.2	3.0	-1.15	-1.95	79.73841667	-68.73536389
1_{47}	226.5±2.5	3.62	-1.11	-1.62	78.61583333	-68.707925
3_{62}	224.9±1.7	2.81	-0.54	-1.91	78.93439167	-68.37500833
7_{48}	237.0±2.7	3.98	-1.27	-1.49	79.60933333	-68.43308889
7_{53}	222.1±2.4	3.41	-0.66	-1.62	79.93408333	-68.33446111
$684 - Sz$	257.0±2.0	2.93	-2.56	-2.32	77.5740125	-68.39771944
2_{71}	265.8±3.6	3.86	-0.64	-1.39	78.87241667	-68.59344167
8_{5}	243.1±2.0	3.72	-2.68	-1.97	79.43477083	-68.22926389
8_{50}	252.3±3.8	3.35	-0.42	-1.59	79.95420833	-68.24261944
8_{38}	243.3±3.0	3.63	-1.04	-1.60	79.68258333	-68.19085278
5_{51}	287.7±2.6	2.97	-1.08	-1.95	79.5702	-68.72778333
2_{80}	279.3±0.3	3.58	-1.11	-1.64	78.84808333	-68.62216944
2_{54}	280.9±0.5	2.17	-0.77	-2.34	78.52710417	-68.62089722
4_{48}	303.7±3.0	3.86	-0.45	-1.34	79.238	-68.26545833
8_{48}	301.8±2.5	2.96	-0.77	-1.88	79.71004167	-68.27998056
4_{8}	343.7±2.2	2.52	-1.90	-2.39	79.03309583	-68.28346667
6_{16}	372.4±3.3	3.83	-1.76	-1.68	80.06760417	-68.61836111
2_{79}	262.7±0.6	2.4†	-0.65	-2.2	78.95541667	-68.58128333
2_{74}	282.3±1.9	3.3†	-0.64	-1.7	78.95541667	-68.58128333

† Hand-measured in IRAF, not picked up by automatic routine.

Table B.6: Stars with $\sum$EW < 4 in LMC field 24.

ID	$\mathbf{V}_{HEL}$	$\sum EW$	V-V_{HB}	[Fe/H]	**RA**	**Dec**
	km s^{-1}	Å			deg.	deg.
4_{33}	186.3±3.8	3.55	-1.13	-1.66	76.2075	-67.84931389
2_{24}	239.9±2.8	3.16	-1.24	-1.89	76.21415417	-68.30559444
5_{9}	254.3±2.3	2.45	-1.58	-2.35	77.45242917	-68.35164722
2_{11}	241.9±3.9	3.77	-1.51	-1.65	76.62582083	-68.26502222
1_{31}	263.4±2.9	3.08	-1.86	-2.08	76.188475	-68.32318056
2_{28}	265.9±3.1	3.40	-1.26	-1.77	76.4223625	-68.19638056
2_{31}	247.2±3.2	3.57	-1.19	-1.67	76.62154167	-68.22419722
2_{13}	288.4±2.5	3.71	-1.67	-1.72	76.3119	-68.30215556
4_{4}	290.0±2.2	3.55	-2.21	-1.93	76.37748333	-67.93956111
4_{25}	280.1±2.8	3.64	-2.84	-1.28	76.411775	-67.99139444
7_{17}	273.0±2.6	3.60	-3.45	-1.58	77.0637375	-68.00995

Table B.7: Stars with $\sum$EW < 4 in LMC field 20.

ID	$\mathbf{V}_{HEL}$	$\sum EW$	M_I	[Fe/H]	**RA**	**Dec**
	km s^{-1}	Å			deg.	deg.
3_1	219.5±2.3	3.41	-1.25	-1.65	69.411875	-67.41552778
4_4	210.8±4.1	3.99	-0.69	-1.26	69.613625	-67.19459167
4_1	252.5±2.5	2.19	-2.27	-2.52	69.0176875	-67.26973611
2_2	286.6±2.5	3.58	-1.13	-1.55	69.588175	-67.45300278
2_8	283.5±2.7	3.72	-0.97	-1.45	69.33513333	-67.55558889
7_5	286.4±2.5	3.73	-1.87	-1.62	69.993875	-67.31118056
7_9	279.2±3.8	3.63	-2.05	-1.70	69.81374167	-67.33602222
5_5	313.2±1.3	2.64	*-1.30*[a]	-2.18	70.0211125	-67.70678611
3_7	279.9±2.3	2.1[†]	-2.0	-2.5	69.26322917	-67.31796944

[a] V-V_{HB} magnitude, V magnitude from (Zaritsky et al. 2004).

[†] Hand-measured in IRAF, not picked up by automatic routine.

Table B.8: Stars with $\sum$EW < 4 in LMC field 15.

ID	$\mathbf{V}_{HEL}$	$\sum EW$	M_I	[Fe/H]	**RA**	**Dec**
	km s^{-1}	Å			deg.	deg.
8_{26}	205.4±3.0	3.41	-2.42	-1.75	63.27589583	-66.13116389
5_{17}	253.3±2.2	2.99	-2.57	-2.13	62.57295833	-66.56230278
1_{20}	260.4±2.7	3.34	-5.35	-2.50	62.32884583	-66.55605278
7_2	255.7±3.9	3.83	-1.75	-1.55	63.17099583	-66.207275
8_{23}	368.6±2.9	3.46	-1.96	-1.77	62.7452875	-66.06399444
7_9	266.4±1.7	1.9[†]	-1.95	-2.6	63.105	-66.228025

[†] Hand-measured in IRAF, not picked up by automatic routine.

Table B.9: Stars with $\sum$EW < 4 in LMC field 13.

ID	$\mathbf{V}_{HEL}$	$\sum EW$	M_I	[Fe/H]	**RA**	**Dec**
	km s^{-1}	Å			deg.	deg.
4_8	188.8±2.8	2.97	-3.27	-2.28	64.84802083	-64.59836667
3_5	233.1±2.2	3.43	-3.08	-2.01	65.17905	-64.80896111
5_3	247.3±2.1	2.7	-4.63	-2.69	65.9377375	-65.11655278

Table B.10: Stars with $\sum$EW < 5.5 in LMC field 11.

ID	$\mathbf{V}_{HEL}$	$\sum EW$	J-J_{tRGB}	[Fe/H]	**RA**	**Dec**
	km s^{-1}	Å			deg.	deg.
$137-2M$	172.5±3.3	4.5	+1.87	-0.94	60.76713333	-65.70098056
$22-2M$	219.8±2.3	5.32	+1.83	-0.58	60.1097125	-65.14153333

Table B.11: Stars with $\sum$EW < 5.5 in LMC field 8.

ID	$\mathbf{V}_{HEL}$	$\sum EW$	M_I	[Fe/H]	**RA**	**Dec**
	km s^{-1}	Å			deg.	deg.
$158-2M$	217.7±2.2	5.21	*+1.83*[a]	-0.65	60.1097125	-65.14153333
6_{16}	245.2±0.5	∼2.5[†]	-0.41	-2.0	60.2784625	-64.35233889

[a] $J - J_{tRGB}$ Magnitude. Also measured in LMC field 11.

[†] Hand-measured in IRAF, not picked up by automatic routine.

B.2 Spectra of Metal-Poor Stars

The following spectra are of the stars from the Tables B.1 to B.11, focussing on the calcium triplet. The spectra are ordered such that each spectrum is in the same order as in the above tables. The star IDs will be listed in the figures with the derived metallicities.

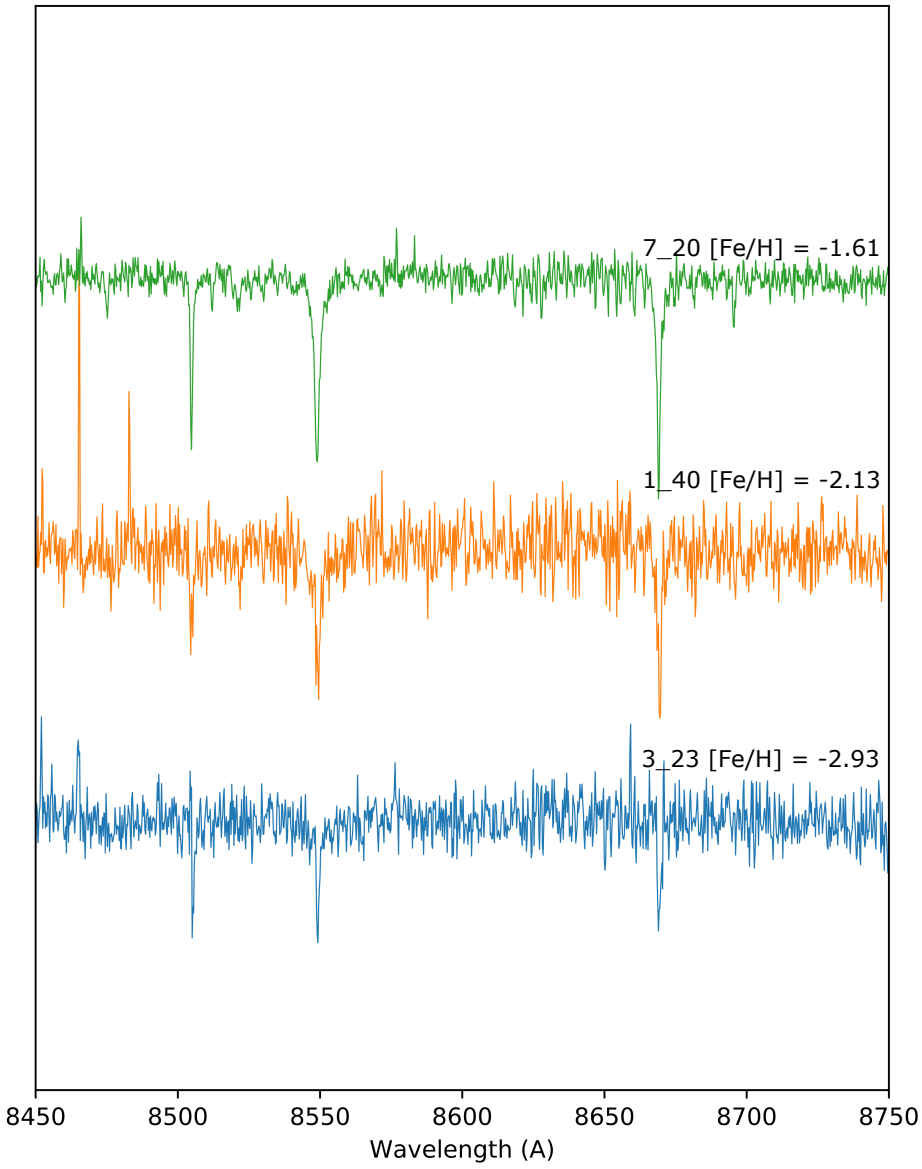

Figure B.1: Normalised spectra for metal-poor candidates in LMC field 26. From top to bottom: 7_{20}, 1_{40}, and 3_{23}. Summary in Table B.1.

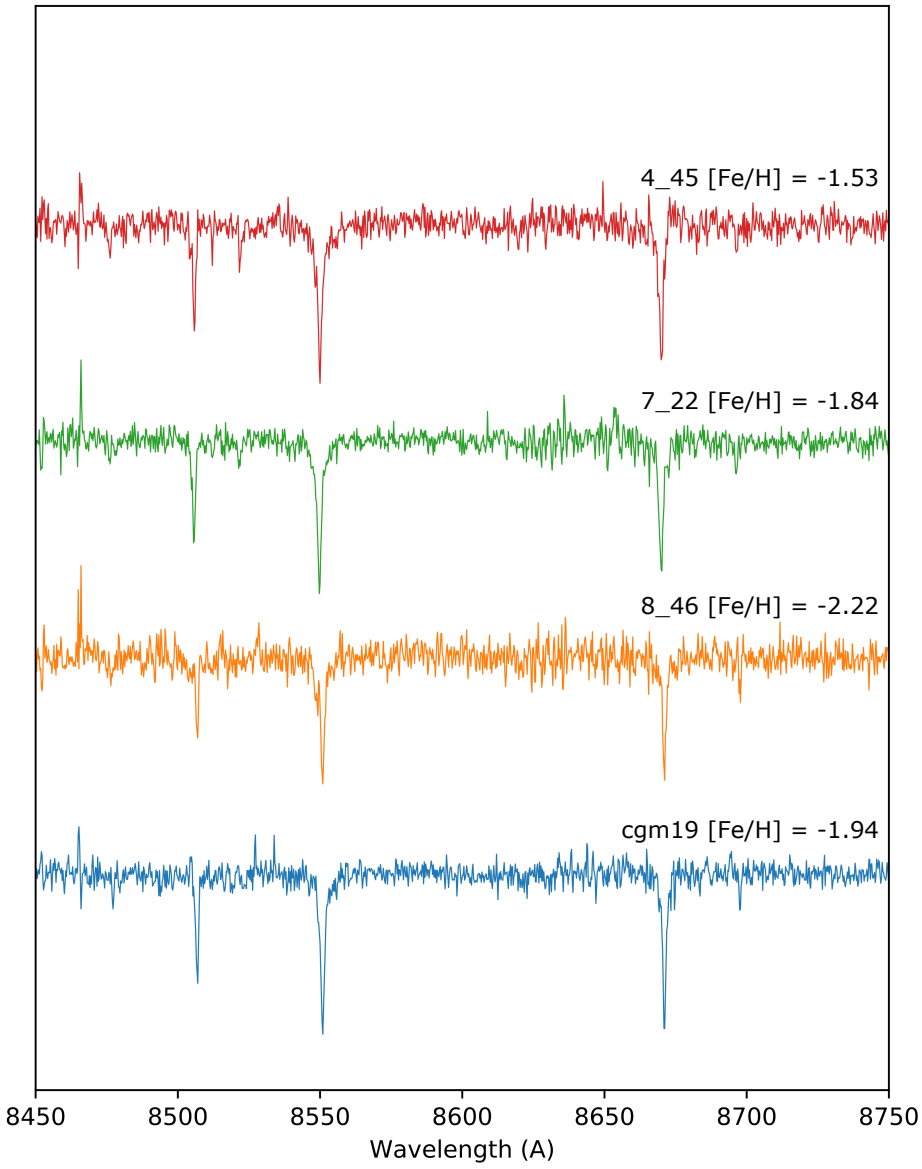

Figure B.2: Normalised spectra for metal-poor candidates in LMC field 26. From top to bottom: 4_{45}, 7_{22}, 8_{46}, and *cgm*19. Summary in Table B.1.

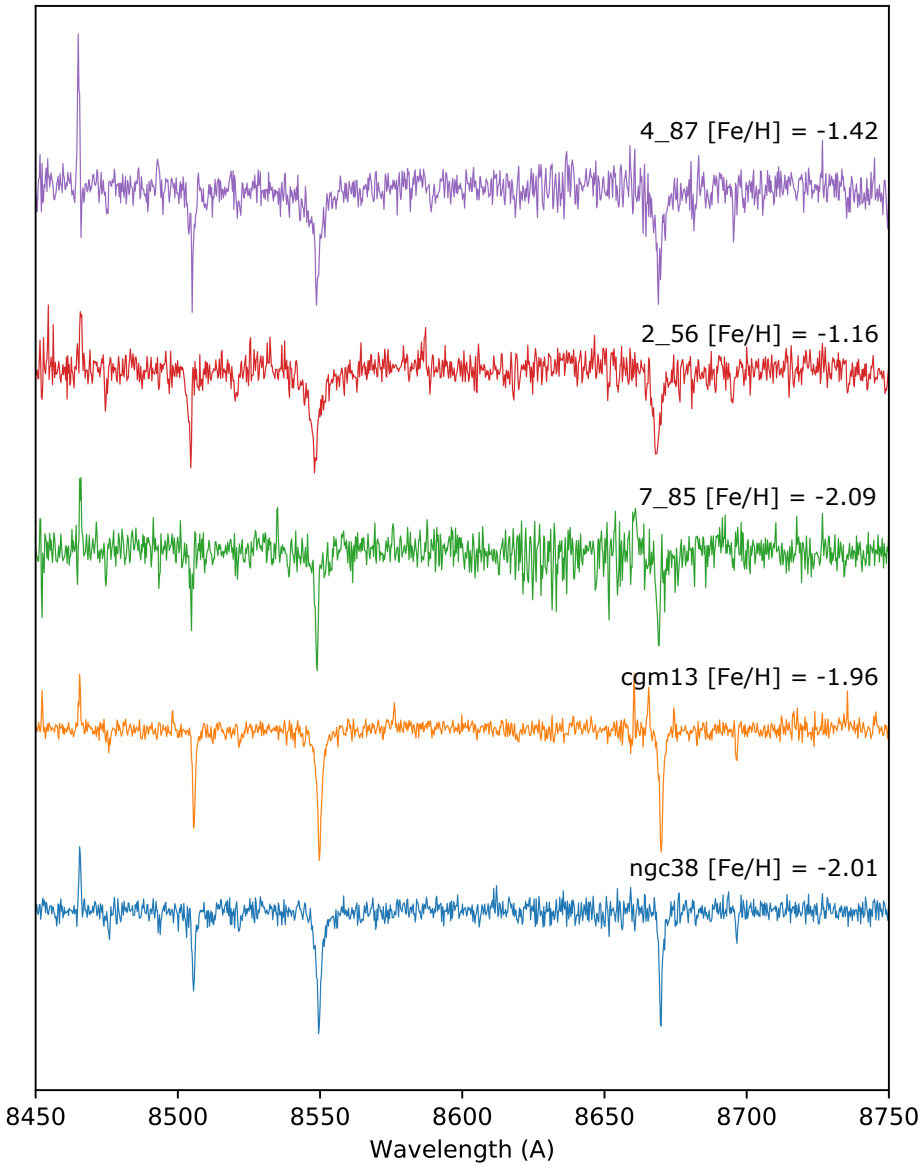

Figure B.3: Normalised spectra for metal-poor candidates in LMC field 26. From top to bottom: 4_{87}, 2_{56}, 7_{85}, $cgm13$, and $ngc38$. Summary in Table B.2.

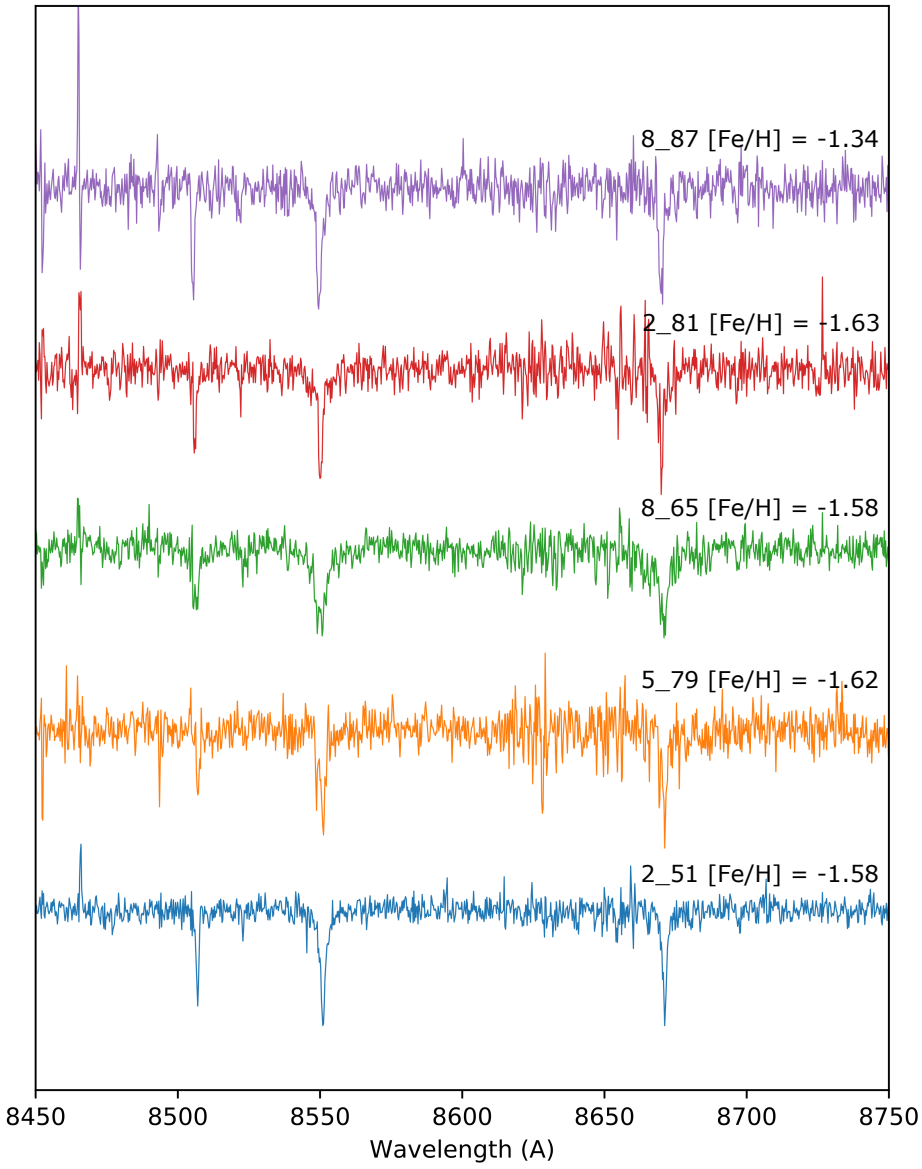

Figure B.4: Normalised spectra for metal-poor candidates in LMC field 26. From top to bottom: 8_{87}, 2_{81}, 8_{65}, 5_{79}, and 2_{51}. Summary in Table B.2.

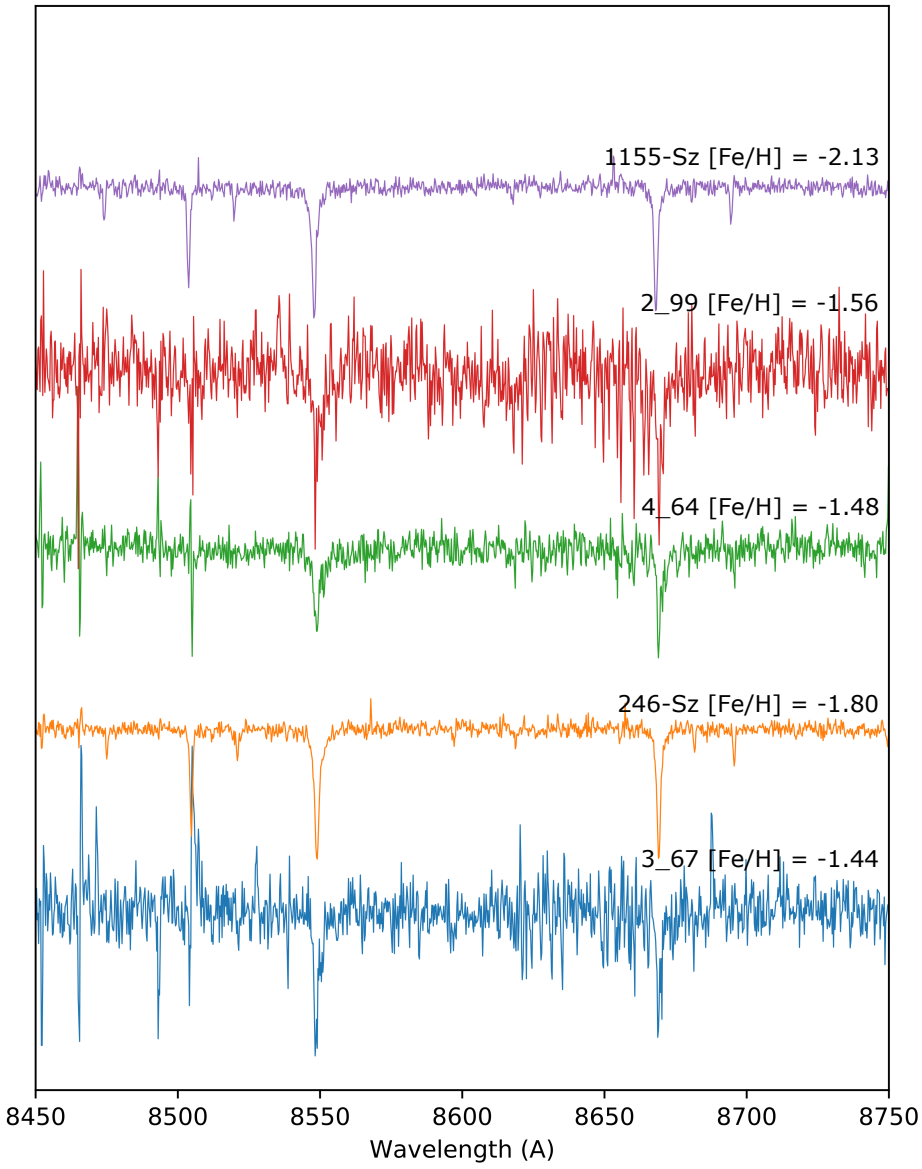

Figure B.5: Normalised spectra for metal-poor candidates in LMC field 26. From top to bottom: $1155 - Sz$, 2_{99}, 4_{64}, $246 - Sz$, and 3_{67}. Summary in Table B.3.

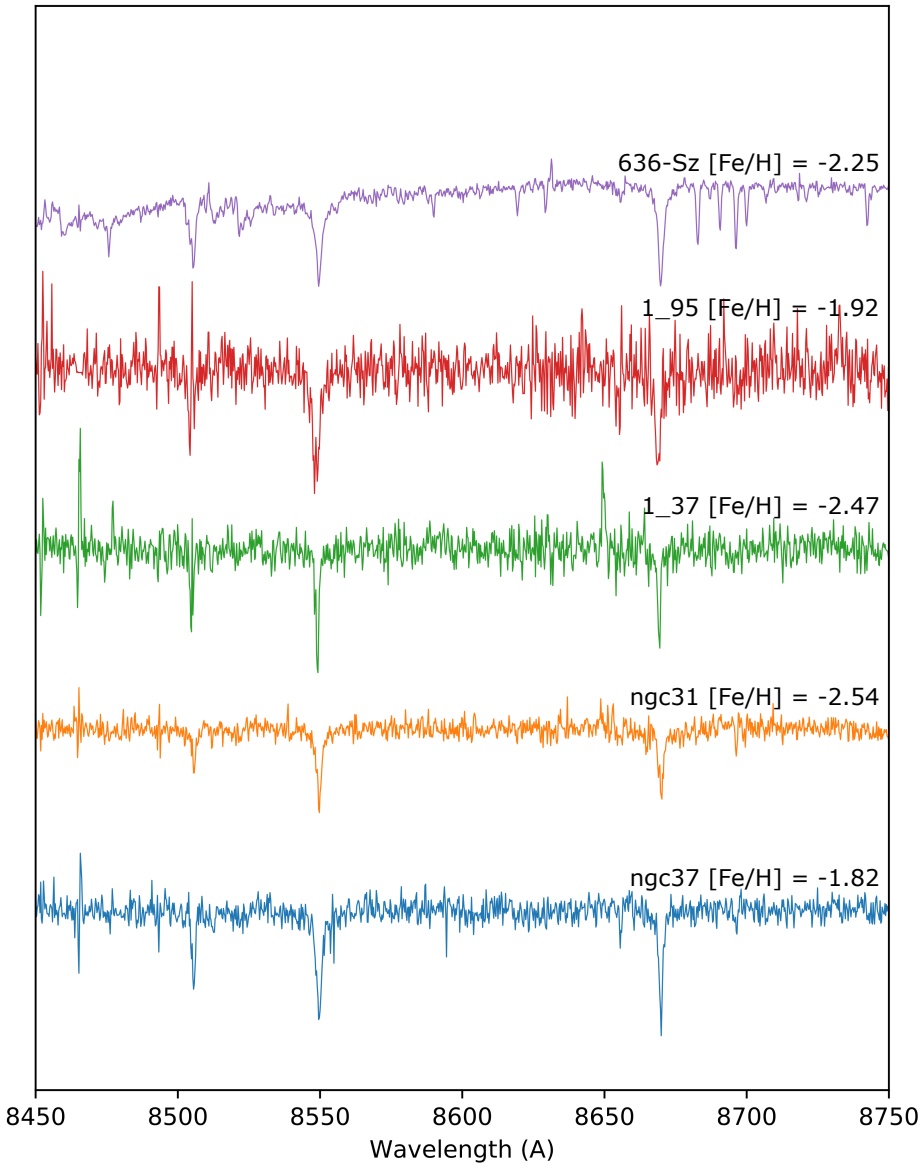

Figure B.6: Normalised spectra for metal-poor candidates in LMC field 26. From top to bottom: $636 - Sz$, 1_{95}, 1_{37}, $ngc31$, and $ngc37$. Summary in Table B.3.

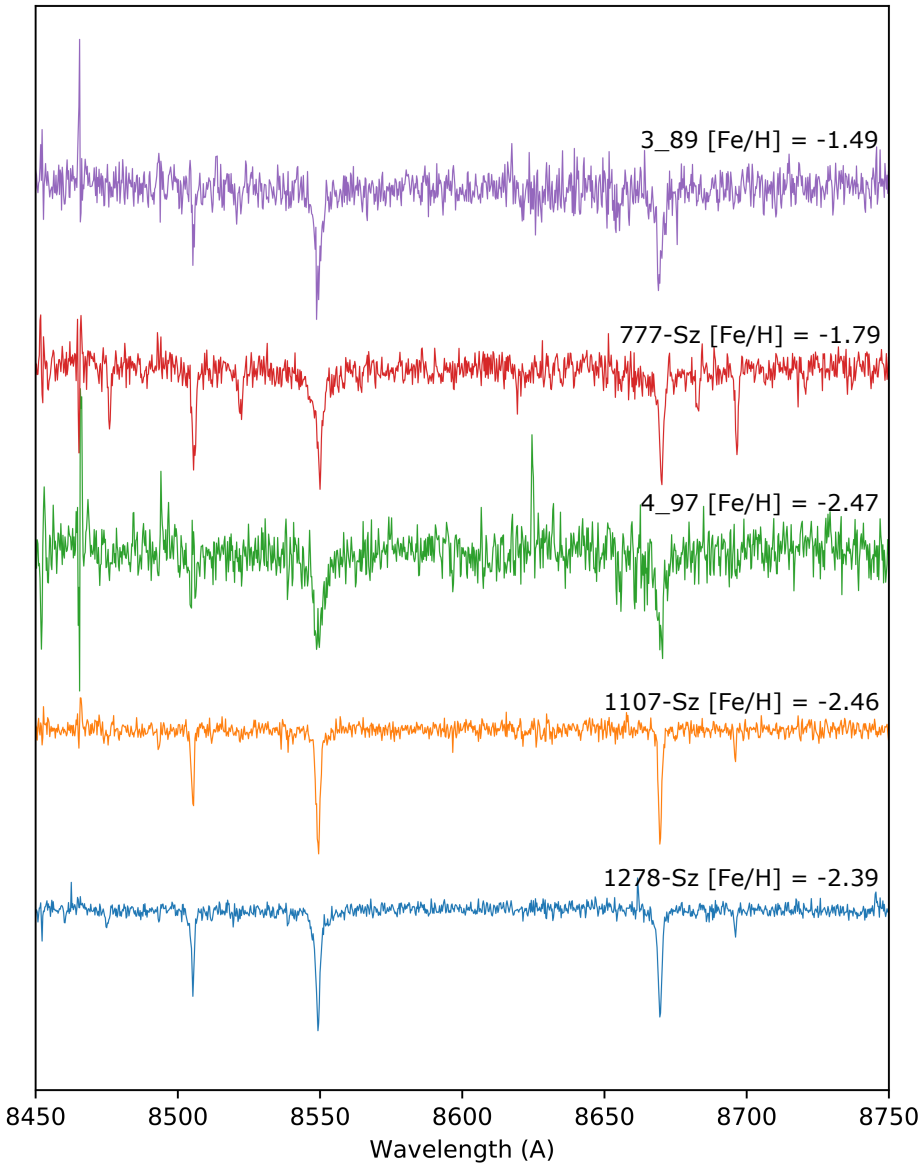

Figure B.7: Normalised spectra for metal-poor candidates in LMC field 26. From top to bottom: 3_{89}, $777-Sz$, 4_{97}, $1107-Sz$, and $1278-Sz$. Summary in Table B.3.

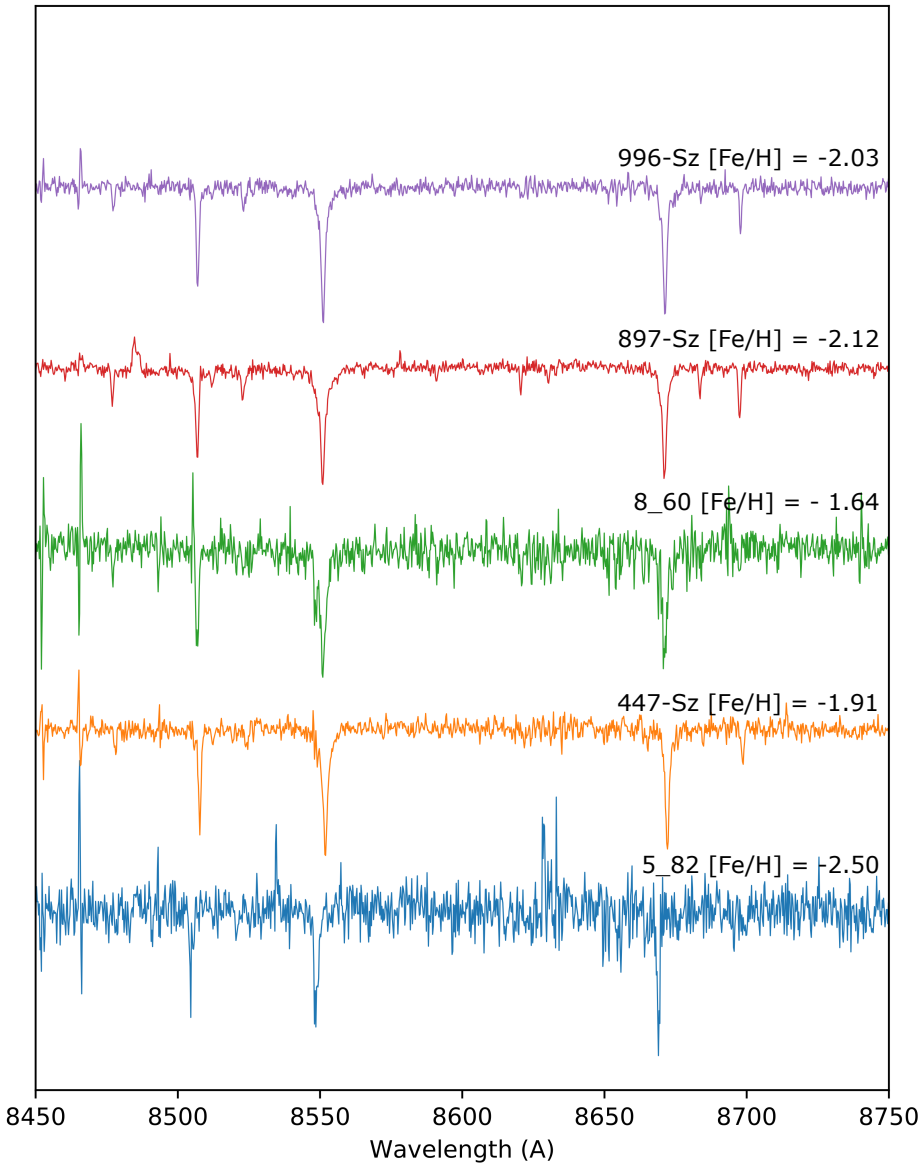

Figure B.8: Normalised spectra for metal-poor candidates in LMC field 26. From top to bottom: $996-Sz$, $897-Sz$, 8_{60}, $447-Sz$, and 5_{82}. Summary in Table B.3.

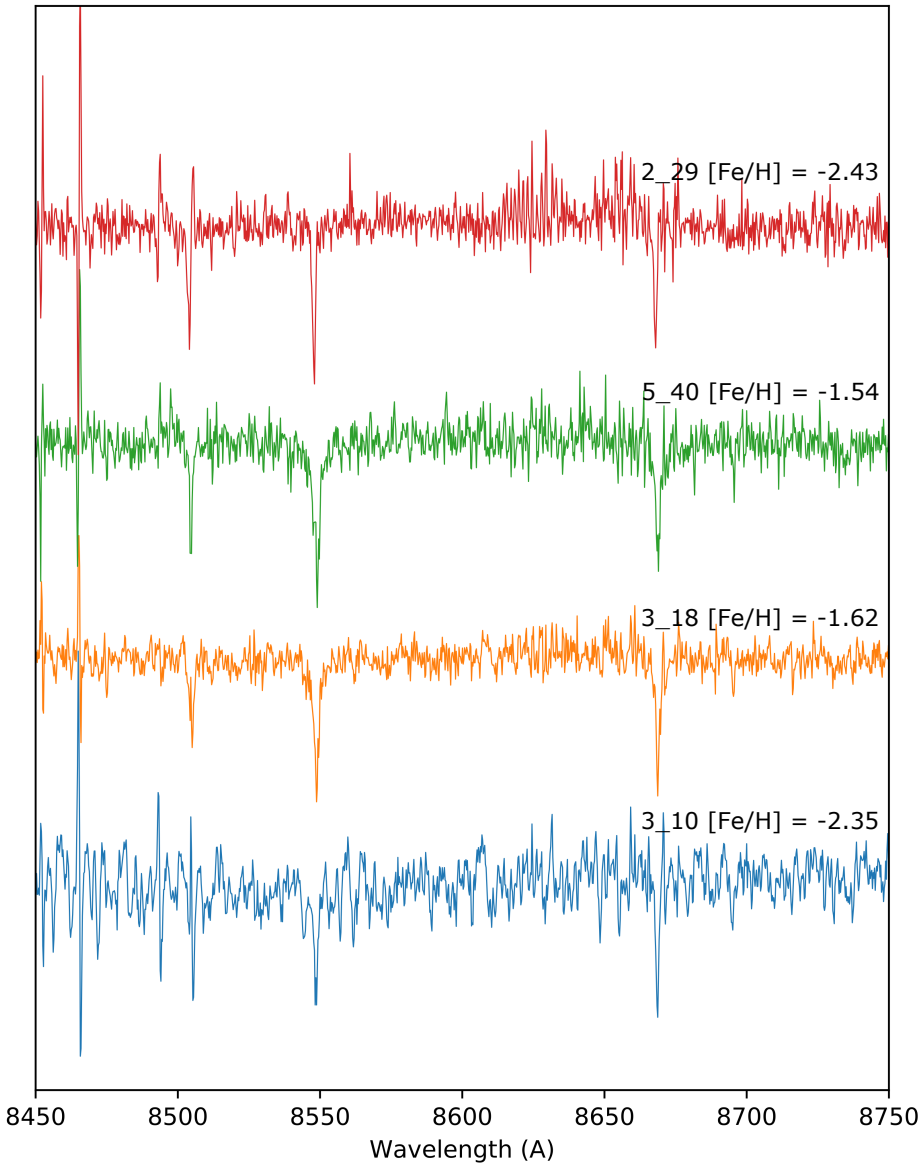

Figure B.9: Normalised spectra for metal-poor candidates in LMC field 25. From top to bottom: 2_{29}, 5_{40}, 3_{18}, and 3_{10}. Summary in Table B.4.

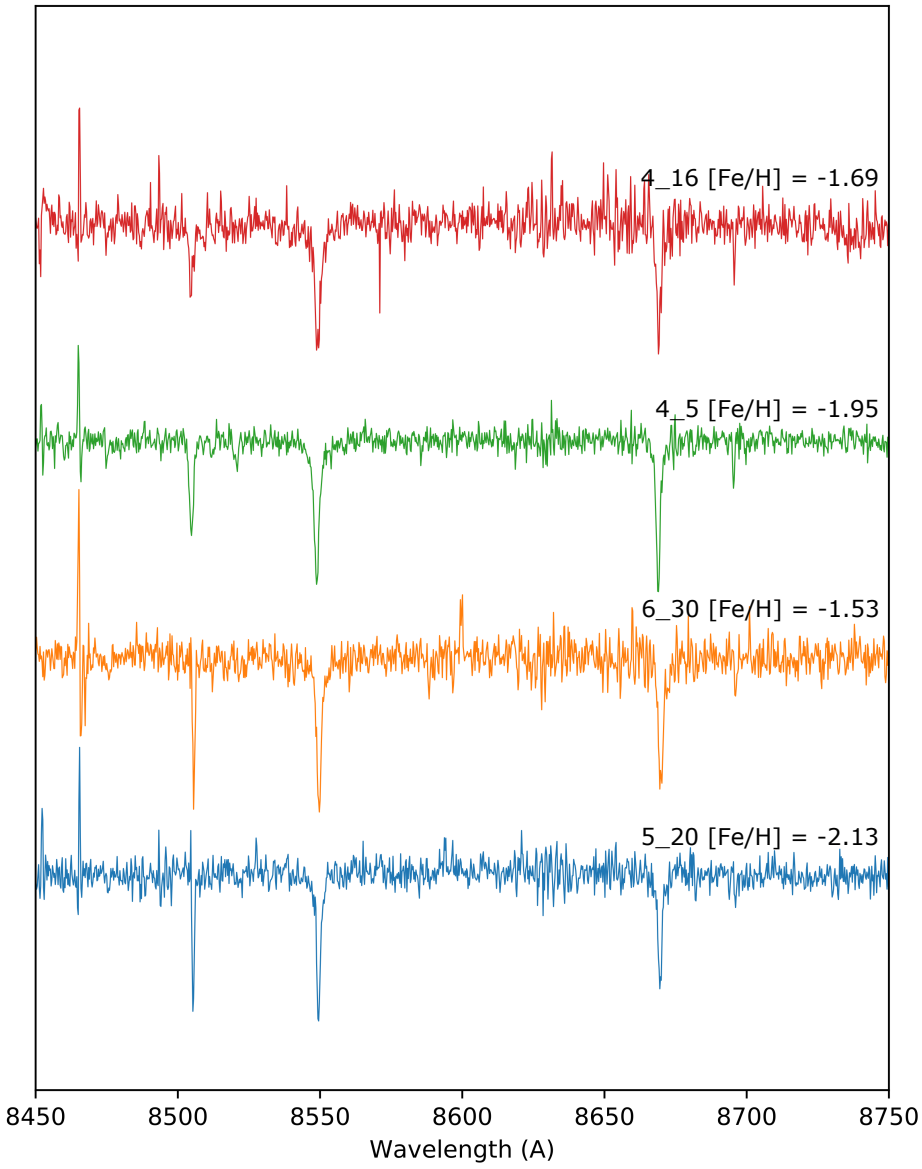

Figure B.10: Normalised spectra for metal-poor candidates in LMC field 25. From top to bottom: 4_{16}, 4_5, 6_{30}, and 5_{20}. Summary in Table B.4.

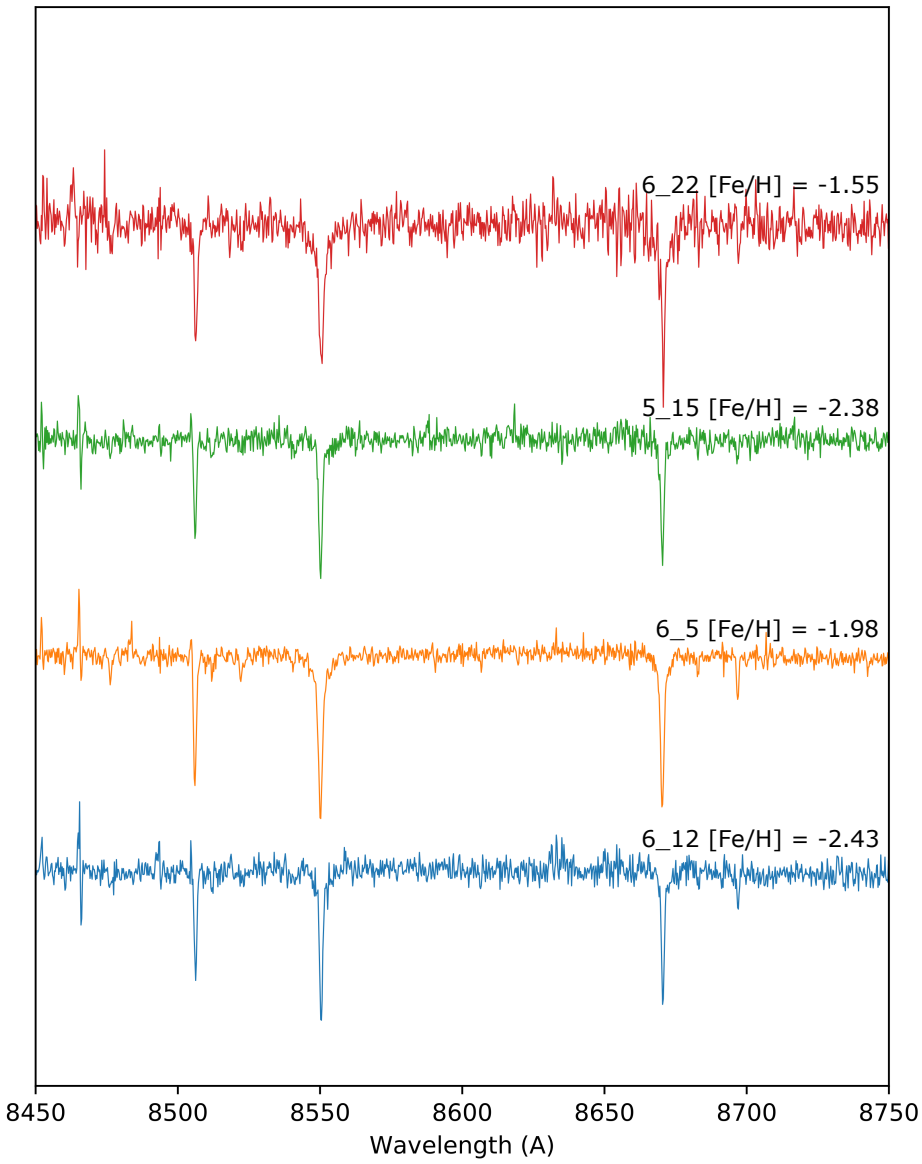

Figure B.11: Normalised spectra for metal-poor candidates in LMC field 25. From top to bottom: 6_{22}, 5_{15}, 6_5, and 6_{12}. Summary in Table B.4.

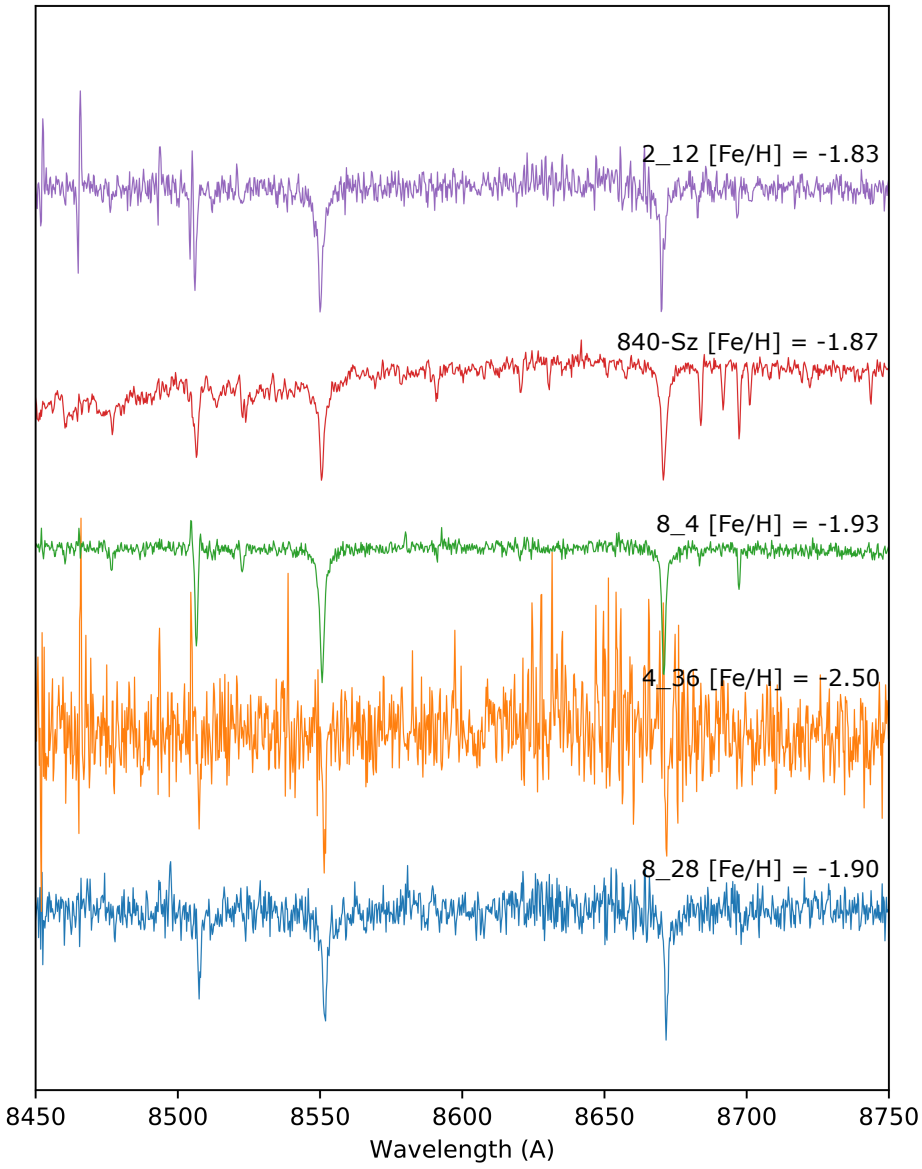

Figure B.12: Normalised spectra for metal-poor candidates in LMC field 25. From top to bottom: 2_{12}, $840-Sz$, 8_4, 4_{36}, and 8_{28}. Summary in Table B.4.

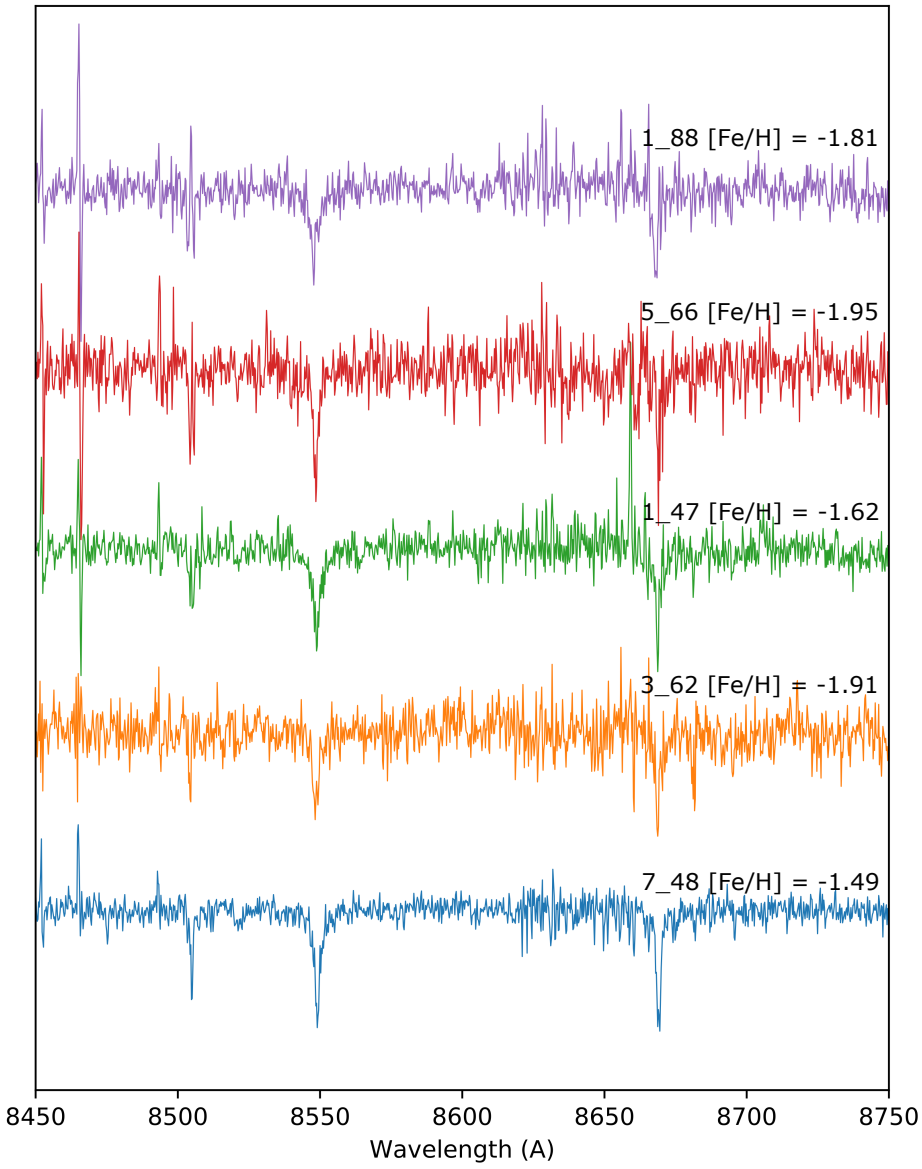

Figure B.13: Normalised spectra for metal-poor candidates in LMC field 25. From top to bottom: 1_{88}, 5_{66}, 1_{47}, 3_{62}, and 7_{48}. Summary in Table B.5.

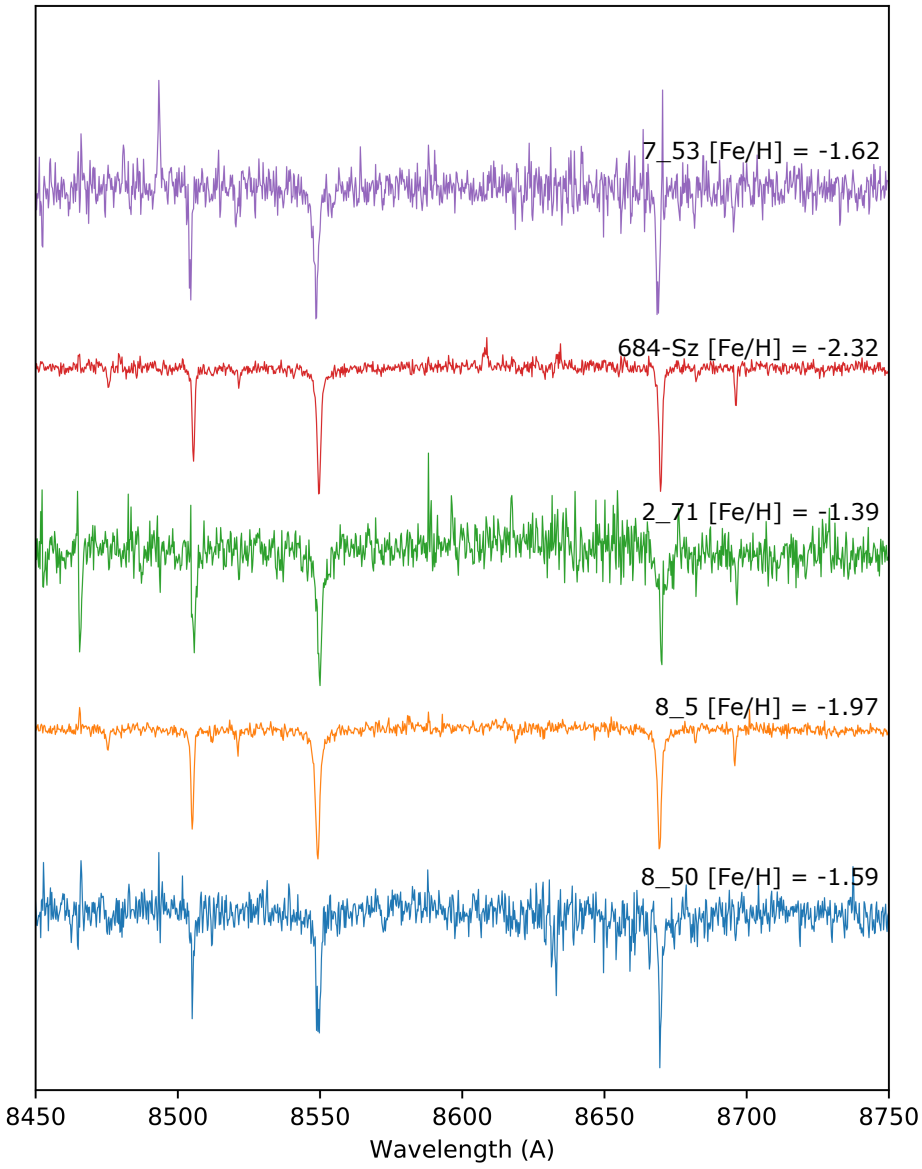

Figure B.14: Normalised spectra for metal-poor candidates in LMC field 25. From top to bottom: 7_{53}, $684 - Sz$, 2_{71}, 8_5, and 8_{50}. Summary in Table B.5.

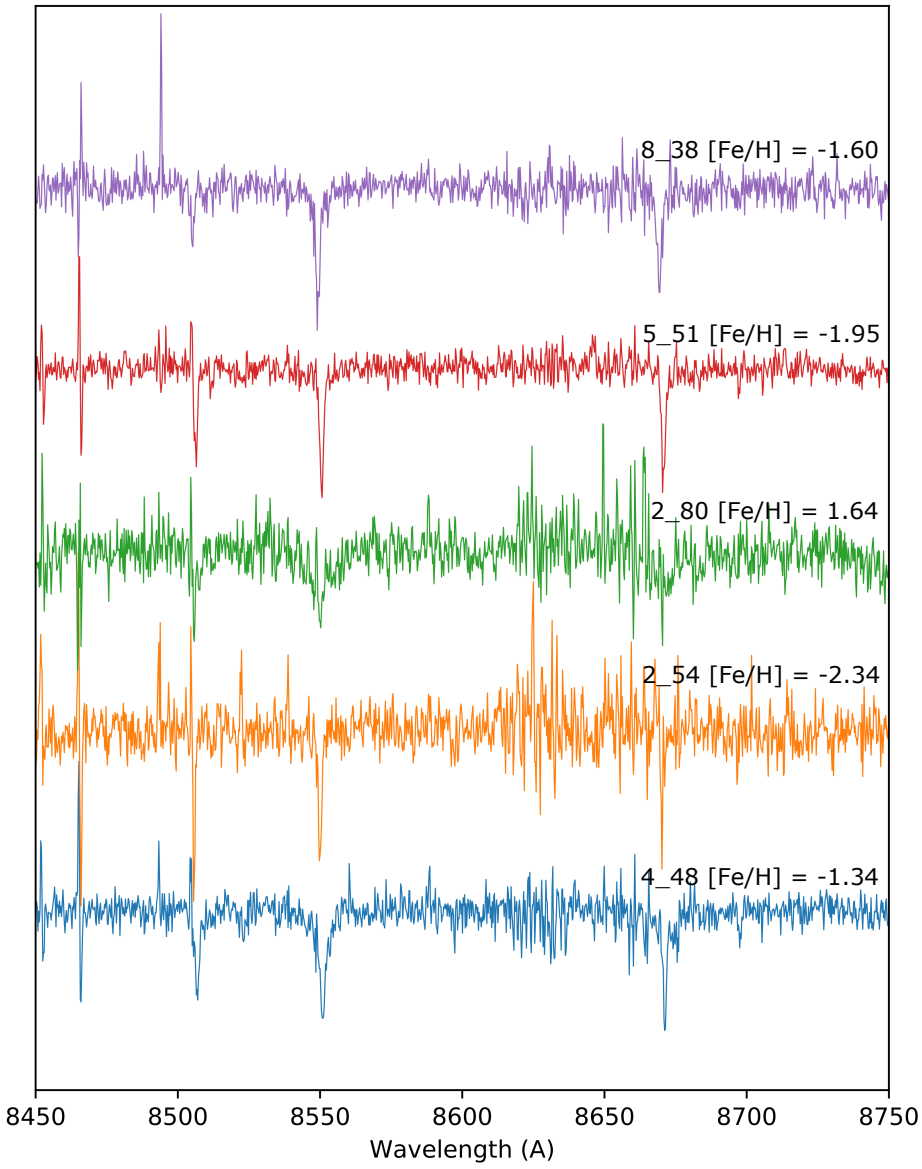

Figure B.15: Normalised spectra for metal-poor candidates in LMC field 25. From top to bottom: 8_{38}, 5_{51}, 2_{80}, 2_{54}, and 4_{48}. Summary in Table B.5.

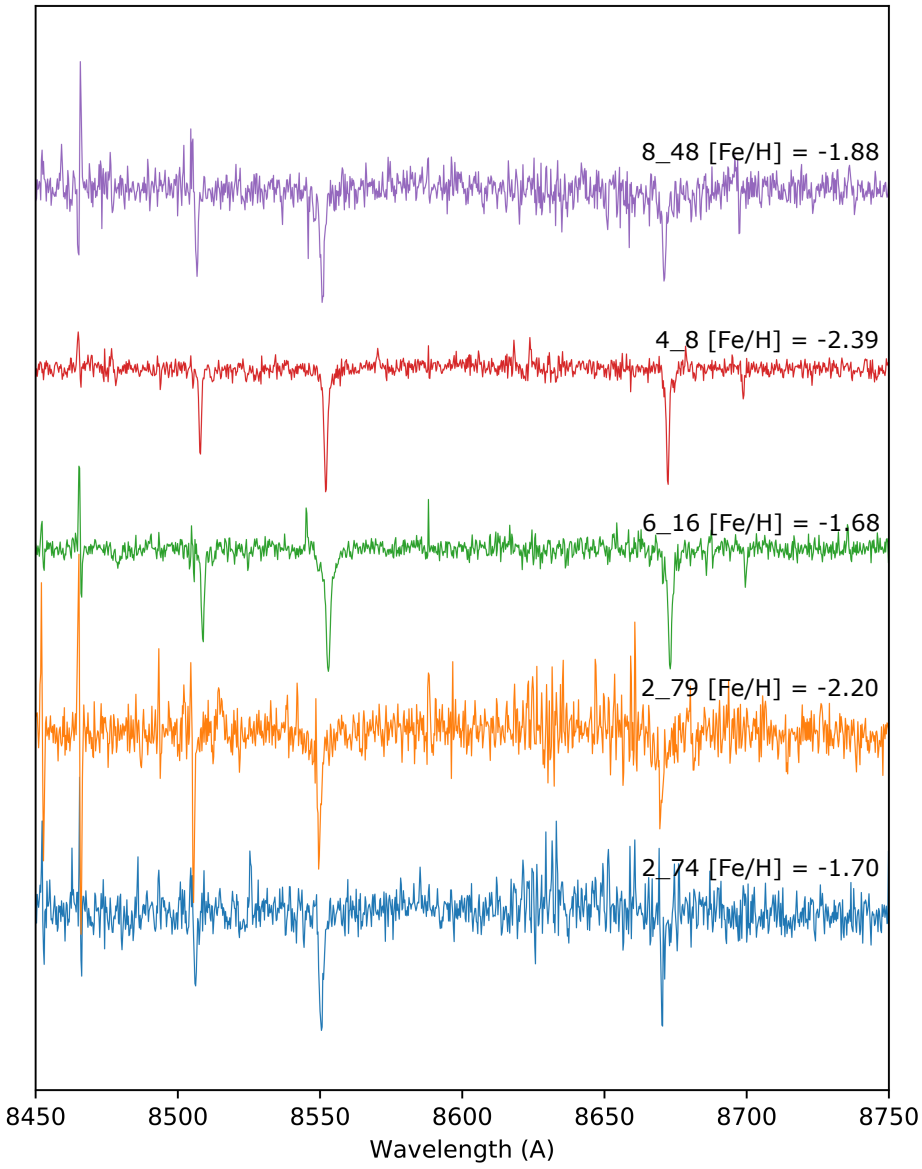

Figure B.16: Normalised spectra for metal-poor candidates in LMC field 25. From top to bottom: 8_{48}, 4_{8}, 6_{16}, 2_{79}, and 2_{74}. Summary in Table B.5.

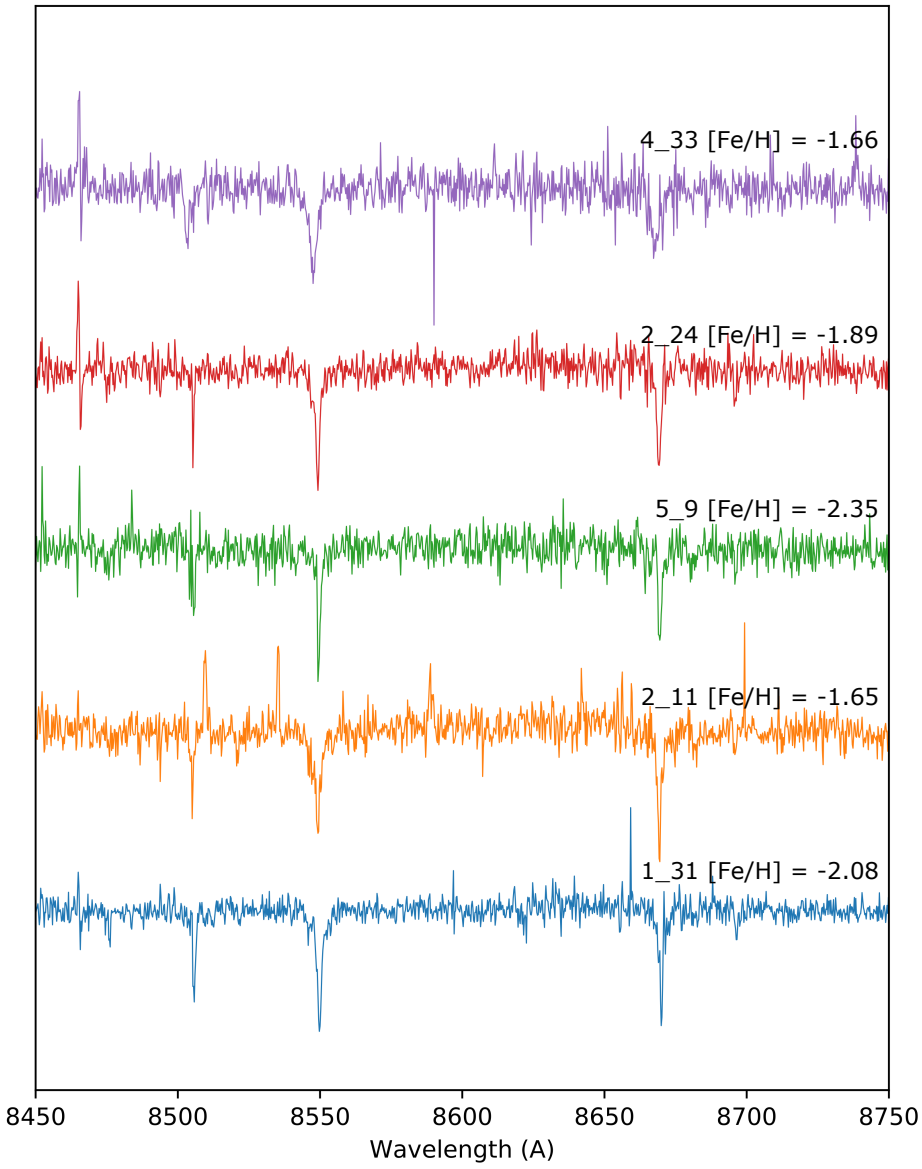

Figure B.17: Normalised spectra for metal-poor candidates in LMC field 24. From top to bottom: 4_{33}, 2_{24}, 5_9, 2_{11}, and 1_{31}. Summary in Table B.6.

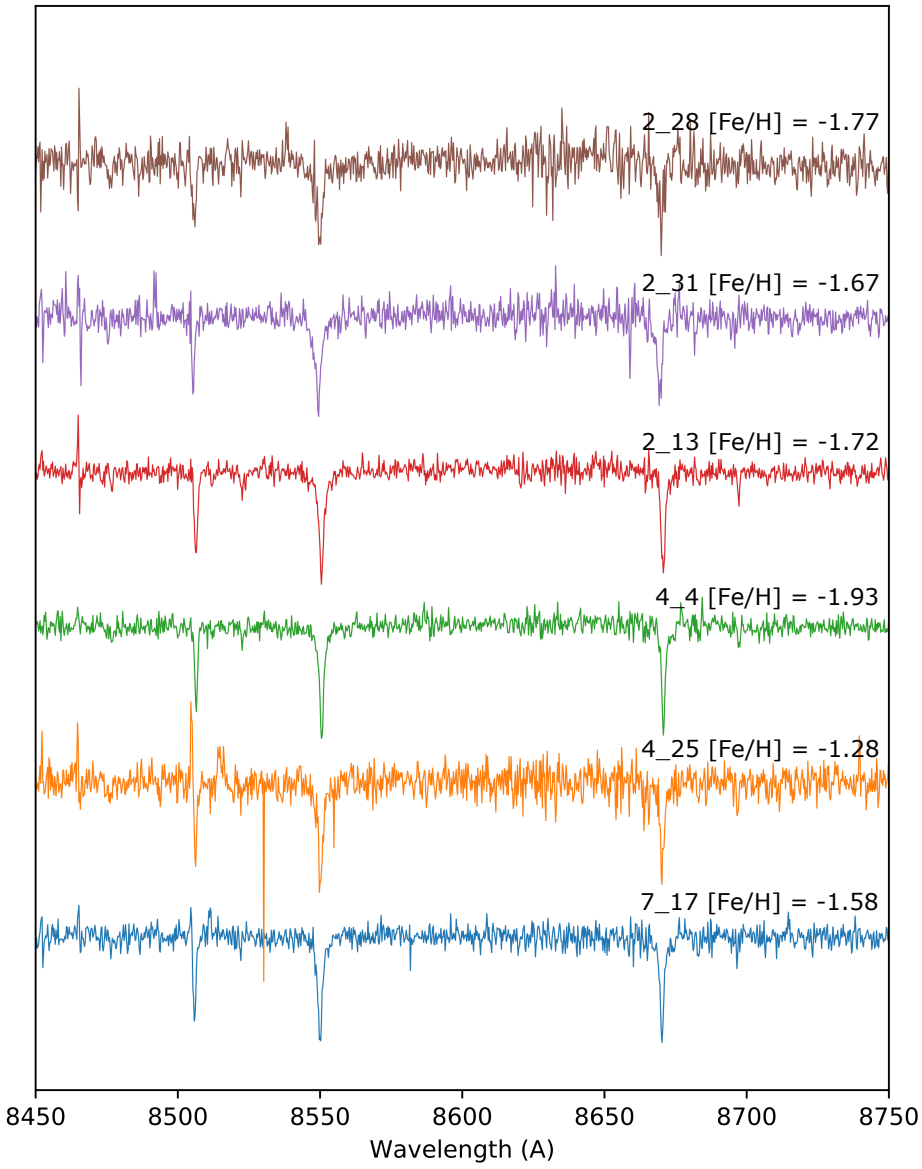

Figure B.18: Normalised spectra for metal-poor candidates in LMC field 24. From top to bottom: 2_{28}, 2_{31}, 2_{13}, 4_4, 4_{25}, and 7_{17}. Summary in Table B.6.

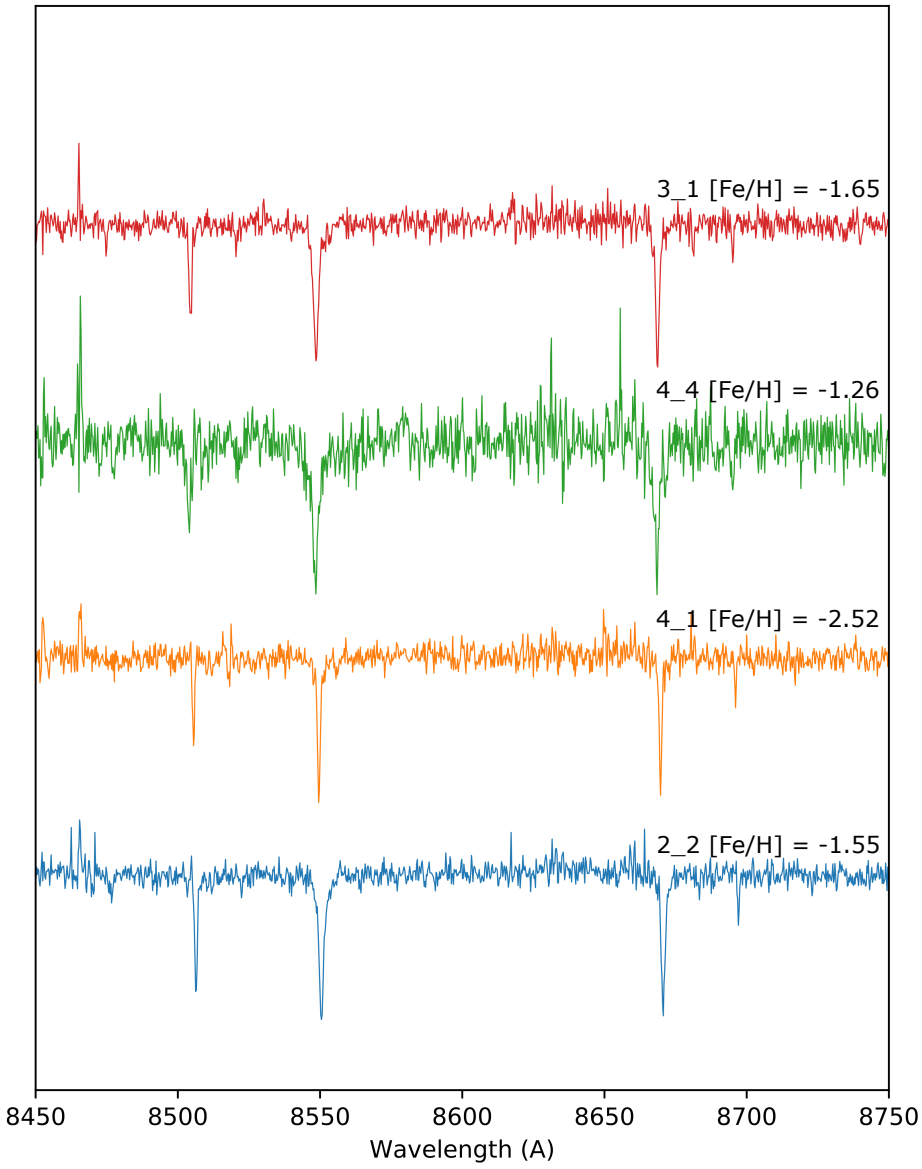

Figure B.19: Normalised spectra for metal-poor candidates in LMC field 20. From top to bottom: 3_1, 4_4, 4_1, and 2_2. Summary in Table B.7.

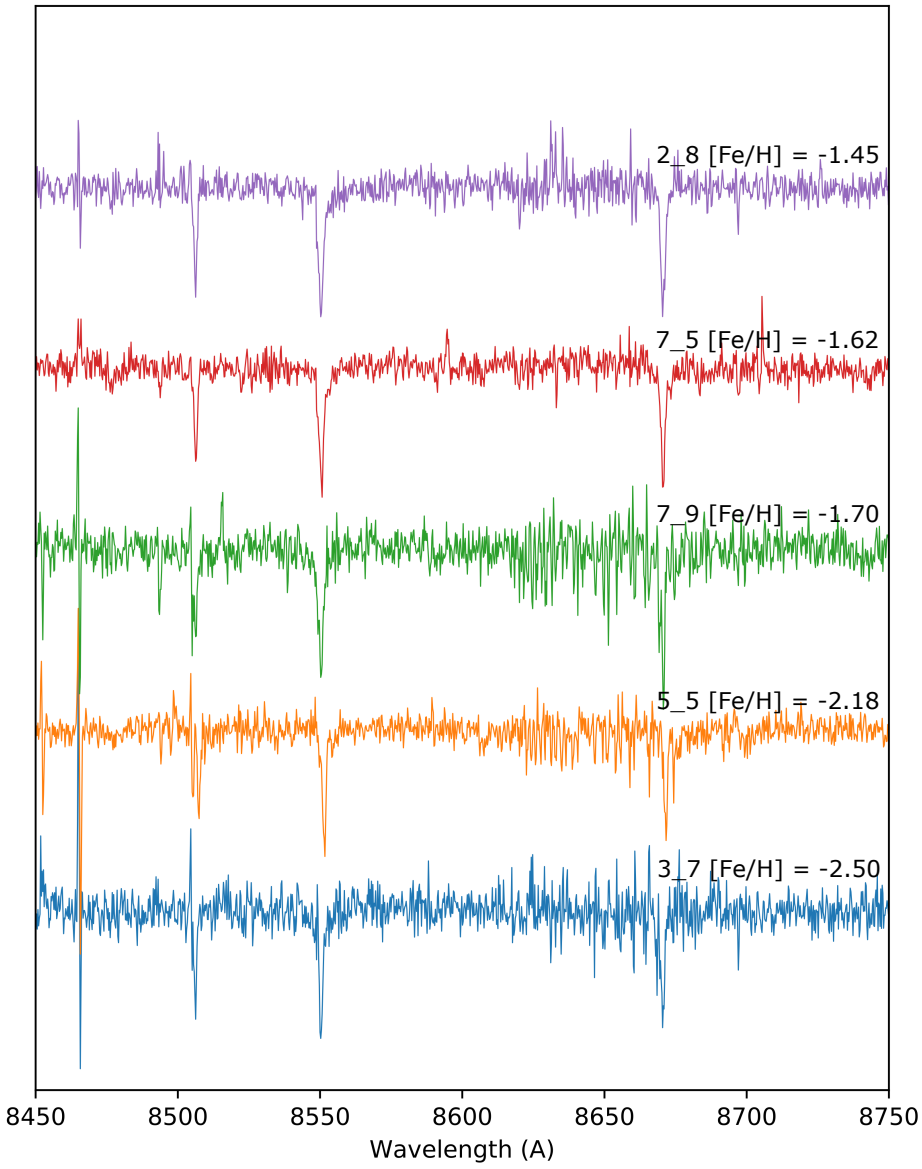

Figure B.20: Normalised spectra for metal-poor candidates in LMC field 20. From top to bottom: 2_8, 7_5, 7_9, 5_5, and 3_7. Summary in Table B.7.

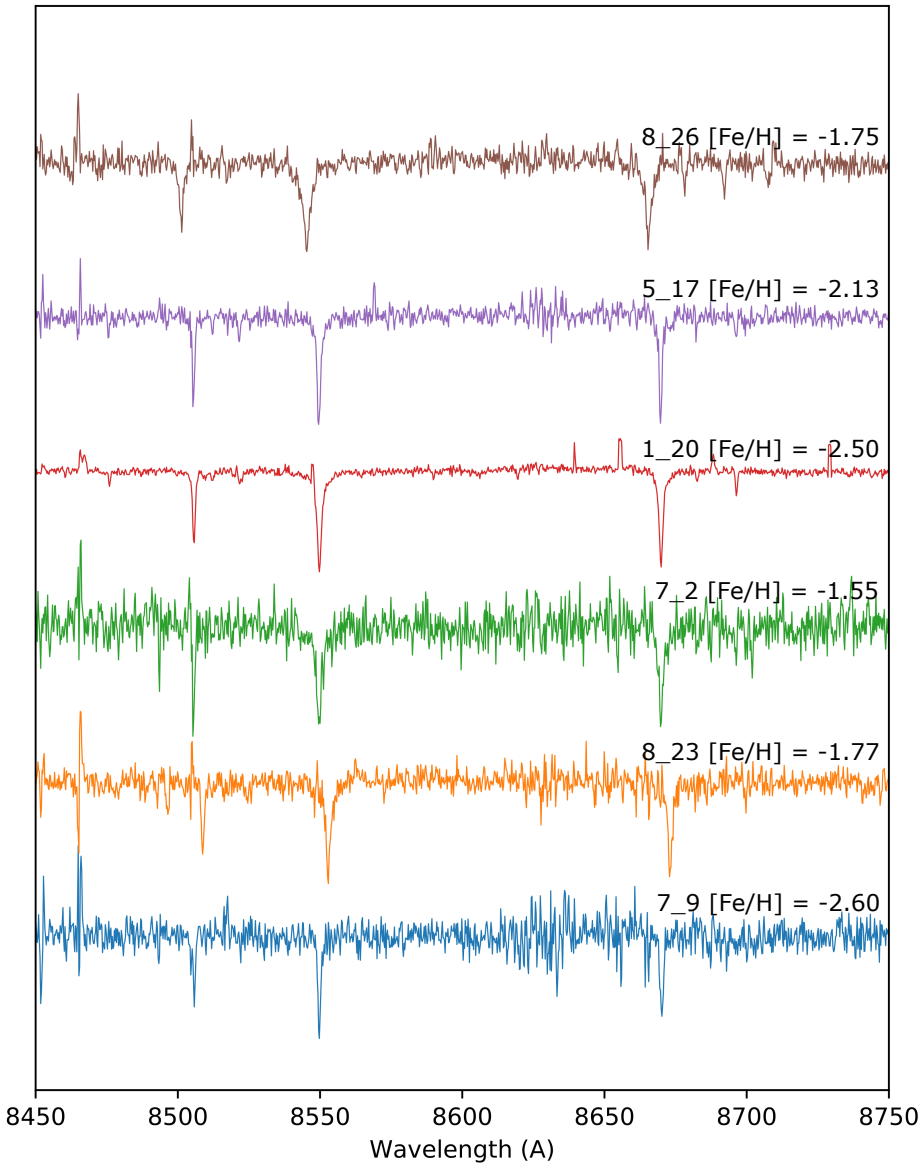

Figure B.21: Normalised spectra for metal-poor candidates in LMC field 15. From top to bottom: 8_{26}, 5_{17}, 1_{20}, 7_2, 8_{23}, and 7_9. Summary in Table B.8.

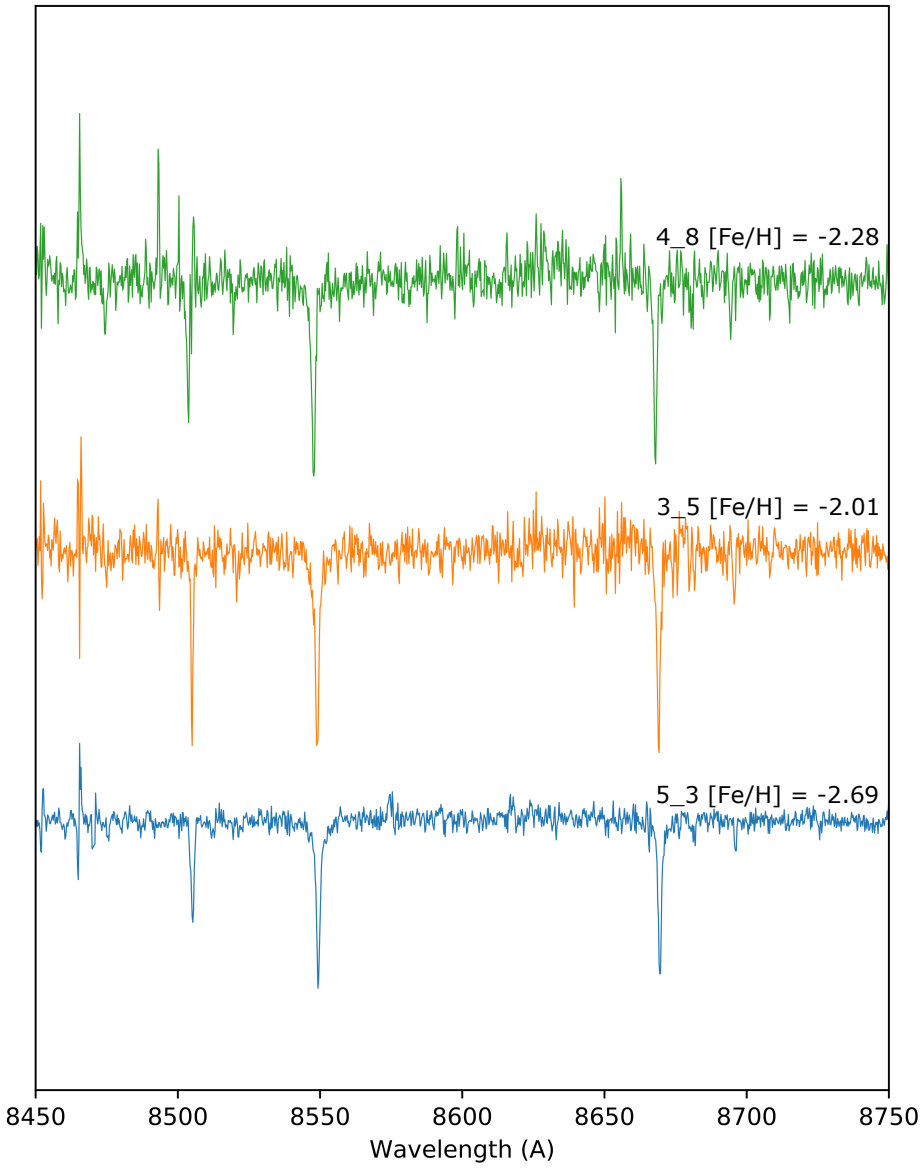

Figure B.22: Normalised spectra for metal-poor candidates in LMC field 13. From top to bottom: 4_8, 3_5, and 5_3. Summary in Table B.9.

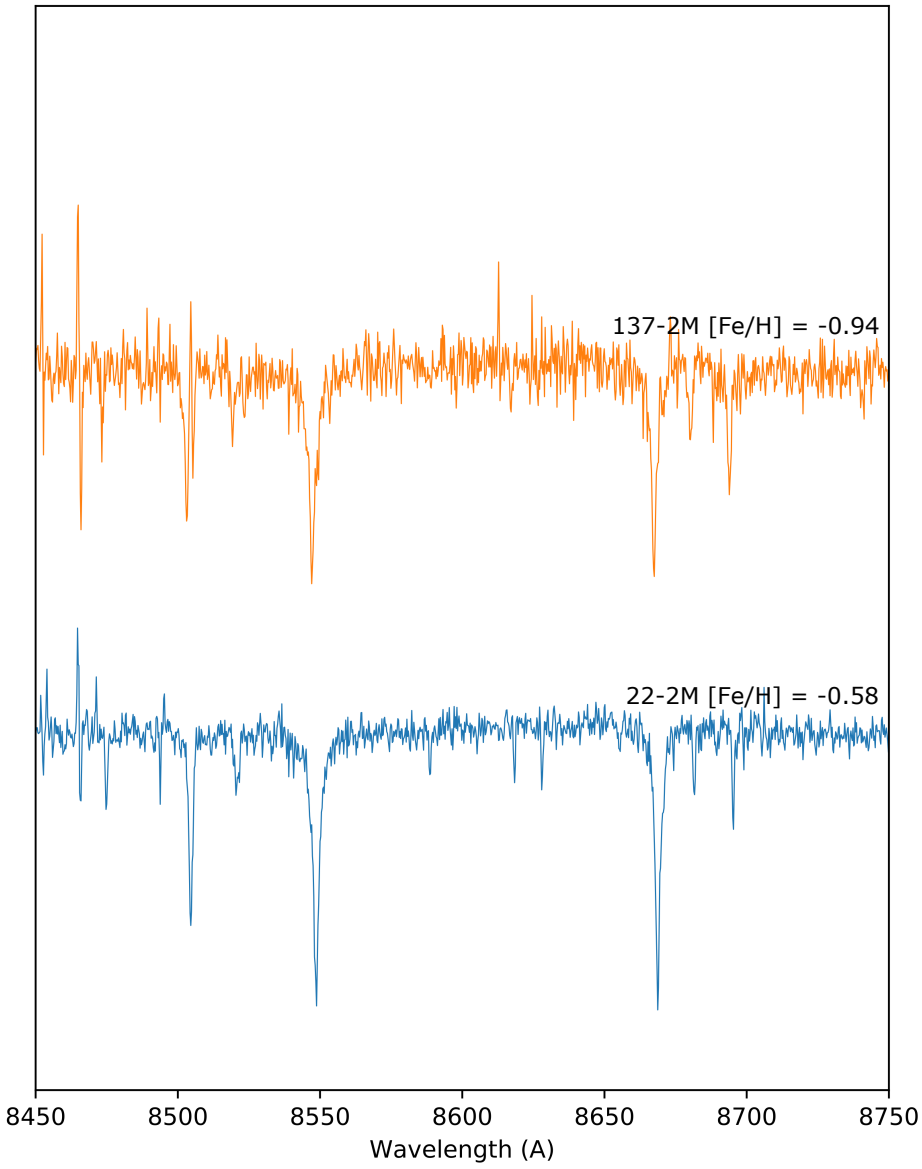

Figure B.23: Normalised spectra for metal-poor candidates in LMC field 11. From top to bottom: $137-2M$ and $22-2M$. Summary in Table B.10.

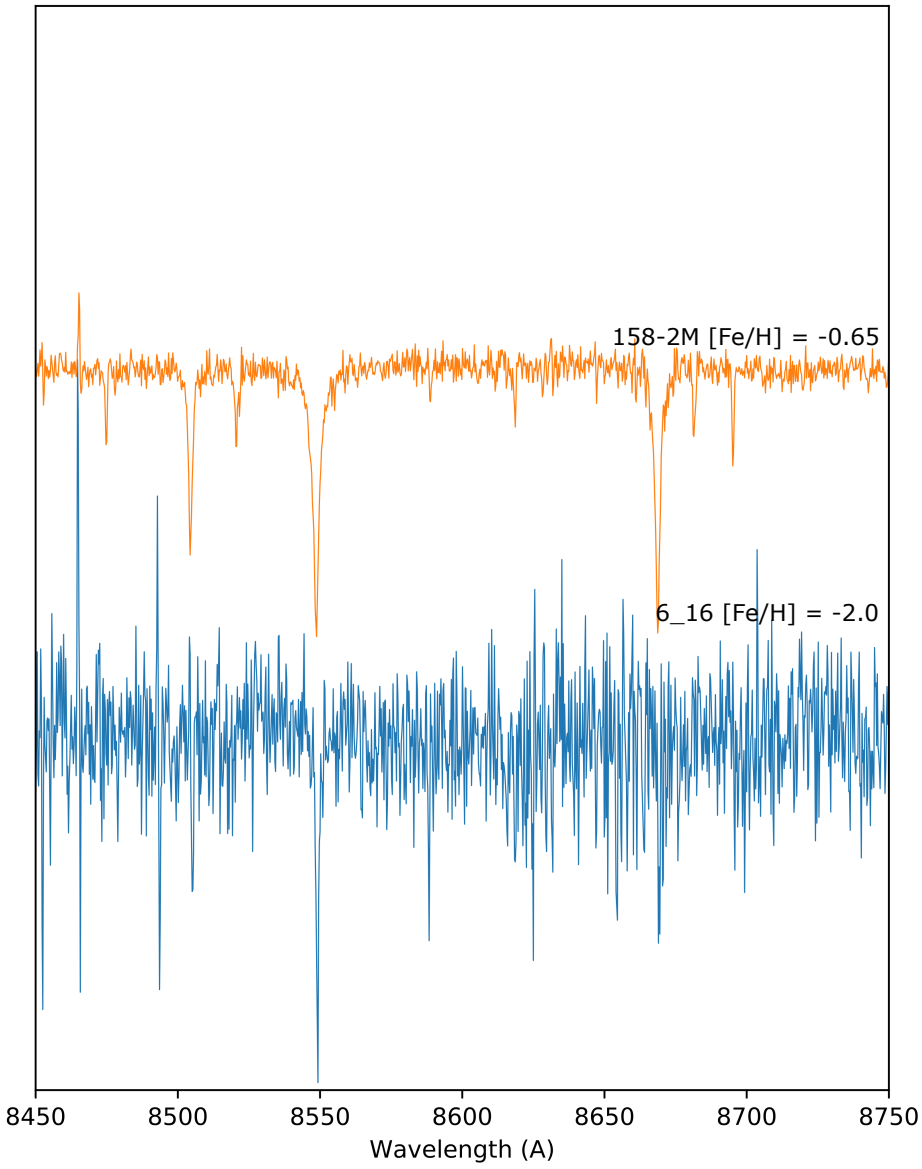

Figure B.24: Normalised spectra for metal-poor candidates in LMC field 8. From top to bottom: $158-2M$ and 6_{16}. Summary in Table B.11.

BIBLIOGRAPHY

Abel, T., Bryan, G. L., & Norman, M. L. 2002, Science, 295, 93

Anthony-Twarog, B. J., Sarajedini, A., Twarog, B. A., & Beers, T. C. 2000, AJ, 119, 2882

Anthony-Twarog, B. J. & Twarog, B. A. 1998, AJ, 116, 1922

Aoki, W., Suda, T., Boyd, R. N., Kajino, T., & Famiano, M. A. 2013, ApJL, 766, L13

Barklem, P. S., Christlieb, N., Beers, T. C., et al. 2005, A&A, 439, 129

Beers, T. C. & Christlieb, N. 2005, ARA&A, 43, 531

Beers, T. C., Preston, G. W., & Shectman, S. A. 1985, AJ, 90, 2089

Beers, T. C., Preston, G. W., & Shectman, S. A. 1992, AJ, 103, 1987

Bekki, K. & Chiba, M. 2005, MNRAS, 356, 680

Bessell, M., Bloxham, G., Schmidt, B., et al. 2011, PASP, 123, 789

Bond, H. E. 1970, ApJS, 22, 117

Bond, H. E. 1980, ApJS, 44, 517

Bromm, V. 2013, Reports on Progress in Physics, 76, 112901

Bromm, V., Coppi, P. S., & Larson, R. B. 2002, ApJ, 564, 23

Canterna, R. 1976, AJ, 81, 228

Carrera, R., Gallart, C., Aparicio, A., & Hardy, E. 2011, AJ, 142, 61

Cayrel, R., Depagne, E., Spite, M., et al. 2004, A&A, 416, 1117

Choi, J., Dotter, A., Conroy, C., et al. 2016, ApJ, 823, 102

Christlieb, N. 2006, in Astronomical Society of the Pacific Conference Series, Vol. 353, Stellar Evolution at Low Metallicity: Mass Loss, Explosions, Cosmology, ed. H. J. G. L. M. Lamers, N. Langer, T. Nugis, & K. Annuk, 271

Christlieb, N., Beers, T. C., Barklem, P. S., et al. 2004a, A&A, 428, 1027

Christlieb, N., Bessell, M. S., Beers, T. C., et al. 2002, Nature, 419, 904

Christlieb, N., Gustafsson, B., Korn, A. J., et al. 2004b, ApJ, 603, 708

Cignoni, M., Cole, A. A., Tosi, M., et al. 2012, ApJ, 754, 130

Clementini, G., Gratton, R., Bragaglia, A., et al. 2003, AJ, 125, 1309

Cohen, J. G., Christlieb, N., Thompson, I., et al. 2013, ApJ, 778, 56

Cole, A. A., Tolstoy, E., Gallagher, III, J. S., & Smecker-Hane, T. A. 2005, AJ, 129, 1465

Da Costa, G. S. 1991, in IAU Symposium, Vol. 148, The Magellanic Clouds, ed. R. Haynes & D. Milne, 183

Dalessandro, E., Schiavon, R. P., Rood, R. T., et al. 2012, AJ, 144

Dotter, A. 2016, ApJS, 222, 8

François, P., Depagne, E., Hill, V., et al. 2003, A&A, 403, 1105

Frebel, A., Aoki, W., Christlieb, N., et al. 2005, in IAU Symposium, Vol. 228, From Lithium to Uranium: Elemental Tracers of Early Cosmic Evolution, ed. V. Hill, P. Francois, & F. Primas, 207–212

Frebel, A., Simon, J. D., Kirby, E., Geha, M., & Willman, B. 2010, in IAU Symposium, Vol. 265, IAU Symposium, ed. K. Cunha, M. Spite, & B. Barbuy, 237–240

Geha, M. C., Holtzman, J. A., Mould, J. R., et al. 1998, AJ, 115, 1045

Geisler, D. 1996, AJ, 111, 480

Geisler, D., Claria, J. J., & Minniti, D. 1991, AJ, 102, 1836

Ginestet, N., Carquillat, J. M., Jaschek, M., & Jaschek, C. 1994, A&AS, 108, 359

Gontcharov, G. A. 2006, Astronomy Letters, 32, 759

Hansen, C. J., Bergemann, M., Cescutti, G., et al. 2013, A&A, 551

Harris, J. & Zaritsky, D. 2009, AJ, 138, 1243

Haschke, R., Grebel, E. K., & Duffau, S. 2011, AJ, 141, 158

Haschke, R., Grebel, E. K., Duffau, S., & Jin, S. 2012, AJ, 143, 48

Hollek, J. K., Frebel, A., Roederer, I. U., et al. 2011, ApJ, 742

Iben, Jr., I. 1983, Mem. S. A. It., 54, 321

Jorgensen, U. G., Carlsson, M., & Johnson, H. R. 1992, A&A, 254, 258

Kallivayalil, N., van der Marel, R. P., Besla, G., Anderson, J., & Alcock, C. 2013, ApJ, 764, 161

Keller, S. C., Bessell, M. S., Frebel, A., et al. 2014, Nature, 506, 463

Keller, S. C., Skymapper Team, & Aegis Team. 2012, in Astronomical Society of the Pacific Conference Series, Vol. 458, Galactic Archaeology: Near-Field Cosmology and the Formation of the Milky Way, ed. W. Aoki, M. Ishigaki, T. Suda, T. Tsujimoto, & N. Arimoto, 409

Kurucz, R. L. 1970, SAO Special Report, 309

Laporte, C. F. P., Gómez, F. A., Besla, G., Johnston, K. V., & Garavito-Camargo, N. 2018, MNRAS, 473, 1218

Mackey, A. D. & Gilmore, G. F. 2004, MNRAS, 352, 153

Majewski, S. R., Ostheimer, J. C., Kunkel, W. E., & Patterson, R. J. 2000, AJ, 120, 2550

McWilliam, A., Preston, G. W., Sneden, C., & Searle, L. 1995, AJ, 109, 2757

Meyer, B. S. 1994, ARA&A, 32, 153

Netopil, M., Paunzen, E., Heiter, U., & Soubiran, C. 2016, A&A, 585

Nidever, D. L., Majewski, S. R., Muñoz, R. R., et al. 2011, ApJL, 733, L10

Nikolaev, S. & Weinberg, M. D. 2000, ApJ, 542, 804

Nordlander, T., Amarsi, A. M., Lind, K., et al. 2017, A&A, 597, A6

Norris, J. E. 2004, Origin and Evolution of the Elements, 138

Norris, J. E., Christlieb, N., Korn, A. J., et al. 2007, ApJ, 670, 774

O'Donnell, J. E. 1994, ApJ, 422, 158

Pagel, B. E. J. 1997, Nucleosynthesis and Chemical Evolution of Galaxies (Cambridge University Press)

Palacios, A., Gebran, M., Josselin, E., et al. 2010, A&A, 516, A13

Paxton, B., Bildsten, L., Dotter, A., et al. 2011, ApJS, 192, 3

Paxton, B., Cantiello, M., Arras, P., et al. 2013, ApJS, 208, 4

Paxton, B., Marchant, P., Schwab, J., et al. 2015, ApJS, 220, 15

Piatti, A. E., Cole, A. A., & Emptage, B. 2018a, MNRAS, 473, 105

Piatti, A. E. & Geisler, D. 2013, AJ, 145, 17

Piatti, A. E., Geisler, D., & Mateluna, R. 2012, AJ, 144, 100

Piatti, A. E., Hwang, N., Cole, A. A., Angelo, M. S., & Emptage, B. 2018b, MNRAS, 481, 49

Pietrzyński, G., Gieren, W., Graczyk, D., et al. 2013, in IAU Symposium, Vol. 289, IAU Symposium, ed. R. de Grijs, 169–172

Placco, V. M., Frebel, A., Beers, T. C., & Stancliffe, R. J. 2014, ApJ, 797, 21

Robotham, A. S. G., Baldry, I. K., Bland-Hawthorn, J., et al. 2012, MNRAS, 424, 1448

Rollinde, E., Vangioni, E., Maurin, D., et al. 2009, MNRAS, 398, 1782

Rossi, S., Beers, T. C., Sneden, C., et al. 2005, AJ, 130, 2804

Rubele, S., Kerber, L., Girardi, L., et al. 2012, A&A, 537, A106

Schlaufman, K. C. & Casey, A. R. 2014, ApJ, 797, 13

Schlegel, D. J., Finkbeiner, D. P., & Davis, M. 1998, ApJ, 500, 525

Schmidt, B. P., Keller, S. C., Francis, P. J., & Bessell, M. S. 2005, in Bulletin of the American Astronomical Society, Vol. 37, American Astronomical Society Meeting Abstracts #206, 457

Shigeyama, T., Tsujimoto, T., & Nakamura, T. 2000, in Liege International Astrophysical Colloquia, Vol. 35, Liege International Astrophysical Colloquia, ed. A. Noels, P. Magain, D. Caro, E. Jehin, G. Parmentier, & A. A. Thoul, 43

Sneden, C., Cowan, J. J., Beers, T. C., et al. 2001, in Astronomical Society of the Pacific Conference Series, Vol. 245, Astrophysical Ages and Time Scales, ed. T. von Hippel, C. Simpson, & N. Manset, 235

Spite, F., Spite, M., Barbuy, B., et al. 2018, A&A, 611, A30

Starkenburg, E., Hill, V., Tolstoy, E., et al. 2010, A&A, 513, A34

Starkenburg, E., Martin, N., Youakim, K., et al. 2017, MNRAS, 471, 2587

Stetson, P. B. 1987, PASP, 99, 191

Stetson, P. B. 1994, PASP, 106, 250

Tafelmeyer, M., Jablonka, P., Hill, V., et al. 2010, A&A, 524, A58

Tumlinson, J. 2007a, ApJ, 665, 1361

Tumlinson, J. 2007b, ApJL, 664, L63

Tumlinson, J. 2010, ApJ, 708, 1398

van der Marel, R. P., Alves, D. R., Hardy, E., & Suntzeff, N. B. 2002, AJ, 124, 2639

Van der Swaelmen, M., Hill, V., & Primas, F. 2012a, in Astronomical Society of the Pacific Conference Series, Vol. 458, Galactic Archaeology: Near-Field Cosmology and the Formation of the Milky Way, ed. W. Aoki, M. Ishigaki, T. Suda, T. Tsujimoto, & N. Arimoto, 347

Van der Swaelmen, M., Hill, V., & Primas, F. 2012b, in SF2A-2012: Proceedings of the Annual meeting of the French Society of Astronomy and Astrophysics, ed. S. Boissier, P. de Laverny, N. Nardetto, R. Samadi, D. Valls-Gabaud, & H. Wozniak, 395–398

Van der Swaelmen, M., Hill, V., Primas, F., & Cole, A. A. 2013, ArXiv e-prints

Weisz, D. R., Dolphin, A. E., Skillman, E. D., et al. 2013, MNRAS, 431, 364

Wenger, M., Ochsenbein, F., Egret, D., et al. 2000, A&AS, 143, 9

Wiescher, M., Käppeler, F., & Langanke, K. 2012, ARA&A, 50, 165

Yong, D., Norris, J. E., Bessell, M. S., et al. 2013a, ApJ, 762, 26

Yong, D., Norris, J. E., Bessell, M. S., et al. 2013b, ApJ, 762, 27

Youakim, K., Starkenburg, E., Aguado, D. S., et al. 2017, MNRAS, 472, 2963

Zaritsky, D., Harris, J., Thompson, I. B., & Grebel, E. K. 2004, AJ, 128, 1606